AD_____
(Leave blank)

Award Number:

W81XWH-07-1-0640

TITLE:

Acoustic Inverse Scattering for Breast Cancer
Microcalcification Detection

PRINCIPAL INVESTIGATOR:

Matthew A. Lewis, Ph.D.

CONTRACTING ORGANIZATION:

University of Texas Southwestern Medical Center at Dallas

Dallas, TX 75390

REPORT DATE:

September 2011

TYPE OF REPORT:

FINAL Addendum

PREPARED FOR: U.S. Army Medical Research and Materiel Command
Fort Detrick, Maryland 21702-5012

DISTRIBUTION STATEMENT:

Approved for public release; distribution unlimited

REPORT DOCUMENTATION PAGE

1. REPORT DATE *(DD-MM-YYYY)*	2. REPORT TYPE	3. DATES COVERED *(From - To)*
01 December 2011	FINAL ADDENDUM	17 Aug 2010to 16 Aug 2011

4. TITLE AND SUBTITLE	5a. CONTRACT NUMBER
Acoustic Inverse Scattering for Breast Cancer Microcalcification Detection	W81XWH-07-1-0640
	5b. GRANT NUMBER
	5c. PROGRAM ELEMENT NUMBER

6. AUTHOR(S)	5d. PROJECT NUMBER
Matthew A. Lewis, Ph.D.	**5e. TASK NUMBER**
Matthew.Lewis@UTSouthwestern.edu	**5f. WORK UNIT NUMBER**

7. PERFORMING ORGANIZATION NAME(S) AND ADDRESS(ES)	8. PERFORMING ORGANIZATION REPORT NUMBER
University of Texas Southwestern Medical Center Dallas, TX 75390-9105	

9. SPONSORING / MONITORING AGENCY NAME(S) AND ADDRESS(ES)	10. SPONSOR/MONITOR'S ACRONYM(S)
U.S. Army Medical Research And Materiel Command Fort Detrick, Maryland 21702-5012	
	11. SPONSOR/MONITOR'S REPORT NUMBER(S)

12. DISTRIBUTION / AVAILABILITY STATEMENT

Approved for public release; distribution unlimited

13. SUPPLEMENTARY NOTES

14. ABSTRACT

An advanced scalar inverse scattering theory developed by Colton, Kirsch, and others in the inverse scattering community can determine the shape of scatterers with size on the order of the wavelength. In addition to size and number, the morphology of breast microcalcifications is an important diagnostic indicator. Our hypothesis was that the linear sampling method could be translated to an acoustic imaging system to detect, localize, and characterize microcalcifications in breast phantoms using data from the far-field scattering measurements. Novel ultrasound image reconstruction methods based on spherical and elliptical Radon transform have been developed. We conclude that inverse scattering algorithms for detecting microcalfications in heterogeneous tissue may be clinically feasible, but for estimating the shape of these microcalcifications the proposed algorithms only appear to work in simple phantoms that do not represent the complexity of biological tissue. The implemented methods were not robust upon the simple introduction of materials that simulate the scattering associated with the effect of cellular structure on biomedical ultrasound. However, detection of microcalcifications is a fairly robust application for inverse scattering.

15. SUBJECT TERMS
Ultrasound, inverse scattering, optimum array processing, breast cancer screening, detection, estimation, linear sampling method

16. SECURITY CLASSIFICATION OF:			17. LIMITATION OF ABSTRACT	18. NUMBER OF PAGES	19a. NAME OF RESPONSIBLE PERSON USAMRMC
a. REPORT U	**b. ABSTRACT** U	**c. THIS PAGE** U	UU	197	**19b. TELEPHONE NUMBER** *(include area code)*

Table of Contents

1   Introduction

Microcalcification detection is the hallmark of mammography as a breast cancer screening modality. For technical reasons, ultrasonic detection of all mammographically-visible microcalcifications has been problematic. In clinical ultrasound, high frequencies must be used to resolve microcalcifications below 200 micrometers. Unfortunately, ultrasonics above 10 MHz suffer from appreciable attenuation in soft tissues, and depth of penetration is limited. Transmission diffraction tomography, while well-suited for the geometry of the breast, is inherently insensitive to scattering caused by small, hard inhomogeneities. A more general form of acoustic inverse scattering is therefore needed for microcalcification detection and localization by ultrasound. We reasoned that the advanced scalar inverse scattering theory developed by Colton, Kirsch, and others in the RADAR community could potentially determine the shape of biological scatterers with size on the order of the wavelength. In addition to size and number, the morphology of breast microcalcifications is an important diagnostic indicator. Our hypothesis was that the linear sampling method (LS), when augmented with a method for estimating the inhomogeneous Green's function for wave propagation in the breast, can translate to an acoustic imaging system to detect, localize, and characterize microcalcifications in breast phantoms using data from the scattering measurements in a tomographic geometry.

2   Body

The goal of this research endeavor was to develop a bistatic ultrasound imaging method that specifically targeted breast microcalcifications. By bistatic imaging, we mean that receiver and transmitter can be separated in space. Since there were several commercial breast acoustic tomography systems undergoing FDA trials, we believed that it was an appropriate time to apply state-of-the-art methods from optimum array processing and inverse scattering to this important biomedical imaging problem.

In Tasks 8 and 9 of Year 1, we upgraded our water tank testing station to facilitate quicker data acquisition from custom ultrasound arrays with improved signal-to-noise ratio. Using provided funds, wereplaced an obsolete, 40 MHz, 8 bit, 48 channel DAQ system with a compact, portable, 64 channel, 12-bit, 65 MHz, commercial DAQ system. This piece of major equipment is based on a National Instruments (Austin, Texas) Compact PCI chassis containing 8 PXI-5105 8 channel digitizer boards. Through the development of custom software in the LabVIEW programming environment, we can capture data simultaneously from 64 array elements. At the time of purchase, this DAQ system was a novel design that has attracted the attention of the manufacturer, and subsequently we were involved as beta testers on a new product line that is focused on ultrasound/NDT DAQ at a much lower cost.

The goal of this program was to evaluate Colton-Kirsch linear sampling (CK-LS) method in breast ultrasound tomography. The CK-LS method is based on the mathematical analysis

of a model of scattering called the far-field operator:

$$(Fg)(x) = \int_\Omega u^\infty(x, d)g(d)ds$$

Here, F is the far-field complex amplitude for a sensor in direction x. The scatterer g lies in the domain Ω, and a plane wave is used to insonify the object from direction d. An important result of analysis by David Colton is: *Assume that ∂D is analytic and let* $z \in D$. *Then for every $\epsilon > 0$ there exists a solution $g = g(\cdot, z) \in L^2(\Omega)$ of the inequality* $\|Fg - \Phi^\infty(\cdot, z)\|_{L^2(\Omega)} < \epsilon$ *such that*

$$\lim_{z \to \partial D} \|g(\cdot, z)\|_{L^2(\Omega)} = \infty$$

In layman's term, this means that the solution to this equation for the far-field data will *blow-up* if the test point z is on the boundary of a scatterer. This suggests our computational strategy for *imaging* the surface of object.

In our software development, Gaussian quadrature and linearization were used to reduce the problem to a matrix equation.

$$(Fg)(x) = \Phi^\infty(x, z)$$

Here, $\Phi^\infty(x, z)$ is the Green's function for a point scatterer at position z in the field-of-view. Even after linearization, this inverse problem is ill-posed, so some sort of regularization is required. In Task 1, we developed software routines in Matlab that allow either Tikhonov regularization or singular value decomposition truncation, which is well-recognized as a simple form of regularization. For most numerical experiments with noiseless data, the regularization may be turned off.

One technical aspect of this research study dealt with a model-data mismatch. In general, all biomedical ultrasound data is acquired in the time-domain; that is, each channel or element of a receiver array records a signal in time. On the other hand, the family of inverse scattering algorithms of interest here are all frequency-domain algorithm; that is, they assume a single frequency wave that is actived for all time. While frequency-domain data acquisition is familiar to researchers working on near infra-red diffuse optical tomography of the breast, it is often not feasible to use frequency-domain data acquisition in ultrasound tomography due to the numerous spurious reflections from the imaging geometry and, in particular, the boundaries of the imaging domain. So, in all physical experiments, the first step in the data processing chain is to transform the time-domain data to the frequency-domain by employing the fast Fourier transform (FFT). Since the typical ultrasound signal possesses 100% fractional bandwidth, one is then left with the choice of how much bandwidth in the frequency space to utilize in the inverse scattering algorithm. For perfect synthetic or low noise real data, it may be sufficient to use only the complex amplitudes at the center frequencies. For noisy data, it may be useful to include all data up to the full-width-at-half-max. However, a balance must be struck between maximizing the data fidelity and minimizing the computational cost of a larger problem. As with all ultrasound tomography,

the frequency-domain data must be phase unwrapped, and standard libraries available in Matlab are applied.

We proposed in Task 2 to develop computation algorithms to generate synthetic data. For numerical simulations, we developed a variety of software tools for data that could be imported into Matlab for algorithm assessment. For 2D scattering in the frequency domain, the Matlab PDE Toolbox provided adequate support for generating test data using finite element analysis (FEA). For 3D scattering in the frequency domain, we utilized COMSOL Multiphysics, a commercial FEA platform that supports the importation of arbitrary scattering geometries. In practice, most of the research in this study involved phantoms that utilized cylindrical symmetry where only 2D imaging is required, so 3D synthetic data generation was developed but not utilized. Since physical data was in the time domain, we also investigated finite-difference time-domain (FDTD) software for generating test data. In the end, we adopted an open source electromagnetics tool called MEEP[1]. As described in [2], the z-invariant 2D Maxwell equations for either transverse electric or magnetic waves can be converted to the 2D acoustic wave equation (set of 2 coupled PDEs for pressure p and particle velocity $\mathbf{v}$) by replacing H_y by p, and replacing E_x and E_z by the 2D velocity components v_z and $-v_x$. In this manner, most electromagnetics packages can be used to simulate 2D ultrasound time-domain data.

Task 4, the migration of these computation tools to more powerful computer clusters, was ultimately delayed by the introduction of multicore computers. We find that much of our code for 2D simulation and imaging reconstruction runs in a reasonable amount of time on the desktop computers, and much of our Matlab code is parallalizable on GPUs using the Parallel Computing Toolbox.

A significant portion of our collaborative/synergistic efforts have dealt with Tasks 5 and 6, the development of methods for estimating the soft tissue heterogeneities that must be accounted for as a background scatterer in the CK-LS method [3]. An emerging model for time domain scattering in the bistatic ultrasound imaging geometry is the elliptical Radon transform (ERT). Small transducers can be modelled as having no directional sensitivity, and in this case the surface of constant time between a transmitter and receiver will be as follows.

Consider an ellipse with foci at $\vec{x}_e$ and $\vec{x}_r$. The family of ellipses at these foci have semi-major axis a, semi-minor axis b, and a foci separation of $2c = |\vec{x}_e - \vec{x}_r|$. The vector form of the ellipse can be written:
$$|\vec{x} - \vec{x}_e| + |\vec{x} - \vec{x}_r| = 2a$$

Next, we make use of an identity linking the a and c with the *eccentricity* e of the ellipse.

$$a = \frac{c}{e}$$

$$|\vec{x} - \vec{x}_e| + |\vec{x} - \vec{x}_r| = \frac{1}{e}|\vec{x}_e - \vec{x}_r|$$

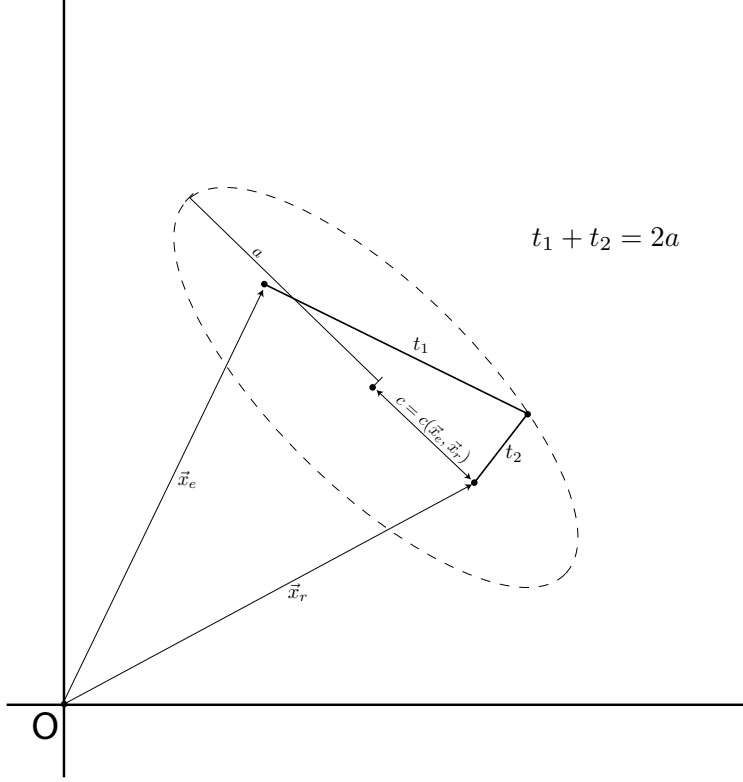e is defined in the domain $0 \leq e < 1$.

Figure 1: Geometry for elliptical Radon transform - a model for bistatic ultrasound array imaging in the breast

One possible definition for the elliptical Radon transform would therefore be:

$$R^{\bigcirc}_{\vec{x}_e,\vec{x}_r}(e) = \int_{|\vec{x}-\vec{x}_e|+|\vec{x}-\vec{x}_r|=\frac{1}{e}|\vec{x}_e-\vec{x}_r|} f(\vec{x})ds$$

There are 5 parameters in this expression. If we additionally require that the semi-major axis be orthogonal to a line from the origin to the center of the ellipse, then the number of parameters can be reduced to 4. Based on the principle of dimensionality, the system is still over-determined. Thus, a shot record for a circular aperture could be modelled as these integrals over ellipses, and some sort of inversion/image reconstruction should be possible in at least the least squares sense.

Recently, there appeared in the literature a backprojection-type algorithm for bistatic imaging according to the the ERT model [4]. Initially, we thought this algorithm might accelerate our development of the Green's function estimator in Task 6. However, one of the co-investigators (G. Ambartsoumian) is an expert in the area of image reconstruction for photoacoustic tomography (PAT), another imaging method that has shown much promise for breast cancer imaging. PAT uses a spherical Radon transform, and it was only in 2007 that a filtered backprojection algorithm appeared in the literature for the 2D problem [5].

In operator form, the proposed filtered backprojection algorithm for the elliptical model

was

$$f = B \circ F^{-1} \circ Abs \circ F \circ R_E \circ f$$

where F is a Fourier transform pair and Abs is the familiar ramp filter from classical tomography. In the case that the transmitter and received are brought together, then this inversion formula should reproduce the exact reconstruction algorithm found in [5]. Unfortunately, this is not the case. The filter found in [5] is logarithmic in the radius, and so we deemed the results in [4] to be incorrect. Please refer to Appendix A for a report summarizing this analysis.

We dedicated a focused effort on developing a proper method for estimating the soft tissue background in this ERT model. One of use (M. Lewis) has developed Matlab codes for forward projection and for estimating a discrete transfer matrix A so that iterative reconstruction methods such as Karmacz can be applied. In addition, a graduate student supported by this award studied the empirical behavior of the spherical filtered backprojection algorithm applied naively in the case of ERT, and this work was published in a Masters thesis[6].

Phantoms for algorithm testing and characterization were based on existing soft tissue phantoms for low-contrast diffraction tomography. 10 grams of agarose is dissolved in 75 ml heat water and poured into a mold to congeal. Acrylic inserts can be used to create voids that are filled in a second pass with a different density agarose. Modification of this phantom includes the addition of hexagonal Allen wrenches and square and round steel rod to simulate extended scatterers of known shape. Six time-domain multi-static response matrix data sets were acquired. These data supplement the scattering data from wires (so-called point scatterers), and include metal scatterers with both circular and hexagonal. The strong scatterers were embedded in a 7 cm diameter gelatin cylinder with known acoustic properties. Two variations of phantom were utilized: one with pure gelatin which produces a piece-wise homogeneous background, and then (in a parallel development to support Task 7) versions where the gelatin includes Metamucil or other fiber based dietary supplements which produce speckle that would be associated with the clutter in a random media and models the speckle observed in real soft tissue. This method was adopted from the literature[7], and we confirmed the B-mode appearance of this phantom using a VisualSonics Vevo700 small animal ultrasound system. Fluctuations in the data due to these hetergeneities can be similar in appearance to the signals due to the strong scatterer, and the goal of this study was to evaluate the performance of linear sampling in this situation.

For Task 13, a peer-reviewed conference proceeding publication[8] was published in early 2009 (see Appendix B). This work was in support of Tasks 6 and 12, and was made possible by the support of a Biomedical Engineering graduate student through this research project. In addition, a collaborator supported under the sub-award published a peer-reviewed book chapter on acoustic tomography in breast imaging. His support under this research project was critical to the completion of this, and it is noted in the acknowledgements of the publication[9].

For both synthetic and real data from phantoms, the amplitudes and phases from a tomographic geometry can be stored in a complex multistatic response matrix, as shown
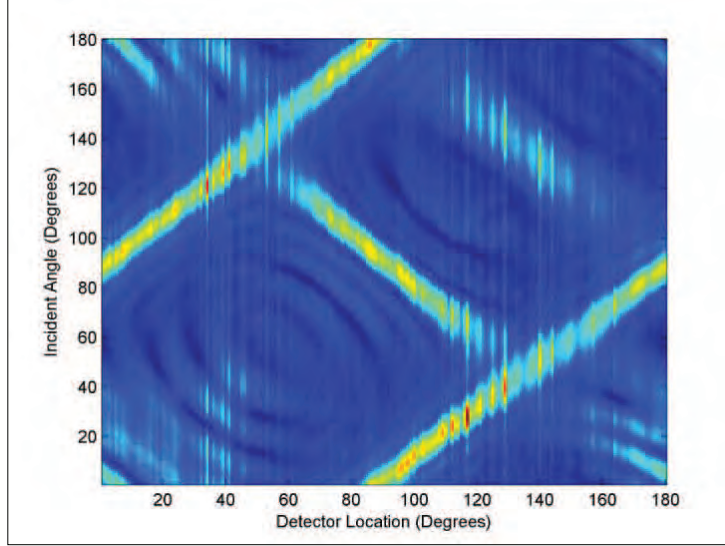
Figure 2: Magnitude of multistatic response matrix K for frequency-domain data

in Figure 2. For real data after transformation from time-domain to frequency-domain, this data will consist of a stack of K for varying spatial frequency k. The linear sampling algorithm family uses this data set to test points in space for affiliation with a scattering surface. When the complex data is tested in a raster mode, the points in image associated with the scattered will be larger than the background. As shown in Figure 3, this prototypical synthetic data set corresponds to a scattering inclusion that in this case is the complex shape of the state of Idaho.

In Figure 4, we present an example of an reconstruction of the shape of an extended scatterer, in this case a steel Allen wrench embedded in a gelatin phantom of known background properties. While the reconstruction is true to the shape of the object, one can observe that the background outside the scatterer is not as well-behaved as in the case with perfect synthetic data. Since the original time-domain data can have arbitrarily high signal-to-noise thanks to signal averaging, we hypothesize that these artifacts may be due to subtle numerical inaccuracies that arise during the Fourier transform and phase unwrapping steps. Next we consider equivalent phantoms where the background media contained fiber (Metamucil or other supplements). In all cases, the introduction of a random component to the background media spoiled the linear sampling algorithm's ability to estimate the shape of the scatterer. The clutter in the background media effectively increases the complexity of the problem, as demonstrated in Figure 5. If one examines the correlation matrix K^*K for the center spatial frequency, one observes that the data is complicated by the clutter, compared to synthetic data where the magnitude of the correlation matrix is smooth. When processed with the linear sampling algorithm (including regulatization) this *cluttered* (not noisy) data produces an image with no identifiable peaks that correspond to the shape of the object. While this is disappointing, the data is robust however for one particular algorithm in the linear sampling family. Using the MUltiple SIgnal Classification (MUSIC) algorithm and a
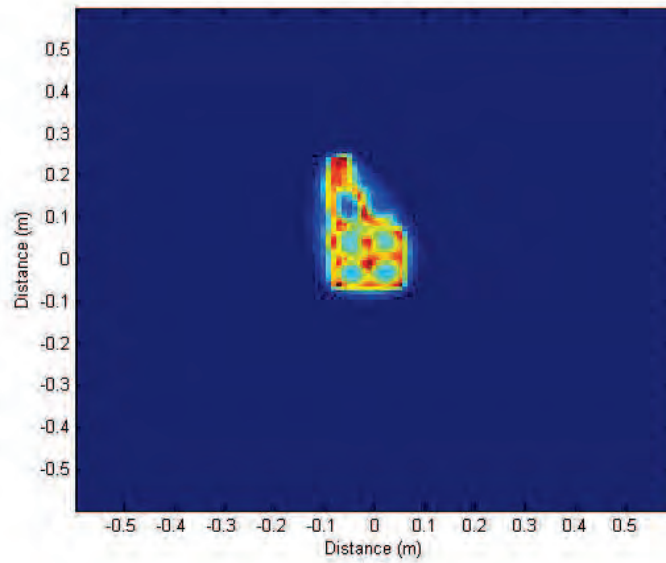
9

Figure 3: Reconstruction of scatterer with shape of state of Idaho using synthetic data

coarse raster scan, it is still feasible to detect the individual scatters even though one can not estimate their morphology, as demonstrated in the example in Figure 6.

Several difficulties were encountered during the history of this research project. First, recruitment of graduate students on the UT Southwestern side of the research was more difficult than anticipated, but this is a reflection of the current organizational structure rather than an issue with the provided support. In retrospect, a post-doctoral fellow may have been a wiser choice. In addition, reductions in institutional support made it difficult to replace mechanical and electrical engineering support, both who departed in 2008-2009. Lastly, in December 2010, all 8 National Instrument PXI-5105 data acquisition boards failed in short order due to defective capacitors. Fortunately, this issue was covered by a recall notice by the manufacturer, and this important equipment was restored to service in April 2011.

3   Supported Personnel

Matthew Lewis, Ph.D., Assistant Professor of Radiology, UT Southwestern
Edmond Richer, Ph.D., Assistant Professor of Radiology, UT Southwestern (now at Southern Methodist University)
Peter Antich, Ph.D., formerly Professor of Radiology, UT Southwestern
Ravi Vaidyanathan, M.Phil., Biomedical Engineering Graduate Program, UT Southwestern
Scott Jensen, UT Southwestern (now at Utah State University)
Tuncay Aktosun, Professor of Mathematics, UTA
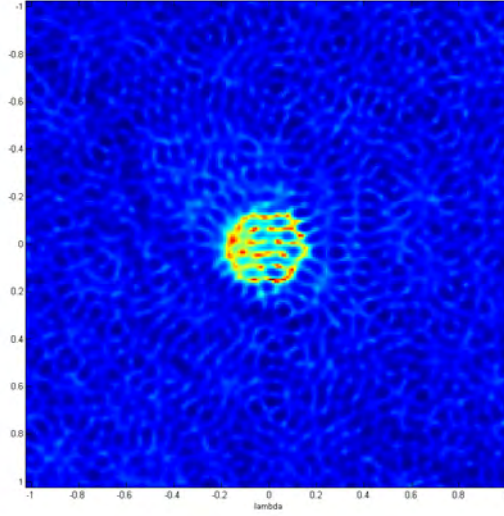Gaik Ambartsoumian, Assistant Professor of Mathematics, UTA

Figure 4: Image reconstruction for steel Allen wrench with hexagonal cross section

Rim Gouia, Ph.D., Department of Mathematics, UTA (now at American University of Sharjah, UAE)

4   Key Research Accomplishments

- Identification of fundamental shortcoming in the breast ultrasound tomography literature as it relates to bistatic imaging

- Development of elliptical Radon transform model for bistatic estimation of background Green's function.

- Numerical implementation of 2D elliptical Radon transform model of breast ultrasound tomography.

- Evaluation of spherical Radon transform filtered backprojection algorithm in the context of elliptical Radon transform model.

- Development of 2D software tools for forward modelling of the low frequency scattering process and the ill-posed algorithm for reconstructing the shape of scatterers, including 2D finite element for frequency domain representation and 2D FDTD for time domain.

- Successful application of linear sampling method to acoustic inverse scattering for high impedence targets embedded in homogeneous phantoms, but not in phantoms containing materials that simulate ultrasound speckle.
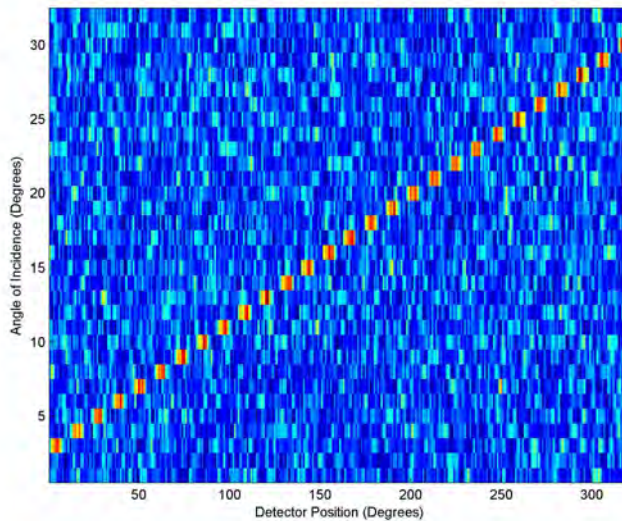
Figure 5: Correlation matrix derived from multistatic response matrix K for many scatterers

- Detailed analysis of circular Radon transform model for time domain ultrasound tomography for circular aperture.

5 Reportable Outcomes

- An abstract and poster were presented at the 2008 Era of Hope conference in Baltimore, Maryland: Acoustic Inverse Scattering for Task-Specific Breast Sonography - Development of Non-Ionizing Methods for Microcalcification Detection in High-Risk Populations[10].

- An abstract and poster were presented at the 2008 SIAM Imaging Science meeting in San Diego: Estimating Tumor Bounds in Bioluminescence Tomography[11]. Here, methods related to CK-LS were applied to a problem in optical imaging for breast cancer research.

- A conference proceedings publication on ultrasound tomography using the elliptical Radon transform model[8].

- A review article on tomographic imaging using spherical Radon transform models[9].

- Two collaborators (M Lewis and G Ambartsoumian) participated in the 2008 NSF/CBMS Rice Workshop on Imaging in Random Media, where image reconstructions methods of the types of interest in this research study were the focus.

- A biomedical engineering graduate student supported by this study completed a Masters of Science thesis on advanced image formation using ultrasound arrays[6].
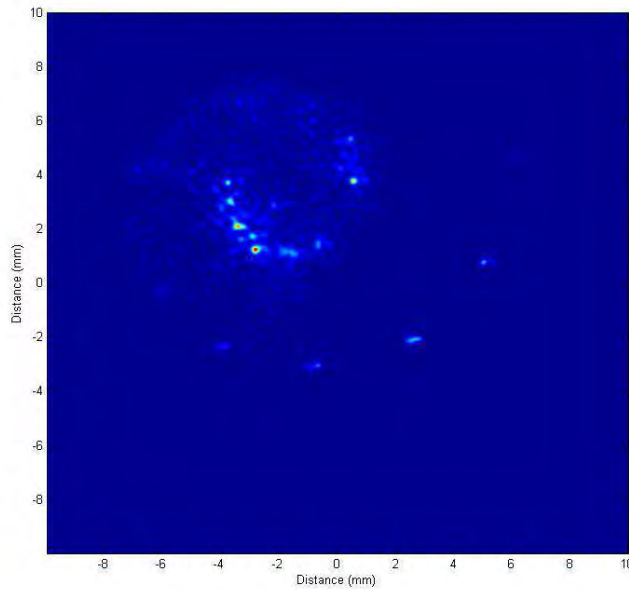
Figure 6: Reconstruction of many scatterers - shape estimation fails when there is background clutter, but detection more robust

- An applied mathematics graduate student supported by this study completed a Ph.D. dissertation on ultrasound image formation using circular arrays[12]. This individual subsequently accepted a position as an Assistant Professor of Mathematics at the American University of Sharjah, United Arab Emirates, where she hopes to continue her research in breast cancer imaging.

- A joint publication on circular array based ultrasound image formation[13].

- Co-investigator G Ambartsoumian is continuing related work through recently award National Science Foundation support (NSF DMS-1109417 *Elliptical Radon transforms in image reconstruction*).

- An additional manuscript (under preparation, to be submitted to the Journal of the Acoustical Society of America in 2012) that details successful imaging experiments in homogeneous, clutter-free backgrounds.

- An abstract and poster were presented at the 2011 Era of Hope conference in Orlanda, Florida: Novel Imaging Methods for Breast Sonography and Microcalcification Detection/Estimation[14].

6 Conclusion

In the context of real biomedical ultrasound imaging, we conclude that inverse scattering algorithms for detecting microcalcifications in heterogeneous tissue may be clinically feasible, but for the problem of estimating the shape of these microcalcifications (which is an important clinical indicator) the proposed algorithms, adopted from the RADAR community where waves propagate in much cleaner environments, only appear to work in simple phantoms that do not represent the complexity of biological tissue. The implemented methods were not robust upon the simple introduction of materials that simulate the scattering associated with the effect of cellular structure on biomedical ultrasound. It is unclear how this family of inverse scattering algorithms can be modified to deal with a random background medium.

At the onset of this research project, we envisioned that that the breast ultrasound tomography systems undergoing clinical trials would soon be available, at least for clinical research. That wish has unfortunately not been met, so applying the described methods (with only partial success) in 3D in more complicated phantoms or even living subjects is probably not warranted at this time. We note however 2 positive developments in this active area of research. Other research groups (some funded also by DOD CDMRP BCRP) have reported success using similar inverse scattering algorithms to detect microcalcifications using standard linear array transducers. In addition, new classes of image reconstruction algorithms for both detection and imaging in complex media like the breast are continuously being described, and there is potential that for improved performance in heavy clutter/speckle imaging[15] in the near future.

References

[1] Ardavan F. Oskooi, David Roundy, Mihai Ibanescu, Peter Bermel, J. D. Joannopoulos, and Steven G. Johnson. MEEP: A flexible free-software package for electromagnetic simulations by the FDTD method. *Computer Physics Communications*, 181:687–702, January 2010.

[2] Steven A Cummer and David Schurig. One path to acoustic cloaking. *New Journal of Physics*, 9(45), 2007.

[3] David Colton and Peter Monk. A linear sampling method for the detection of leukemia using microwaves. *SIAM J. Appl. Math.*, 58(3):926–941, 1998.

[4] Serge Mensah and Emile Franceschini. Near-field ultrasound tomography. *JASA*, 121(3):1423, 2007.

[5] David Finch, Markus Haltmeier, and Rakesh. Inversion of spherical means and the wave equation in even dimensions. *SIAM J Appl Math*, 68(2):392, 2007.

[6] Ravi Shankar Vaidyanathan. Advanced array imaging for breast and prostate sonography. Master's thesis, UT Southwestern Graduate School of Biomedical Sciences, 2009.

[7] Helen Morehouse, Harshada Pranav Thaker, and Chandowti Persaud. Addition of metamucil to gelatin for a realistic breast biopsy phantom. *J Ultrasound Med*, 26:1123–1126, 2007.

[8] Ravi Skankar Vaidyanathan, Matthew A. Lewis, Gaik Ambartsoumian, and Tuncay Aktosun. Reconstruction algorithms for interiour and exterior spherical radon transform-based ultrasound imaging. *Proceedings of SPIE*, 7265:72651l, 2009.

[9] Yuan Xu, Lihong V. Wang, Gaik Ambartsoumian, and Peter Kuchment. Limited view thermoacoustic tomography. *Photoacoustic Imaging and Spectroscopy*, pages 61–73, 2009.

[10] M A Lewis, T Aktosun, G Ambartsoumian, E Richer, and P P Antich. Acoustic Inverse Scattering for Task-Specific Breast Sonography - Development of Non-Ioninizing Methods for Microcalcification Detection in High-Risk Populations. *2008 Era of Hope Department of Defense Breast Cancer Research Program Meeting*, (P8-26), 25–28 June 2008. Baltimore, Maryland.

[11] M A Lewis. Estimating Tumor Bounds in Bioluminescence Tomography. *2008 SIAM Conference on Imaging Science and Annual Meeting*, (PP0-170), 7–11 July 2008.

[12] Rim Gouia. *Some Problems of Integral Geometry in Advanced Imaging*. PhD thesis, University of Texas at Arlington, 2011.

[13] G Ambartsoumian, R Gouia-Zarrad, and M A Lewis. Inversion of the circular radon transform on an annulus. *Inverse Problems*, 26(10), 2010.

[14] M A Lewis, S C Jensen, R S Vaidyanathan, T Aktosun, G Ambartsouiam, and R Gouia. Novel Imaging Methods for Breast Sonography and Microcalcification Detection/Estimation. *2011 Era of Hope Department of Defense Breast Cancer Research Program Meeting*, (P17-28), 3–5 August 2011. Orlando, Florida.

[15] L. Borcea, G. Papanicolaou, and C. Tsogka. Adaptive time-frequency detection and filtering for imaging in heavy clutter. *SIAM J. Imaging Sciences*, 4(3):827–849, 2011.

7   Appendices

Appendix A - Summary of mathematical modeling based on elliptical Radon transform
Appendix B - Reportable Outcome/Reference [6]
Appendix C - Reportable Outcome/Reference [9]
Appendix D - Reportable Outcome/Reference [12]
Appendix E - Reportable Outcome/Reference [13]

Appendix A - Research related to Task 6 performed under UT Arlington subaward

We consider a simple model of near-field ultrasound tomography, where a reflecting medium of interest is excited by spherical waves emitted from a transducer, and the backscattered echoes are registered by a receiver [11, 12]. Assuming an ideal propagative medium, where the speed of sound is constant, the signal registered at any given moment by the receiver is generated by reflections from all those points for which the sum of their distances to the emitter and the receiver is constant (depending on time and sound speed). In other words, those points are located on confocal ellipses with foci at the emitter and receiver locations, and the problem of image reconstruction in 2D boils down to the inversion of a transform integrating functions along such ellipses. In 3D one should consider a transform integrating along the family of surfaces of revolution (obtained by rotating the 2D ellipse around its main axis).

Definition 1. *The elliptical Radon transform (ERT) of $f(x)$, $x \in \mathbb{R}^2$ is defined as*

$$\tilde{R}f(p_e, p_r, r) = \int\limits_{|x-p_e|+|x-p_r|=r} f(x)dl(x),$$

where $dl(x)$ is the arc length of the ellipse $|x - p_e| + |x - p_r| = r$.

It is easy to see that the inversion of this transform is an overdetermined problem (recovering a function of 2 variables from a function of 5 variables). Hence, one should expect to be able to reconstruct f from restrictions of $\tilde{R}f$ to $2-$dimensional families of ellipses. From physical considerations we first restrict the locations of foci p_e and p_r (the acquisition geometry) to a curve S in $\mathbb{R}^2$ (denoting the transform by $\tilde{R}_S f(p_e, p_r, r) = \tilde{R}f(p_e, p_r, r)|_{p_e, p_r \in S}$). We consider the lines and circles for S in this project. Notice, that $\tilde{R}_S f(p_e, p_r, r)$

is a three-parameter family, while $f(x)$ is a function of two variables. There are several ways to reduce the dimension of the family of $\tilde{R}_S f(p_e, p_r, r)$. Motivated by tomographic models (e.g. [16, 3, 11, 12]) we will assume, that the distance between the emitter and the receiver stays constant. By matching the dimensions this way we further denote the ERT by $\tilde{R}_S f(p, r)$, where S is either a circle or a line, and p is the midpoint of the interval joining the foci of the ellipse.

Notice, that in the degenerate case when the emitter coincides with the receiver the ellipses become spheres and the ERT becomes a spherical (or circular) Radon transform (SRT). The latter has been extensively studied in the past for various applications of imaging and applied mathematics (e.g. [1, 2, 4, 8, 9, 10, 13, 15] and the references therein). In case of SRT various exact inversion formulae have been discovered for a limited number of acquisition geometries. These results can be divided into two categories: closed backprojection type inversion formulae, and expansions into series (usually involving some special functions). One of the goals of our project has been obtaining extensions of these results to the case of ERT, and the discovery of some new inversion algorithms. While the work in this direction is continuing, we can report certain progress here.

We developed an inversion algorithm using the algebraic reconstruction techniques based on the Kaczmarz method, which can work in any acquisition geometry. It also provides an effective mechanism for incorporation of certain side constrains to the reconstruction process, which is an extremely important tool for stabilizing the inversion in limited data problems. The developed algorithms have been numerically implemented in Matlab, and are currently being tested with both synthetic and experimental data. Two publications describing the developed methods and the obtained results are in preparation. The mathematical description of the inversion instabilities in limited data problems has been covered in [17].

We have also made certain progress in generalizing the inversion formulas for SRT using series expansion to the case of ERT. Most of the inversion formulas using series expansions for SRT are based on the fact, that this transform is either shift-invariant, or can become shift-invariant after a smooth change of variables. For example, the result of [13] is derived as follows. Let R_S be the 2D spherical Radon transform on the plane that integrates functions compactly supported inside the unit disk D over all circles $|x - p| = \rho$ with centers p located on the unit circle S. Since this transform commutes with rotations about the origin, the Fourier series expansion with

17

respect to the polar angle partially diagonalizes the operator, and thus the n-th Fourier coefficient $g_n(\rho)$ of $g = R_S f$ will depend on the n-th coefficient f_n of the original f only. Hence, the problem of reconstructing f from g, can be reformulated as a problem of reconstructing f_n from g_n. The latter requires solving and integral equation, which in [13] is done using the Hankel transform. In [14] the SRT is inverted in the case of a linear aperture by utilizing the shift invariance of the transform in the direction of the data acquisition line, and obtaining shift invariance in the orthogonal direction by a smooth change of variable. Then application of the 2-dimensional Fourier transform diagonalizes the operator, which enables the inversion. In case of a non-degenerate ERT in linear acquisition geometry, we have proved that there does not exist any smooth change of coordinates, which would make the transform shift-invariant in the second variable, hence one should not expect inversion procedures using Fourier techniques in this case. In the case of spherical acquisition geometry the elliptic transform $\tilde{R}$ also commutes with rotations about the origin, hence the inversion method using the Fourier series expansion may allow generalization to ERT. We have reduced the problem of recovering f from g to the problem of recovering f_n from g_n. The latter is a non-trivial integral equation, and we currently work on its solution.

References

[1] M. L. Agranovsky, and E. T. Quinto, "Injectivity sets for the Radon transform over circles and complete systems of radial functions," *J. Funct. Anal.*, **139** (1996), 383–413.

[2] L.-E. Andersson, "On the determination of a function from spherical averages," *SIAM J. Math. Anal.*, **19** (1988), no. 1, 214–232.

[3] J. Coker, and A. Tewfik, "Multistatic SAR image reconstruction based on an elliptical-geometry Radon transform," *2007 International Waveform Diversity and Design Conference*, 204–208, IEEE Conference Proceedings, 2007.

[4] A. Denisjuk, "Integral geometry on the family of semi-spheres," *Fract. Calc. Appl. Anal.*, **2** (1999), no. 1, 31–46.

[5] L. Ehrenpreis, *The Universality of the Radon Transform*, Oxford Univ. Press 2003.

[6] J. A. Fawcett, "Inversion of n-dimensional spherical averages", *SIAM J. Appl. Math.*, **45** (1985), no. 2, 336–341.

[7] D. Finch, M. Haltmeier, and Rakesh, "Inversion of spherical means and the wave equation in even dimension,", *SIAM J. Appl. Math*, **68** (2007), no.3, 392–412.

[8] D. Finch, Rakesh, and S. K. Patch, "Determining a function from its mean values over a family of spheres," *SIAM J. Math. Anal.*, **35** (2004), no. 5, 1213–1240.

[9] I. Gelfand, S. Gindikin, and M. Graev, *Selected Topics in Integral Geometry*, Transl. Math. Monogr. v. 220, Amer. Math. Soc., Providence RI, 2003.

[10] F. John, *Plane Waves and Spherical Means, Applied to Partial Differential Equations*, Interscience Publishers, 1955.

[11] S. Mensah, and E. Franceschini, "Near-field ultrasound tomography," *J. Acoust. Soc. Am*, **121** (3), March 2007, 1423–1433.

[12] S. Mensah, E. Franceschini, and M.-C. Pauzin, "Ultrasound mammography," *Nuclear Instruments and Methods in Physics Research*, Section A, **571** (2007), no. 3, 52–55.

[13] S. J. Norton, "Reconstruction of a two-dimensional reflecting medium over a circular domain: Exact Solution," *J. Acoust. Soc. Am.*, **67** (1980), no. 4, 1266–1273.

[14] S. J. Norton, "Reconstruction of a reflectivity field from line integrals over circular paths," *J. Acoust. Soc. Am.*, **67** (1980), no. 3, 853–863.

[15] S. J. Norton, and M. Linzer, "Ultrasonic reflectivity imaging in three dimensions: exact inverse scattering solutions for plane, cylindrical, and spherical apertures," *IEEE Trans. Biomed. Eng.*, **28** (1981), 202–220.

[16] D. Trad, T. Ulrych, and M. Sacchi, "Accurate interpolation with high-resolution time-variant Radon transforms," *Geophysics*, **67** (2002), no.2, 644–656.

[17] Y. Xu, L.-H. Wang, G. Ambartsoumian, and P. Kuchment, "Limited view thermoacoustic tomography," in *Photoacoustic imaging and spectroscopy, ed. L.-H. Wang*, CRC Press, 2009.

ADVANCED ARRAY IMAGING FOR BREAST AND

PROSTATE SONOGRAPHY

By

RAVI SHANKAR VAIDYANATHAN

MASTER OF SCIENCE IN BIOMEDICAL

ENGINEERING

University of Texas Southwestern Medical Center at

Dallas

Dallas, TX

2009

Submitted to the Faculty of the
Graduate Colleges of the
University of Texas Southwestern Medical Center at
Dallas and University of Texas at Arlington
in partial fulfillment of
the requirements for
the Degree of
MASTER OF SCIENCE
December, 2009

ADVANCED ARRAY IMAGING FOR BREAST AND

PROSTATE SONOGRAPHY

Thesis Approved:

Dr. Matthew A. Lewis, Ph.D

Dr. Vikram Kodibagkar, Ph.D

Dr. Roddy McColl, Ph.D

Dr. Nikolai Slavine, Ph.D

ACKNOWLEDGMENTS

I would like to express my primary thanks to Dr. Matthew Lewis, my mentor, for his sincere support, guidance and advice in both academic and personal areas. He was very supportive in helping me finish my course works. At several occasions has personally advised me on various things. It was a very good experience to work under him.

I would like to thank the program chair Dr. Peter Antich for accepting me in this program and give me a chance to get trained on various imaging modalities. He has advised me at many levels to help me complete this degree.

I would like to extend special thanks for Dr. Vikram Kodibagkar and Dr. Nikolai Slavine for advising me on various aspects of personality development. Their inputs are much appreciated.

I would like to thank Ms. Kay Emerson, the BME program assistant for helping me out with administrative issues and offering me valuable advices.

I would like to thank my parents and family.

Finally, I would like to thank my wife for her love and understanding.

TABLE OF CONTENTS

LIST OF TABLES

LIST OF FIGURES

CHAPTER I

INTRODUCTION

1.1 Ultrasound Imaging

In conventional medical ultrasound such as B-mode imaging, the amplitude of the back-scattered ultrasound pulse is used to image tissues along a fixed beam direction[1]. This imaging technique works best in static organs, and it is difficult to image moving organs like the heart. The M-mode imaging technique is better for cardiac applications. For better image resolution, ultrasound tomography systems were developed in which ultrasound data were acquired by transducers placed in a circle around the object[2]. This task of deriving the structure of the object from scattered radiation is known as the inverse scattering problem.

The inverse scattering problem is known by several names like reflectivity tomography[3] and diffraction tomography[5, 6, 7] etc. Scattering refers to the effects on wave propagation due to an inhomogeneous medium. Since the inhomogenieties are unknown, the goal is to determine their properties – the spatial variation in density, compressibility, geometrical distribution etc. With the scattered wave field, determining the scatterer is called the inverse problem. As for the geometry of the scattering theory, the scatterer is assumed to

be present in a homogeneous reference medium with known properties. Following the notations used in Lehman[8], the acoustic pressure, p, in this medium satisfies the Helmholtz equation

$$(\nabla^2 + k^2)\, p(\mathbf{r}) = 0 \tag{1}$$

where the pressure field is given by

$$p(\mathbf{r},t) = p^0 + p^1(\mathbf{r},t) \tag{2}$$

The ambient pressure, p^0 is constant. Since the scatterer is present in the reference homogeneous medium, the pressure field can be written as

$$p_0(\mathbf{r}) = p^{inc}(\mathbf{r}) + p^{sc}(\mathbf{r}) \tag{3}$$

where p^{inc} refers to the incident field and p^{sc} is the scattered field. In an ideal situation the incident pressure field is taken as a plane wave

$$p^{inc}(\mathbf{r}) = p^0\, e^{ikz} \tag{4}$$

where k is the complex wave number which is given by

$$k = (\omega/c)\,(1 - i\omega M_\kappa) \tag{5}$$

where M_κ is the compressional viscosity.

Now, we are in a position to introduce the integral representations of the scattered field. In the region exterior to the scatterer, the pressure field is given by

$$(\nabla^2 + k^2)\, p_0(\mathbf{r}) = 0 \tag{6}$$

Introducing the Green's function

$$G(\mathbf{r} - \mathbf{r}') = e^{ik|\mathbf{r}-\mathbf{r}'|}/|\mathbf{r}-\mathbf{r}'| \tag{7}$$

that will satisfy the inhomogeneous impulse equation

$$(\nabla^2 + k^2)\, G(\mathbf{r} - \mathbf{r}^{'}) = -4\pi\delta(\mathbf{r}\text{-}\mathbf{r'}) \qquad (8)$$

Using one of the most frequently used approximations, the Rayleigh-Born approximation we can modify equation (7). At large distance the Green's function can be approximated by

$$G(\mathbf{r} - \mathbf{r}^{'}) \sim e^{ikr}/r \ \ e^{-ikr.\mathbf{r'}} \qquad (9)$$

which holds true for $k_0 r^{'2}/r \ll 1$.

A Fourier diffraction theorem based reconstruction technique using the Born approximation is derived in Radial Reflection Diffraction Tomography (RRDT) [8]. Though my work is concerned with time-domain reconstruction techniques, I will discuss some existing frequency domain reconstruction techniques.

1.1.1   B-mode Imaging

B-mode (for Brightness mode) images are 2-D ultrasound images that contain pixels that correspond to ultrasound echoes. The value of the pixels corresponds to the amplitude of the echo. The image is obtained by sweeping narrow ultrasound through the object while detecting the echoes with a linear electronic array. In the B-mode image, the vertical position of the bright pixel is determined by the time-of-delay of the ultrasound wave and the horizontal position is determined by the location of the receiver. The path the echo follows is usually referred to as the beam line. The direction of the propagation along the beam line is called the axial direction and the direction perpendicular to this is called the

lateral direction. This technique also provides data at various levels enabling the creation of three-dimensional image.

The reconstruction technique may be compared to a crude backprojection of the obtained data without using any filter. In this way, B-mode imaging is considered very primitive form of ultrasound image reconstruction. Better techniques of reconstructing ultrasound data were later developed in the scheme of tomographic setup[2].

1.2 Interaction of Ultrasound Waves with the Biological Media

Ultrasound is the propagating disturbance of the properties (e.g., pressure and particle position) of the tissue through which it travels. Unlike electromagnetic radiation which can propagate in vacuum, ultrasound needs the material through which it travels. As a consequence this leads to interactions between the physical properties of the tissues and the extrinsic properties of the ultrasonic waves such as pressure. Acoustic properties of tissues as measured in many experiments were tabulated by Goss and Dunn[18, 19].
In medical imaging applications, the range of ultrasound frequencies used vary from 2-10 MHz (for imaging deep organs) to 40 MHz (for intrarterial imaging)[1]. In soft tissues

Material	Density (Kg/m^3)	Compressibility (10^{-12} m^2/Nt)	Velocity (m/s)	Acoustic Impedance (10^6 Kg/m^{2}s)
Fat	950	508	1440	1.37
Blood	1025	396	1570	1.61
Muscle	1070	353-393	1542-1626	1.65-1.74
Bone	1380-1810	25-100	27100-4100	3.75-7.4

Table 1.1 Acoustic parameters for some biological materials[9]

(which are predominantly water) like tendons and fat, the ultrasound propagation velocity is around 1500 m/s. Table 1.1 lists few of the acoustic parameters for some biological materials[9]. Though we notice the velocity of sound differs between materials, most of the time-domain reconstruction techniques assume the speed of sound to be constant, and the body is thus inhomogeneous in density. The speed of sound is related to the density and compressibility of the material in the following way:

$$c=1/(\rho\kappa)^{1/2} \qquad (10)$$

where ρ is the density and κ is the compressibility. Now we are in a position to define the term *acoustic impedance Z*,

$$Z=\rho c \qquad (11)$$

Variations in acoustic impedances cause specular reflection of the waves.

As mentioned earlier the spatial resolution of the ultrasound images depend on the frequency of the waves used (higher the frequency, better the resolution). But, higher frequencies also mean higher attenuation. So, there is always a trade-off depending on the organ of interest. In adult cardiology[1] 2.5-5 MHz is used to get enough penetration and for imaging of intravascular atherosclerosis, frequencies up to 40 MHz is used. The positioning of the transducers also plays an important role. For example, the nearest possible routes anatomically to place the transducers and image the prostate is transrectal and transurethral. This leads to various interesting geometries from a tomographic perspective for which no reconstruction algorithms exist.

1.3 Ultrasonic Tomography – frequency domain image reconstruction

So far the basics of ultrasonic imaging have been discussed. These ultrasound principles were used for a long time in conventional ultrasonic imaging developed for B-mode and M-mode imaging. One of the earliest works which used acoustic imaging in a tomographic setup, in the frequency domain, used algebraic reconstruction techniques (ART) [10, 11] to form images. Greenleaf used similar techniques to reconstruct the speed of sound using time-of-flight profiles[12].   Like most ART techniques the work was computationally intensive. Then there were techniques based on perturbation solutions of the wave equations[5]. These techniques reconstructed the speed of sound by approximating it by a small perturbation to velocity in the surrounding medium. Using

few first-order perturbation equations, images were reconstructed. There were old techniques that reconstructed spatial distribution of acoustical absorption with tissues from their two-dimensional projections[13], in a manner analogous to filtered backprojection.

1.4 Diffraction tomography Methods (Frequency domain imaging techniques)

There is another tomographic technique to reconstruct acoustic data called the diffraction technique. There are two important approximations that are used to approximate the wave equation, namely the Born[15] and the Rytov[16] approximations that transform homogeneous wave equation into nonhomogeneous equation using perturbation methods which can then be solved analytically which will include the effects of diffraction.

1.4.1   The Born approximation

Let us start with the Helmholtz equation and using the notations used by Lehman[8], we have

$$\nabla^2 \psi + K^2 \psi = 0 \tag{12}$$

If the total wave is the sum of incident and scattered wave, i.e.

$$\psi = \psi^{sc} + \psi^{inc} \tag{13}$$

then equation (12) can be written as

$$\nabla^2 \psi^{sc} + k_0{}^2 \psi^{sc} = O\psi^{inc} \qquad (14)$$

where

$$O = -k_0{}^2(B^2 - 1) \qquad (15)$$

and the object function,

$$B^2 = k(x)^2 / k_0{}^2$$

(16)

where $k(x)$ is the wavenumber of the medium which varies spatially and k_0 is the wavenumber of the background medium. We arrived at equation (14) with an important assumption inherent with the Born approximation,

$$\psi^{sc} << \psi^{inc} \qquad (17)$$

that is, it assumes that the amplitude of the scattered energy is much less than the incident energy.

1.4.1   The Rytov approximation

Let us start again with wave equation (12) and substitute

$$\psi(\mathbf{r}) = \exp(i\, k_0 \phi(\mathbf{r})) \qquad (18)$$

where we express ψ in a form that assumes the information to be in the *phase* part of an exponential form, where complex phase allows for spatial variation in both propagation velocity and attenuation. The substitution results in

$$i\, k_0{}^{-1} \nabla^2 \phi \ - \ |\nabla \phi|^2 + A^2 = 0 \qquad (19)$$

15

where

$$A = 1 + \eta \tag{20}$$

where η is the change in refractive index. Now, let $\phi = \phi_0 + \phi_1$ where ϕ_0 is the phase

component of the pressure distribution $\psi(\mathbf{r})$ for no perturbation and where ϕ_1 is the phase

perturbation due to perturbation in the refractive index. Substituting the perturbations into

equation (19) we get,

$$i\,k_0^{-1}\nabla^2\phi_0 + i\,k_0^{-1}\nabla^2\phi_1 - |\nabla\phi_0|^2 - 2(\nabla\phi_0 \cdot \nabla\phi_1) - |\nabla\phi_1|^2 + 1 + 2\eta + \eta^2 \tag{21}$$

Ignoring η^2 and $|\nabla\phi_1|^2$, we get,

$$\nabla^2(\phi_1\exp(ik_0\phi_0)) + k_0^2(\phi_1\exp(ik_0\phi_0)) = i2k_0\eta\exp(i\,k_0\phi_0) \tag{22}$$

Equations (22) are the Rytov's approximation and it has the same form as equation (14).

Equations (14) and (22) are both linear and their solution is a convolution of Green's

solutions with the source terms for all space. The result is obtained by Tribolet[17].

1.4.2 Monostatic forward scattering model

To develop a linear forward scattering model for monostatic setup we start with the

Helmholtz equation that governs the wave propagation and scattering,

$$[\nabla^2 + k^2(\mathbf{r})]\,\psi(\mathbf{r},\omega) = -p(\mathbf{r},\omega), \tag{23}$$

where $\mathbf{r}$ is given by the polar spatial coordinates $r(\cos\theta, \sin\theta)$ of a point in the

surrounding medium, ω, the temporal frequency, $k(\mathbf{r})$ is the wavenumber of the medium,

$\psi(\mathbf{r},\omega)$ is the total field, $p(\mathbf{r},\omega)$, the incident pulse temporal spectrum. To remove the

spatial inhomogeneity in equation (23), we add the background wavenumber, $k_0(\omega)=$

ω/v_0, to both sides of the equation and move the inhomogeneous term to the right hand

side to obtain,

$$[\nabla^2 + k_0{}^2] \psi(\mathbf{r},\omega) = -p(\mathbf{r},\omega) - [k^2(\mathbf{r}) - k_0{}^2(\omega)] \psi(\mathbf{r},\omega) \qquad (24)$$

Defining the object function as,

$$o(\mathbf{r}) = (k^2(\mathbf{r})/ k_0{}^2) - 1 \qquad (25)$$

equation (24) becomes,

$$[\nabla^2 + k_0{}^2] \psi(\mathbf{r},\omega) = = -p(\mathbf{r},\omega) - k_0{}^2(\omega)\, o(\mathbf{r})\, \psi(\mathbf{r},\omega) \qquad (26)$$

where the term $k_0{}^2(\omega)\, o(\mathbf{r})\, \psi(\mathbf{r},\omega)$ is known as the secondary source which creates the

scattered field. To convert equation (26) into an integration equation we have to use the

Green's theorem[43]. Equation (26) now becomes,

$$\psi(\mathbf{R},\omega) = \int d\mathbf{r}\, G(\mathbf{R},\mathbf{r'},\omega) P(\mathbf{r'},\omega) + k_0{}^2(\omega) \int d\mathbf{r'}\, G(\mathbf{R},\mathbf{r'},\omega) o(\mathbf{r'}) \psi(\mathbf{r'}), \qquad (27)$$

where the Green's function is given by,

$$G(\mathbf{R},\mathbf{r},\omega) = e^{ik0|\mathbf{R}\text{-}\mathbf{r}|}/4\pi|\mathbf{R}\text{-}\mathbf{r}| \qquad (28)$$

The first integral in equation (27) is the primary field, $\psi^{inc}(\mathbf{R},\omega)$. Subtracting it from the

total field yields the scattered field,

$$\psi^{scat}(\mathbf{R},\omega) = \psi(\mathbf{R},\omega) - \psi^{inc}(\mathbf{R},\omega) = k_0{}^2(\omega) \int d\mathbf{r}\, G(\mathbf{R},\mathbf{r},\omega) o(\mathbf{r}) \psi(\mathbf{r}) \qquad (29)$$

Evaluating the scattered field on the measurement surface, $\mathbf{r_0}$, we obtain,

$$\psi^{scat}(\mathbf{r_0},\omega) = k_0{}^2(\omega) \int d\mathbf{r}\, G(\mathbf{r_0},\mathbf{r},\omega) o(\mathbf{r}) \psi(\mathbf{r}) \qquad (30)$$

The above equation is nonlinear the scattering term is on both sides and is under an

integral on the right hand side. Therefore to reconstruct an estimate of $o(\mathbf{r})$, we need to

simplify the equation by linearizing it. We can do it by assuming that the medium is weakly scattering and that the first Born approximation holds. Therefore equation (30) becomes

$$\psi_{\text{born}}^{\text{scat}}(\mathbf{r_0},\omega)= k_0^2(\omega)\int d\mathbf{r}G(\mathbf{r_0},\mathbf{r},\omega)o(\mathbf{r})\psi^{\text{inc}}(\mathbf{r}) \tag{31}$$

We further assume the incident field is the results of a point source at $\mathbf{r_0}$, so that $p(\mathbf{r},\omega)=P(\omega)\, \delta(\mathbf{r_0}\text{-}\mathbf{r})$, where $P(\omega)$ is the incident pulse spectrum. With this assumption, the incident field is,

$$\psi^{\text{inc}}(\mathbf{r},\omega) = P(\omega)\, G(\mathbf{r_0},\mathbf{r},\omega), \tag{32}$$

and equation (31) becomes

$$\psi_{\text{born}}^{\text{scat}}(\mathbf{r_0},\omega)= P(\omega)\, k_0^2(\omega)\int d\mathbf{r}G^2(\mathbf{r_0},\mathbf{r},\omega)o(\mathbf{r}) \tag{33}$$

where the squared Green's function is the result of the transmitter and receiver being located at the same point. Using equation (28), the forward model of the monostatic setup is expressed as follows

$$\psi_{\text{born}}^{\text{scat}}(\mathbf{r_0},\omega)= P(\omega)\, k_0^2(\omega)/(4\pi)^2\int d\mathbf{r}\ e^{i2k0(\omega)|\mathbf{r}_0\text{-}\mathbf{r}|}/|\mathbf{r_0}\text{-}\mathbf{r}|^2\ o(\mathbf{r}) \tag{34}$$

We will see later how this model differs in a bistatic setup owing to the fact that the transmitter and locater are not colocated anymore.

1.4.1 Green's function for the Helmholtz equation

It is important to give a brief discussion of the Greens function of the Helmholtz's equation at this juncture for the case of 2-D and 3-D. A detailed explanation and

derivation of the all equations discussed in this section can be found in Barton[43].

Following the notations used by Barton[43], we have the Green's function for the operator

in the wave equation $(-\nabla_{\mathbf{R}}^2 + ((1/c^2)\partial^2/\partial\tau^2$ where $\mathbf{R} = \boldsymbol{r}\text{-}\boldsymbol{r'}$ as they propagate is given by

Case I Three Dimensions

$$G_{0\tau} = \delta(\tau\text{-R}/c)/4\pi R \tag{34.1}$$

This disturbance is expanding shell with radius τc. Beyond this point there is no trace of

the disturbance which means there is no afterglow. Moreover, the Huygen's principle

works in 3D.

Case II Two dimensions

$$G_{0\tau} = 1/2\pi(\theta(\tau\text{-R}/c))/ (\tau/[\tau^2\text{-R}^2/c^2]^{1/2} \tag{34.2}$$

It can be seen that the impulse response rises steadily from zero to infinity. It becomes

infinity at τ=R/c and diminishes after this point. IT diminishes and faces to zero which

means there is an afterglow. The Huygen's principle does not work in 2D.

1.5 Time-domain ultrasound imaging

Time-domain image reconstruction techniques show how to reconstruct an image of a

point reflecting object from broadband pulse-echo data generated by translating a single,

omni-directional source-receiver over a suitable aperture. This means that the goal of a

broadband imaging system is to use the wide „temporal' frequency bandwidth (generated

by a large transmitting and receiving aperture), to obtain the complete information-
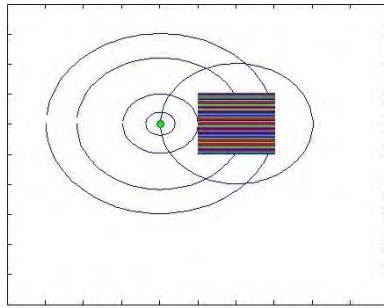

Figure 1. Monostatic setup of ultrasound tomography system. Shown here is the location of the point of transmitter/receiver (green) and few samples of radial projections.
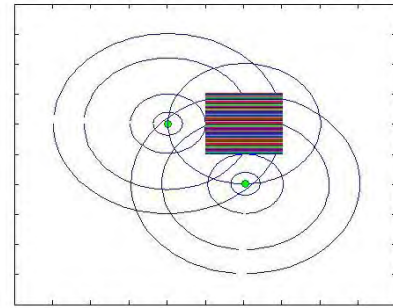

Figure 2. Moving the transducer to various locations (angular samples in addition to radial samples) on the circle, circular integrals are obtained over multiple intersecting paths.

bearing capacity of these signals. One of the earliest works which tackled the time-

domain found in the work of Norton [20].To explain this monostatic model, where the same

transducer acts as a transmitter and receiver (Figure 1), consider an infinitesimally short,

spatially diverging pulse that is emitted into a two-dimensional weakly reflecting

medium. If the reflected echoes are recorded at the same location (that is the location of

the transmitter), as a function of time, line integrals of the property of the medium under

study (e.g., reflectivity) over a family of concentric circles centered at this point are

obtained. This model could be understood by observing that a diverging circular

disturbance produced by two-dimensional isotropic source, at any point in time, produces

reflected waves simultaneously over the length of the arc illuminated by the wavefront at

that point in time. These echoes arrive back at the receiver at the same instant of time

where they are 'integrated' producing line integrals of the property of the medium over a

family of concentric circles (as a function of time). Several such data are obtained by

moving the transducer at various points (Figure 2) on the boundary (the boundary usually

being a circle). The data obtained are reconstructed using various methods, one of the

earliest being attempted in the work of Norton[20]. I will discuss some of the popular

reconstruction techniques in the next chapter. Though these reconstruction techniques do

not produce a perfect image because the system is limited by both finite temporal and

spatial frequency bandwidth (limited spatial frequency bandwidth because of finite

aperture), they improve the considerably improve the temporal-spatial system response

compared to the conventional delay-and-sum method of imaging[21].

1.5.1 Photo/thermo acoustic imaging

Several time-domain reconstruction techniques are used in a hybrid modality imaging

techniques known as a photo(thermo) acoustic imaging. Photoacoustic (PA) effect

reported by Alexander Graham Bell[22] is the basis for PA imaging. The phenomenon is

the generation of acoustic waves by the absorption of electromagnetic (EM) energy, such

as radio-frequency (rf) waves[23]. Photoacoustic imaging uses the high EM contrast at high

21

ultrasound resolution in large volumes of biological tissues[24].Similar to the transducer setup described in the previous subsection for the monostatic geometry, the acoustic waves due to PA effect generated by the initial sources inside the tissue reach the boundary with various time delays. The image resolution as a function of imaging depth is depended upon the detected ultrasonic bandwidth[25].With the help of temporal PA signal, depth-dependent information of the object can be determined. This is called PA depth profiling[26].

 Similarly, microwave induced themoacoustic imaging also exist in literature[27]. In this case, microwave pulses generate acoustic waves in a lossy medium. Although microwave-induced thermoacoustic imaging shares similar principles with photoacoustic imaging in the optical wavelength[28], it may have a wider use in medical imaging because microwaves penetrate deeper and more uniformly in biological tissues than light. Since, both these techniques in a tomographic setup share a similar model with the monostatic ultrasound tomography, we will consider only photoacoustic imaging.

1.5.2 Forward model based on spherical Radon transform

To image complex structures, in recent years, an imaging method called photoacoustic tomography (PAT) [29, 30] has caught wide attention. A forward model based for this imaging technique based on spherical Radon is similar to the monostatic ultrasound imaging.

Let the colored grid in figure 1 be a two-dimensional function $f(r,\theta)$ (describing for example, the reflectivity of the medium) defined in the inside of the circle of radius R. Let a short pulse of sound be emitted from a point (indicated in green color in figure 1) on the circumference at an angle ϕ measured from the positive x axis and the backscattered acoustic wave is recorded at the same point as a function of time. This generates line integrals over circles centered at this point. In other words, Spherical (or circular in two dimensional cases) Radon transformed projections. From a tomographic setup, this process of data acquisition is repeated on several points on the circumference (figure 2). The aim is to reconstruct $f(r,\theta)$ from circular integrals obtained from all the points on the circumference. To state symbolically, our aim is to reconstruct $f(r,\theta)$ from the following circular integrals:

$$g(\rho,\phi)= \int_{\ell(\rho,\phi)} f(r,\theta)\ ds \tag{23}$$

where $g(\rho,\phi)$ is the spherical Radon transform of $f(r,\theta)$. The path along which the function $f(r,\theta)$ is denoted by $\ell(\rho,\phi)$, which is a circle, parameterized by two variables ρ and ϕ, where ρ is the radius whose center lies on the point of measurement on the circumference of the enclosing circle at angle ϕ.

In a two-dimensional form equation (23) can be written in the following way:

$$g(\rho,\phi)= \int_{0}^{\infty}r\,dr \int_{0}^{2\pi} f(r,\theta)d\theta \times \delta\{[r^2 + R^2 -2rR\cos(\phi-\theta)]^{1/2} - \rho\} \tag{24}$$

the delta function follows the circular path in the (r,θ) plane.

Equation (24) is the forward model based on the spherical Radon for monostatic ultrasound imaging. The same is applicable to photoacoustic imaging with a slight modification in the model. In the latter, there is no "emitter" because the acoustic waves are generated by a different mechanism (photoacoustic effect), but only the receiver. There are several reconstruction techniques to recover $f(r,\theta)$ which I will discuss in the next chapter.

1.5.3 Inverse source problem in photo/thermo acoustic tomography

As mentioned in the previous section, in the scheme of photoacoustic tomography, there are only receivers and no transmitters. Since, the acoustic waves are generated inside the object at some source, the problem of reconstructing the object from the data acquired by the receivers is called the "inverse source problem". Each temporal photoacoustic signal, measured at various locations of the receivers, provides one- dimensional radial information about the photoacoustic source relative to the receiver location. Often small-aperture receivers are used to approximate point detectors, which receive photoacoustic signals originating from spherical (circular in 2D) shells centered at each point detector, with the radius determined by the acoustic times of flight. For large aperture detectors, the reconstruction algorithms are different. One such reconstruction is attempted in [31]. Let us assume a heat source $H(\mathbf{r}, t)$, and a pressure to its response at position $\mathbf{r}$ and time t, $p(\mathbf{r}, t)$ in a homogeneous medium. Following the notations of Xu[24], the pressure would

follow the following wave equation, ignoring effects of thermal diffusion and kinematic

viscosity[32]:

$$\nabla^2 p(\mathbf{r}, t) - 1/c^2\, \partial^2/\partial t^2\, (p(\mathbf{r}, t)) = -\beta/C_p\, \partial/\partial t\, (H(\mathbf{r}, t)) \tag{25}$$

where β is the isobaric volume expansion and C_p is the specific heat[33].

The solution to equation (25) is expressed by

$$p(\mathbf{r}, t) = \beta/4\pi C_p \iiint d^3\mathbf{r'}/|\mathbf{r}\text{-}\mathbf{r'}|\, \partial/\partial t'\, (H(\mathbf{r'}, t'))\, |_{t'=t-|\mathbf{r}\text{-}\mathbf{r'}|/c} \tag{26}$$

The heating function can be written as a product of two separable variables, spatial

absorption function and the condition of thermal confinement,

$$H(\mathbf{r}, t) = A(\mathbf{r})I_e(t) \tag{27}$$

Now equation (26) can be written as a convolution between the temporal profile $I_e(t)$ and

the acoustic wave form $p_\delta(\mathbf{r},t)$ that is excited by an infinitesimally short pulse $\delta(t)$,

$$P_e(\mathbf{r}, t) = \int_{-\infty}^{\infty} I_e(t-\tau) p_\delta(\mathbf{r},\tau) d\tau \tag{28}$$

where

$$p_\delta(\mathbf{r},t) = \partial/\partial t[\, 1/4\pi \iint_{|\mathbf{r}\text{-}\mathbf{r'}|=ct} p_0(\mathbf{r'})\, d\Omega'\,]\,, \tag{29}$$

where $d\Omega'$ is the solid-angle element of vector $\mathbf{r'}$ with respect to the point at $\mathbf{r}$; and $p_0(\mathbf{r})$

is the initial pressure excited by a $\delta(t)$ electromagnetic source, computed by

$p_0(\mathbf{r}) = \Gamma(\mathbf{r})A(\mathbf{r})$, which acts as the source for the propagating acoustic wave.

Let us assume a very simple electromagnetic source $\delta(t)$, and the photoacoustic signal is

detected at the location $\mathbf{r}_0$ by a point detector. The signal detected at that transducer can

be symbolically written as,

$$P_d(\mathbf{r}_0,t)= \partial/\partial t[\ 1/4\pi \iint_{|\mathbf{r}-\mathbf{r'}|=ct} p_0(\mathbf{r})\ d\Omega\ ] \tag{30}$$

where $d\Omega$ is the solid-angle element of vector $\mathbf{r}$ with respect to the point at $\mathbf{r}_0$.

The goal is reconstruct $p_0(\mathbf{r})$ from the acquired data $P_d(\mathbf{r}_0,t)$.

1.5.4 Relationship between the acquired data and the Radon transformed projections

Rewriting equation (30), we obtain,

$$F(\mathbf{r}_0,t)= 4\pi/t \int_0^t P_d(\mathbf{r}_0,t)\ dt = \iint_{|\mathbf{r0}-\mathbf{r'}|} p_0(\mathbf{r})\ d\Omega \tag{31}$$
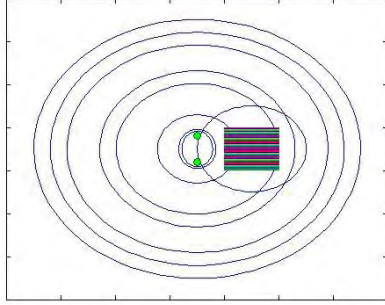
Figure 3. Bistatic setup of ultrasound tomography system. Shown here is the locations of the points of transmitter and receiver (green) and few samples of "radial" projections.
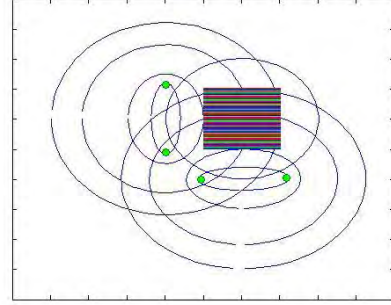
Figure 4. Bistatic setup of ultrasound tomography system. Shown here is the locations of the points of transmitter and receiver (green) at various angular positions and few samples of "radial" projections.

The Radon transfo location of the detectors which is usually on a circumference of a circle centered at the center of the object and t is the time at which "radial" projections are obtained.

The Radon transform approximation yields good results for circular detection geometry. All the reconstruction techniques existing for the circular detection geometry hold well only when the center of the object is centered at the center of the circle. Significant artifacts appear when the source deviates from the center. Another important assumption in most of the time-domain reconstruction techniques is that the speed of sound, c, is constant inside the medium. This assumption is reasonable because the variation in the speeds of sound in biological medium is very less.
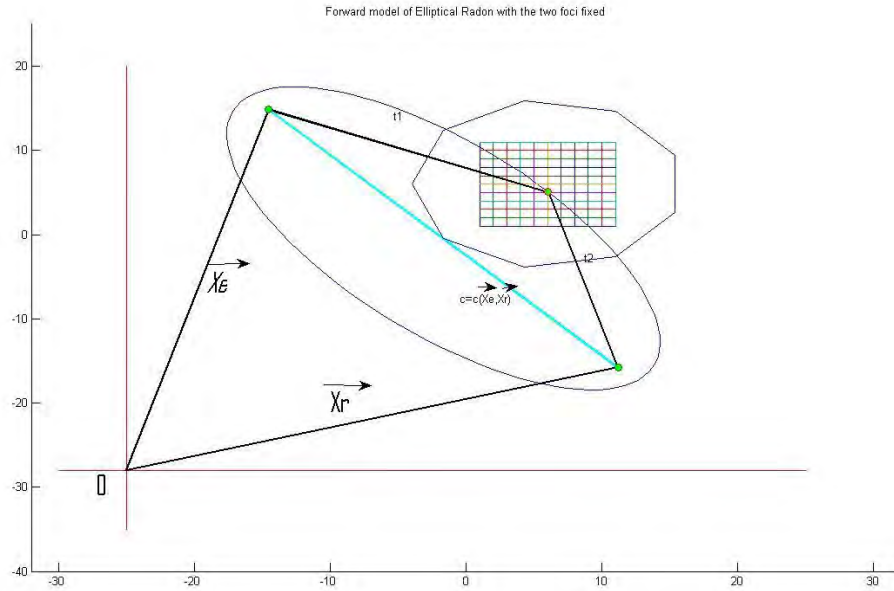
Figure 5. Definition of an ellipse. As can be seen from the figure, an ellipse has five degrees of freedom.

There are other approximations which have been attempted wherein a 2D Radon transform was approximated with a Hilbert transform[37]. The most common form of reconstruction, backprojection for tomographic data, will be discussed later.

1.5.5 Bistatic time-domain ultrasound imaging (Elliptical Radon transform-based imaging)

Unlike monostatic setup in ultrasonic imaging, in bistatic setup the locations of the source and the detector differ. In this respect, monostatic imaging can be considered a special case of bistatic imaging. Whenever the source and the sensors are not at the same location, surfaces of constant time of flight are ellipses, whose foci are the locations of the transmitting and receiving transducers.

Some conventional medical imaging systems like focus-and-steer imaging[34] and synthetic-focus imaging[35] with complete dataset include the effects of backscattered signals acquired by detectors not at the same location as the source. Image reconstruction using elliptical projections can also be found in applications like Synthetic Aperture Radar (SAR) imaging[36]. The geometric setup used in this modality is not appropriate for medical imaging.

<u>A. Parameters of an ellipse and the elliptical Radon</u>

Consider an ellipse (Figure 5) with foci at $\mathbf{x_e}$ and $\mathbf{x_r}$. The family of ellipses at these foci

has semi-major axis a, semi-minor axis b and a foci separation of $2c=|\mathbf{x_e} - \mathbf{x_r}|$. The vector

form of ellipse can be written as

$$|\mathbf{x\text{-}x_e}| + |\mathbf{x\text{-}x_r}| = 2a \tag{32}$$

Next, we make an identity linking the a and c with the *eccentricity e* of the ellipse,

$$a=c/e \tag{33}$$

implying,

$$|\mathbf{x\text{-}x_e}| + |\mathbf{x\text{-}x_r}| = 1/e \; |\mathbf{x_e\text{-}x_r}| \tag{34}$$

e is defined the domain $0 \leq e < 1$.

One possible definition of elliptical Radon would therefore be

$$R_{\mathbf{xe,xr}}(e) = \int_{|\mathbf{x\text{-}xe}| + |\mathbf{x\text{-}xr}| = 1/e \; |\mathbf{xe\text{-}xr}|} f(\mathbf{x}) \; ds \tag{35}$$

There are five parameters in this expression. If we additionally require that the semi-

major axis be orthogonal to a line, then the number of degrees of freedom can be reduced

to four. At present, nothing is known about the analytical inversion of this transform.

Even a Fourier slice theorem is lacking. The earliest known approximate reconstruction

was attempted in 1989[38].

To define the elliptical Radon, consider the locations of a transmitter and a receiver on xy plane on the y axis with y coordinates +/- d from the origin. Then a pulse moving from the transmitter to the receiver from a point (x, y) in the plane travels a distance A:

$$A= \sqrt{h^2 +(y+d)^2 + x^2} + \sqrt{h^2 +(y-d)^2 + x^2} \qquad (36)$$

The signal arriving at the receiver at a time instant t=A/c is that due to all signals which have traveled a distance A. the geometry dictates that the signal must have reflected from the loci in the xy plane given by a re-arrangement of equation (36):

$$x^2 + y^2 = (1-4d^2/A^2) = A^2/4 - d^2 \qquad (37)$$

which is an ellipse centered at the origin with A and d being constants.

To convert the expression from time-dependent equation to a spatial one, we introduce a new variable $r^2 = A^2/4 - d^2$, we have

$$x^2 + y^2(r^2/ r^2+d^2) = r^2 \qquad (38)$$

where the semi-minor axis which lies on the x axis and is of length r and the semi-major axis lies on the y axis and is of length

$$y_r = r\sqrt{(r^2 +d^2)/r^2} \qquad (39)$$

It can be seen clearly, when d=0 (monostatic case), y_r= r which is the same length as the semi-minor axis, indicating the geometry is a circle. The aspect ratio of the ellipse is defined as the ratio of its semi-minor axis to the semi-major axis. It can been that the aspect ratio of the ellipse defined above changes smoothly from $\sqrt{1+d^2}$ for small r to 1 for a circle. The ellipse will start appearing like a line for large d.

If the ellipses are parameterized using polar coordinate,

$$x = r\cos\theta \tag{40}$$

$$y = r\sqrt{(r^2 + d^2)/r^2}\ \sin\theta \tag{41}$$

then the "elliptical" measurement at the receiver, with ellipse centered at the origin, and the time corresponding to the radius r, is

$$F(r) = \int\limits_{-\infty}^{\infty} \int\limits_{\infty}^{\infty} f(x,y)\delta(x^2 + y^2\ (r^2/r^2 + d^2) - r^2)\ dxdy$$

$$= r\int\limits_{0}^{2\pi} f(r\cos\theta, r\sqrt{(r^2 + d^2)/r^2}\ \sin\theta)\sqrt{1 + (d\cos\theta/r)^2}\ d\theta \tag{42}$$

where the differential length dl of the line integral is written in terms of the integration variable $d\theta$ as:

$$dl = r\sqrt{1 + (d\cos\theta/r)^2} \tag{43}$$

Equation (42) gives a generalized elliptical Radon transform.

B. An engineering derivation of the elliptical Radon model from the time-dependent wave equation

Starting with the wave equation in the time-domain, we have

$$(\nabla^2 - \partial_{tt})\ u(\mathbf{r},t) = s(\mathbf{r},t) \tag{44}$$

For a non-zero eigenvalue, the Green's function exists, given by

$$LG\ (\mathbf{x},\ \mathbf{x'}) = \delta(\mathbf{x\text{-}x'}) \tag{45}$$

where $L=(\nabla^2-\partial_{tt})$, and

$$Lf(\mathbf{x})=s(\mathbf{x}) \tag{46}$$

which implies,

$$f(\mathbf{x})=\int_{B.C} s(\mathbf{x'})\ G(\mathbf{x},\mathbf{x'})\ d\mathbf{x'} \tag{47}$$

Now,

$$(\nabla^2-\partial_{tt})p(\mathbf{r},t,\mathbf{r'},t') = \delta(\mathbf{r\text{-}r'}) \tag{48}$$

$$p(\mathbf{r},t,\mathbf{r'},t') = 1/(4\pi|\ \mathbf{r\text{-}r'}|)\ \delta(t\text{-}t' - |\mathbf{r\text{-}r'}|) \tag{49}$$
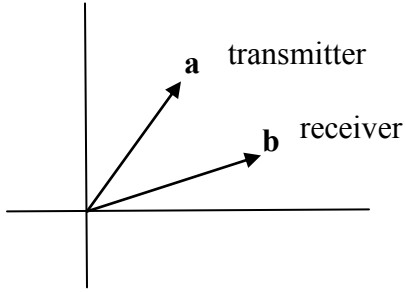
Figure 6. Position vectors of the transmitter and the receiver which act as the foci of the ellipse

We use p($\mathbf{r},t,\mathbf{r'},t'$) to propagate signal from source to scatterer, and then from scatterer to receiver. Using the implicit Born approximation for single scatterer, we calculate incident field,

$$(\nabla^2-\partial_{tt})\ u_i(\mathbf{r},t) = \delta(\mathbf{r\text{-}a})\ \delta(\mathbf{t\text{-}0}) \tag{50}$$

scattered field,

$(\nabla^2 - \partial_{tt})\ u_s(\mathbf{r},t) = o(\mathbf{r})u_i(\mathbf{r},t)$ \hfill (51)

Using the positional vectors, we derive,

incident field,

$u_i(\mathbf{r},t) = p(\mathbf{r},t,\mathbf{r'} = \mathbf{a}, t' = 0) = 1/(4\pi|\mathbf{r}\text{-}\mathbf{a}|)\ \delta(t - |\mathbf{r}\text{-}\mathbf{a}|)$ \hfill (52)

and the scattered field,

$(\nabla^2 - \partial_{tt})\ u_s(\mathbf{r},t) = s(\mathbf{r},t)$ \hfill (53)

where,

$s(\mathbf{r},t) = 1/(4\pi|\mathbf{r}\text{-}\mathbf{a}|)\ o(\mathbf{r})\ \delta(t - |\mathbf{r}\text{-}\mathbf{a}|)$ \hfill (54)

where $o(\mathbf{r})$ is the scattering object.

Solving for the scattered field, we get,

$u_s(\mathbf{b},t) = \int_{t',\mathbf{x'}} s(\mathbf{r},t)\ G(\mathbf{b},t,\mathbf{r},t')d\mathbf{x} = 1/(4\pi)^2 \int o(\mathbf{r})/|\mathbf{r}\text{-}\mathbf{a}|\ \delta(t - |\mathbf{r}\text{-}\mathbf{a}|)\ \delta(t\text{-}t'\text{-}|\mathbf{b}\text{-}\mathbf{r}|)d\mathbf{x}dt$ \hfill (55)

where

$\delta(t - |\mathbf{r}\text{-}\mathbf{a}|)\ \delta(t\text{-}t'\text{-}|\mathbf{b}\text{-}\mathbf{r}|) = \delta(t - |\mathbf{r}\text{-}\mathbf{a}|\text{-}|\mathbf{b}\text{-}\mathbf{r}|)$ \hfill (56)

Equation (55) gives the wave form in time-domain as an elliptical Radon transformed projection..

CHAPTER II

REVIEW OF LITERATURE

The problem of recovering a function from a subset of its spherical means, which has applications in both photo/thermo acoustic tomography and monostatic imaging, has been of interest to applied mathematicians and engineers for several years. One of the first works to tackle this problem was the seminal paper also by Norton[39]. The author was interested in the problem in the scheme of ultrasound reflectivity problem and this paper dealt with the geometry where spherical radon transformed projections are obtained on locations on a circumference of a circle. In an earlier paper[20] by the same author, the same line-integral model was used for an analysis of a reflectivity reconstruction problem. But here, the problem was analyzed for the case of an omni-directional source-receiver moved along a straight line in the boundary of a half-plane. That kind of a modeling would be appropriate for Synthetic Aperture Radar (SAR) imaging. During the time his paper was published[39], most of the acoustical imaging systems in medical diagnosis employed highly directional sources and receivers (like the traditional single probe system) to provide resolving power transverse to the direction of propagation whereas the solution to the reflectivity reconstruction problem in his paper was the basis for a high-resolution, tomographic imaging techniques that employs omnidirectinal transducer elements like the one shown in Figure 6.
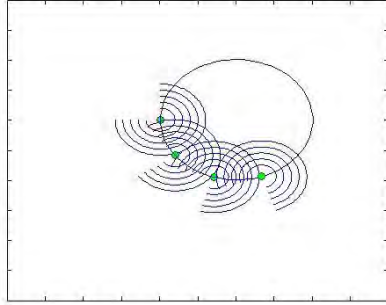
Figure 6. When an omnidirectinal element sends out a pulse and measure the echoes back as a function of time, line integral over circular paths of reflectivity are measured.

The reconstruction to the problem is obtained by deriving a relationship expressing the all the circular harmonic coefficients of the function to be recovered in terms of the projections obtained at each angular location. This, approach, which may be termed the method of circular harmonic decomposition, is possible because of the problem's inherent circular symmetry. That is precisely the reason why the same approach cannot be done with elliptical Radon transformed projections because they lack symmetry. Then a Hankel transformation is performed on each harmonic coefficient to yield the corresponding harmonic coefficient of the original function. Finally, the function is recovered by inserting the harmonic coefficients into the angular Fourier series. In essence, the method suggested in this paper can be made to resemble a convolution-backprojection operation. It is easy to perceive that as the radius of the enclosing circle becomes large relative to the size of the object, the integration paths intersecting the object approach straight lines. In that case the convolution-backprojection formulation reduces to that of conventional computerized x-ray tomography.

As mentioned previously, if the measurements are made in the far field with respect to the scattering region, where the Born approximation is usually applicable, then the scattering distribution and the scattering measurements bear a simple Fourier transform relationship to each other[41]. But in a practical medical imaging system Born approximation is impractical because the far-field approximation imposes unreasonable constraints on imaging distances. Without the far-field approximation exact inversion formulas are obtained by some authors using monochromatic illumination[42.] But these solutions are derived under the assumption of weak scattering using the first-order Born or Rytov approximations as mentioned in the previous chapter. But a three-dimensional inverse scattering problem was examined for the more general case of broad-band illumination without a far-field approximation[40]. Here, broad-band omnidirectional spherical waves are assumed to be the incident waves.

In frequency domain, there is another wave-based tomographic imaging algorithm that was developed based upon a single rotating radially outward oriented transducer[8]. The geometrical setup is similar to the one shown in Figure 2. But since this is a frequency domain imaging technique, a spherical Radon model is not appropriate, but the acquisition of data is very similar to it. At each angular location at a fixed radius, the transducer launches a primary field and collects the backscattered field in what is called a "pitch/catch" operation. This is similar to the medical intravascular ultrasound systems (IVUS). IVUS systems use conventional ultrasound imaging called the B-mode imaging. Goss[8] develops a wave-based imaging algorithm using diffraction tomography

techniques. In his work a mutimonostatic mode is used for data acquisition.

Mutimonostatic is a terminology used when a single transducer is rotated along the

circumference of the circle as opposed having many transducers on a circle and sending

and receiving signals at the same time. The implementation of this model reduces the

hardware resources and also interference effects of acoustic waves. The author derives an

analytic expression for the multimonostatic inverse and uses Hilbert space inverse wave

algorithm to construct images.

In recent years researchers have taken interest time-domain reconstruction algorithms

based on spherical Radon transformed model because if its applications in

photo/thermoacoustic tomography. A limitation of these methods is that the Radon

transform model is appropriate only when then medium is insonified by an impulsive

(infinite bandwidth) wave. When pulses of finite bandwidth are employed, image quality

can be compromised significantly[44]. But the existing frequency-domain algorithms

provide high quality images for many numbers of discrete frequencies that is

computationally very demanding. Some authors have worked on time-domain waveform

for inverse scattering methods by the method of frequency decomposition to work the

spatial Fourier transform[46] and others on quantitative time-domain imaging[45].

The earliest known spherical Radon transform based image reconstruction was

investigated by Norton[39]. The paper was based on circular harmonic decomposition.

But only recently, a paper provided a filtered-back projection (FBP) based reconstruction

for the spherical Radon transformed data in 2-D[47]. FBP algorithms for 3-D have existed

for a longer time. The authors provide a log-based filter to invert spherical Radon

transformed data in even dimensions. If the spherical Radon transform Mf of a function f

is defined in the following way,

$$(Mf)(x,r)=1/|S^{n-1}|\int_{S^{n-1}} f(x+r\theta)\, dS(\theta) \tag{57}$$

where $|S^{n-1}|$ denotes the area of S^{n-1} in $\mathbf{R}^n$ and ds (θ) denotes the area measure on the

sphere which in two-dimensions would be arcs.

The reconstruction formula suggested in the Finch[47] paper is (following the notations of

the paper),

$$f(x)= 1/2\pi R_0 \int_S \int_0^{2R_0} \partial_r r \partial_r (Mf)(p,r) \log |r^2 - |x-p|^2|\, drds(p) \tag{58}$$

where R_0 is the radius of the circle on which the detectors are placed, p is the angular

location of the detectors and r is the radius over which the circular integrals are measured

with p as center.

An explicit representation for the wave is given in terms of the spherical radon transform,

$$u(p,t)=1/(n-2)!\partial_t^{n-2} \int_0^t r(t^2 - r^2)^{(n-3)/2} (Mf)(p,r)dr \tag{59}$$

where n gives the dimension. Interesting to note here is that this solution to the initial

value problem gives u as a function of time t, whereas the conventional image

reconstructions are for a constant time.

One of the earliest attempts to reconstruct elliptical Radon transform data approximately was attempted in[38]. Each elliptical Radon transformed projection is back projected with a weight that is equal to the product of the distance of a point on the ellipse from the two loci. Recently, authors have attempted[48] a Fourier transform based image reconstruction for ellipsoidal projections. The work does not clearly define and explain the elliptical Fourier transform.

CHAPTER III

METHODOLOGY

In the background section we saw several formulas to reconstruct a function from the

spherically Radon transformed data. In theory all these formulas assume continuous

functions. In real applications that would mean obtaining infinite amount of data which is

practically not feasible. For example, we can have only a fixed number of detectors for

the monostatic setup or move a single transducer at fixed number of angular locations.

For the monostatic setup, the numerical implementation of the filtered backprojection

algorithm derived in[47] 100 equally spaced angular samples and 100 equally spaced radial

samples were used.

The discrete version of the forward problem[47] can be stated as follows,

$$F^{k,m} = (Mf) (p^k, r^m), \qquad\qquad (60)$$

where F is the spherical Radon transformed projections, p^k is the angular location given

by,

$p^k = R_0(\cos(kh_\phi), \sin(kh_\phi))$ where k runs from 0 to 100 in steps of 1 and $r^m = mh_r$ where h_ϕ

is the angular spacing given by 0.0622 radians (2π divided by angular samples) and h_r is

the radial spacing which is equal to 1.4142 "pixel" units. The radius of the circle R_0 on

which the transducers are placed are determined by half of the diagonal of the size of the

square object which is 100 pixels each side. The radial spacing is obtained by dividing

the diameter of this circle by the number of radial samples.

To implement equation 58 to reconstruct the function we need to calculate the partial

derivative with respect to r. To be exact, we need to calculate the $\partial r + r\partial_r^2$ of the obtained

projections. To discretize differentials, we approximate with symmetric finite differences of the samples in the projection $F^{k,m+1}-F^{k,m-1}/2\ h_r$ and for the second order partial derivatives, we use $F^{k,m+1}-F^{k,m-1}-2F^{k,m}/\ h_r^2$. The discrete version of the entire expression of $\partial r+r\partial_r^2$ acting on the projection would be as follows,

$$1/\ h_r((m+1/2)\ F^{k,m+1} + (m-1/2)F^{k,m-1} - 2mF^{k,m}$$ (61)

where $F^{k,-1}=F^{k,Nr+1}=0$ because of the boundary conditions.

Now, the integration along circular paths over all angles is performed by linear spline interpolation, interpolating the projections at the positions r^m. The discrete version of the interpolation operator is defined as follows

$$T^k[G](r)= F^{k,m}+ r{-}r^m/h_r(F^{k,m+1}-F^{k,m})$$ (62)

where r is in between two consecutive radial samples r^m and r^{m+1}. Therefore the discrete version of the entire equation (58) is as follows

$$\sum_{m'=0}^{Nr-1} a_{m'}^m F^{k,m'} +1/\ h_r \sum_{m'=0}^{Nr-1} b_{m'}^m (F^{k,m'+1} - F^{k,m'})$$ (63)

where

$$a_{m'}^m = [\{r-r^m)\log |r-r^m|+r+r^m \log |r+r^m|-2r]_{r=r^{m'}}^{r^{m'}+1}$$ (64)

$$b_{m'}^m = -r^{m'} a_{m'}^m +1/2[(r^2 - (r^m)^2)\log |r^2 -(r^m)^2|-r^2]_{r=r^{m'}}^{r^{m'}+1}$$ (65)
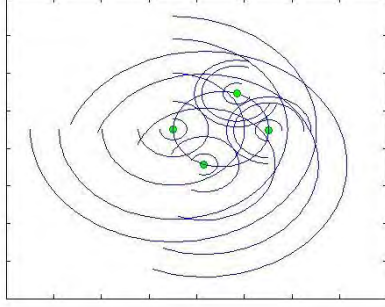
Figure 7. Exterior data acquisition. If the object is at the top right of the ring of detectors, the detectors on the left half of the ring will have a higher radial spacing than the right half

Finally, the discrete version of the back-projection operator[47] is given by

$$\frac{1}{(N_\phi+1)} \sum_{k=0}^{N_\phi} F(|\, x^i - p^k\,|)\,, \quad x^i \epsilon\, D \tag{66}$$

The computational efforts are $O(N^3)$ for the FBP because all $(N+1)^2$ reconstructions for the points in the image, $N_\phi+1$ summations must be done. Here $N=N_\phi=N_r=100$. The reconstructions were performed when both the object was inside the ring of detectors and exterior to it. In the exterior case, there were more radial samples from one half of the ring of detectors like shown in Figure 7. In this case, the object to be reconstructed is on the top right of the ring of detectors; the detectors on the left half of the ring of detectors will have more radial spacing than the right half. The radial spacing increase proportionately as the distance between the ring of detectors and the object increases. For the bistatic case, the distance between the transmitter and the receiver remain constant throughout data acquisition. This would geometrically mean that the distance between the two foci of the ellipse remain constant. In addition, a further constraint was imposed that the major axis remains tangential to the circle on which the pair of transducers are rotated. The center of the ellipse, the mid-point of the major axis is the angular location e^k, where k runs from 0 to 100 with an angular spacing of 0.0622 radians.

We are at a position to define the eccentricity ϵ of an ellipse. If the major axis of the ellipse is a and the minor-axis b, then the eccentricity is defined as a follows

$$\epsilon = \sqrt{1 - (b/a)^2} \qquad (67)$$

And the distance from the center to either focus is ae which is equal to $\sqrt{a^2 - b^2}$. In my numerical implementation of the forward model, the distance between the foci remains constant. If the constant is c, then for linear samples of major axes $a^m = ma_r$, where m runs from 0 to 100 in steps of 1 ($a_r=1$), then the samples of minor axes are calculated as follows,

$$b^m = \sqrt{(a^m)^2 - c^2} \qquad (68)$$

which means the samples of minor axes do not increase in a linear fashion.

For the backprojection, the projections were smeared aback along elliptical arcs with the filter that was used in the monostatic setup. Here, the log based filter had values of samples of minor axes as opposed to the radial samples in the case of mono-static setup. In the case of multi-bi-static setup, where there are more than one receiver per transmitter, the filter contained samples of eccentrities of the ellipses instead of the radial samples. In this case, the eccentrities start from zero (where an ellipse is a circle) and approach towards the value 1 as a the receiver moves farther away from the transmitter on a circle and moves back to the value 0 as the pair of transducers get closer.

CHAPTER IV

FINDINGS

In this section, I will present the results for the FBP reconstructions of phantoms for various geometrical setups. For the monostatic setup, a 100X100 Shepp-Logan phantom was used (figure 8).

Figure 7. 100X100 Shepp-Logan phantom
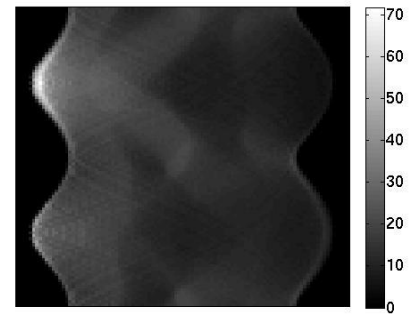
Figure 8. The corresponding sinogram of the phantom

For $N=N_{\phi}=N_r=100$, for a total angular data acquisition of 360 degrees, the corresponding sinogram of the Shepp-Logan phantom is shown in Figure 8.

The reconstructed image using the FBP algorithm mentioned in the methodologies section is shown in Figure 9.
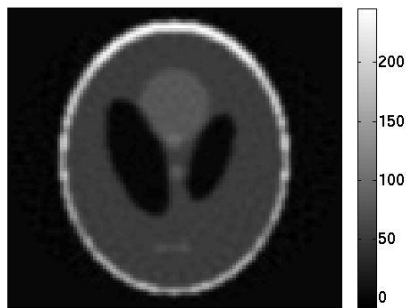
Figure 9. The reconstructed image from the obtained sinogram using the FBP method

The following image shows the reconstruction of a point source (Figure 13).
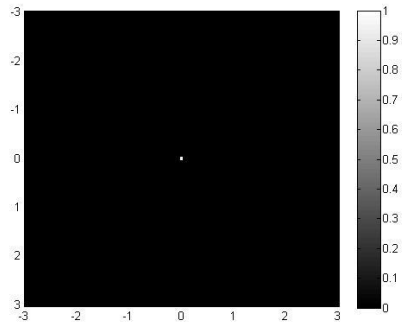
Figure 10. A point source at origin
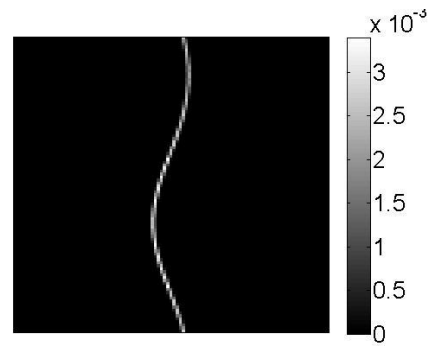
Figure 11. Sinogram of a point source at origin
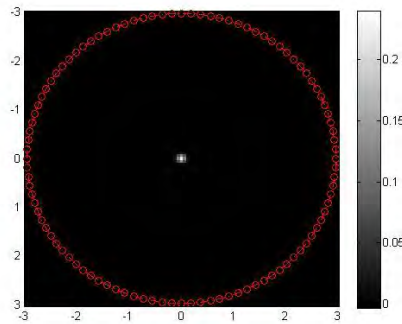
Figure 12. Reconstruction of a point source

Next, for the phantom shown in Figure 13, the algorithm was used to reconstruct the
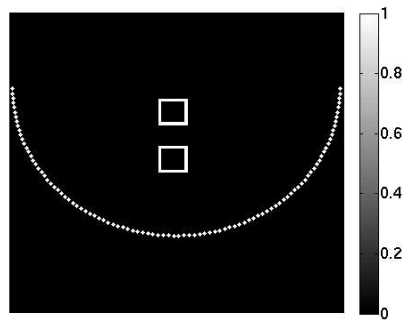
Figure 13. The phantom used for partial reconstruction. The location of the detectors is shown with white dots.

object from half the data. This kind of modeling is most appropriate for breast cancer imaging using the tomographic modality. The corresponding sinogram and the reconstruction are shown in Figures 14 and 15 respectively. In this case $N=N_\phi=N_r=100$ with an angular coverage of 180 degrees.
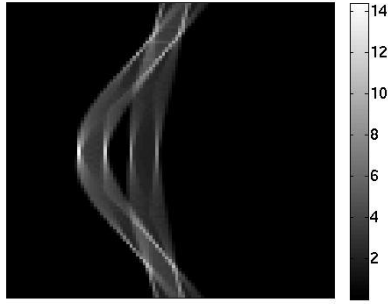
Figure 14. The sinogram of the phantom shown in Figure 10 for partial angular coverage
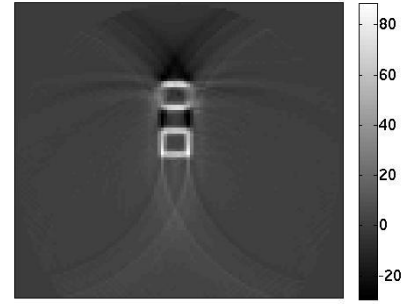
Figure 15. Reconstruction of phantom shown in fiure 10 for partial angular coverage

For the case of exterior reconstruction, where the object was placed exterior to the ring of detectors (top right to the ring of detectors, with the center of the object 2N pixels from the center of the ring of detectors with radius of $\sqrt{2}$ N pixels. In this case N= N_ϕ= N_r=100 but the radial spacing for the detectors on the left half is twice that of the right half. The phantom used is shown in Figure 7 and the corresponding sinogram is shown in Figure 16 and the reconstruction using FBP is shown in Figure 17.
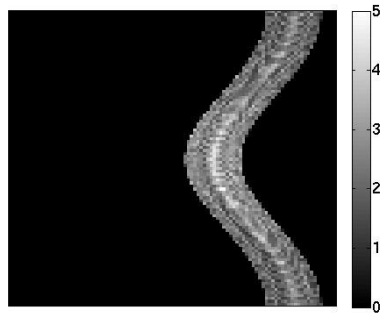
Figure 16. The sinogram obtained for an object placed exterior of the ring of detectors
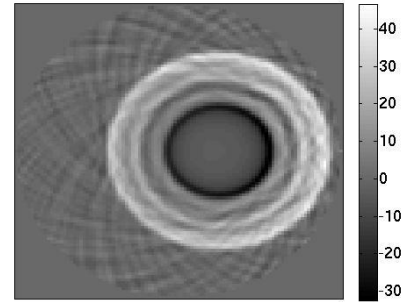
Figure 17. The reconstruction with artefacts for the exterior case.

To understand the behavior of the filter for the bistatic case, a different phantom was used as shown in Figure 18. It is a 100X100 binary phantom with a square in the middle of the phantom of 100 pixels each side.
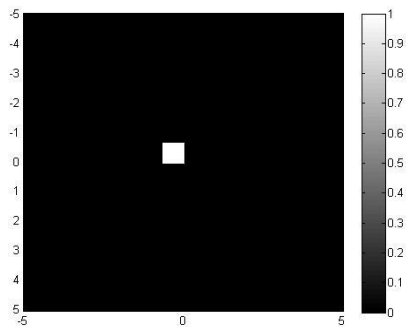

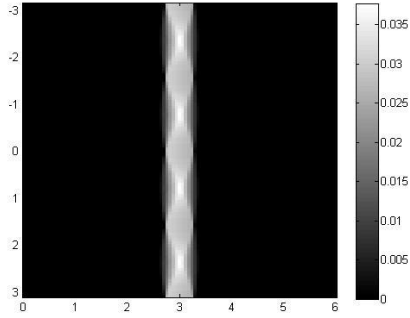**Figure 18. 100X100 binary phantom used with a square in the middle of 10 pixels each side.**

Figure 19. Sinogram of the phantom shown in Figure 15
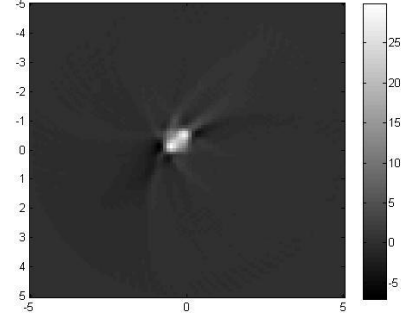
Figure 20. The reconstructed object

For N= N_ϕ= Na=100, and for a angular coverage of 360 degrees, the corresponding sinogram is shown in Figure.19. The reconstructed object is shown in Figure 20. Since, the filter is a „computational' quantity and to understand its spatial behavior, the square on the binary phantom was spatially moved. The following images were moved along the x-axis with no change in the y-axis. The image was moved every 2-pixels on either side of the center. To conserve space, few are shown here. A graph comparing the spatial location and the error in reconstruction will follow.
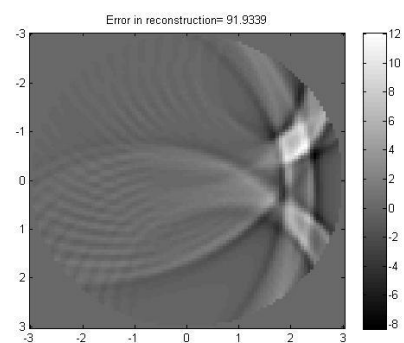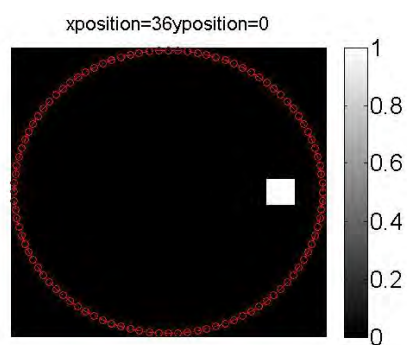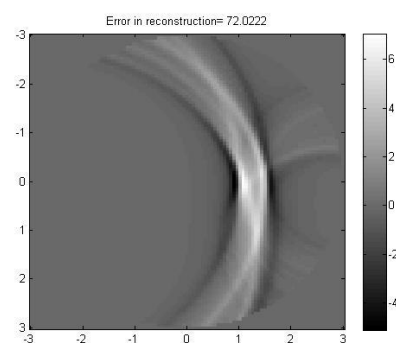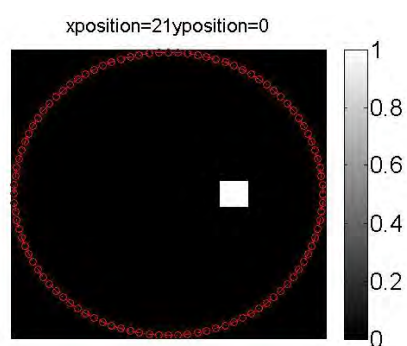
xposition=15yposition=0

Error in reconstruction= 87.886

xposition=21yposition=0

Error in reconstruction= 72.0222

xposition=36yposition=0
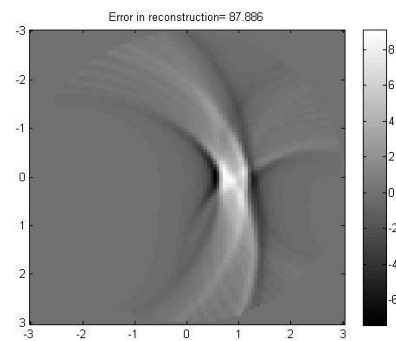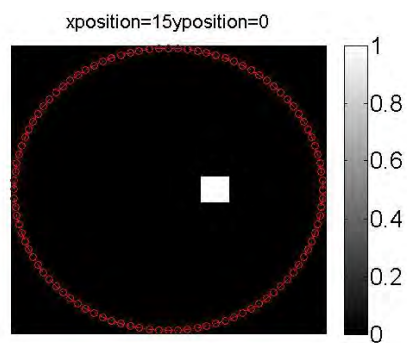

Error in reconstruction= 91.9339
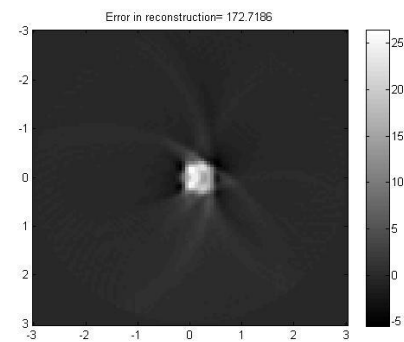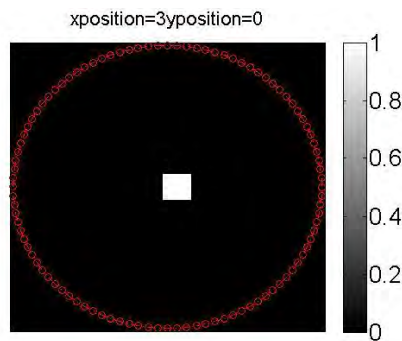
Figure 21. Phantom moved along positive x-axis while no change in y-axis

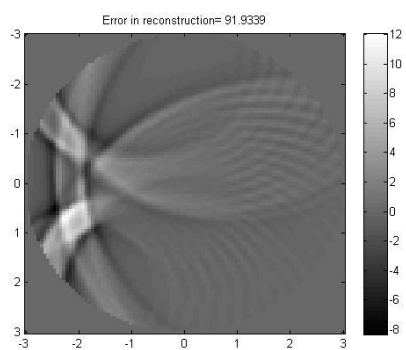**Figure 22. Corresponding reconstructions**

49

xposition=-3yposition=0

Error in reconstruction= 172.7186

xposition=-21yposition=0

Error in reconstruction= 72.0222

xposition=-36yposition=0

Error in reconstruction= 91.9339
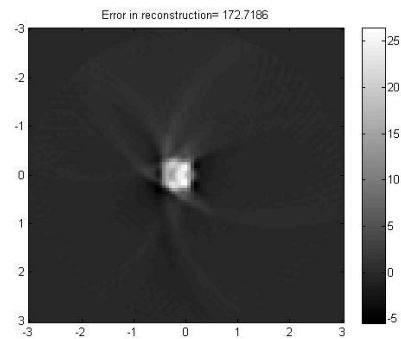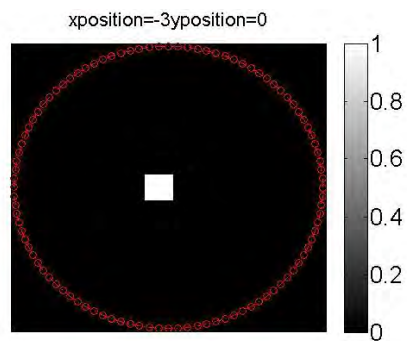
Figure 23. Phantom moved along negative x-axis while no change in y-axis

Figure 24. Phantom moved along positive x-axis while no change in y-axis

50

xposition=0yposition=3

xposition=0yposition=6

xposition=0yposition=39
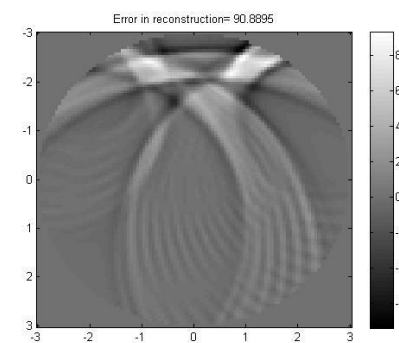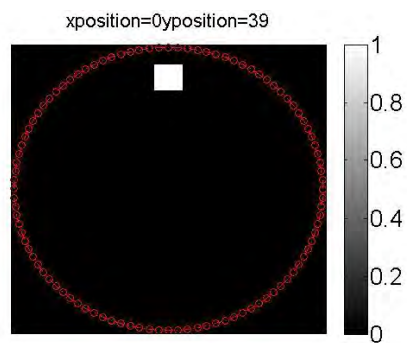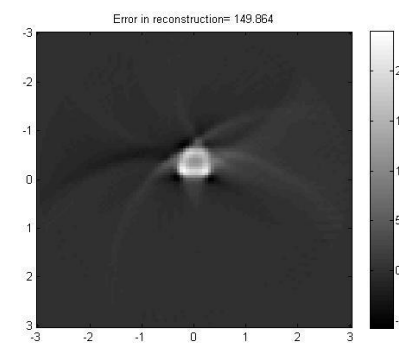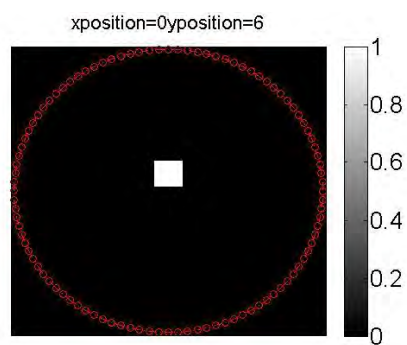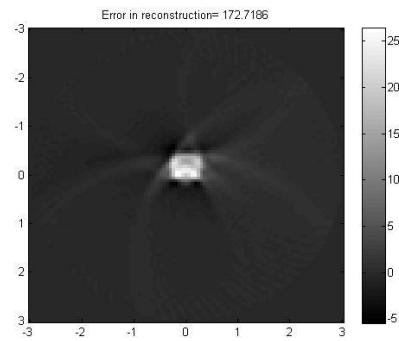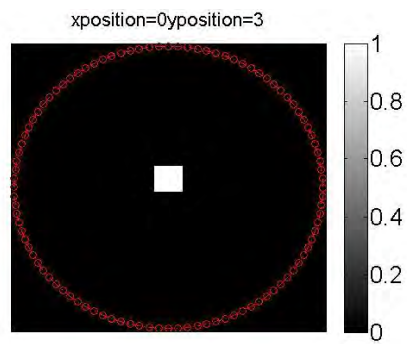
Figure 25. Phantom moved along positive y-axis while no change in x-axis

Error in reconstruction= 172.7186

Error in reconstruction= 149.864

Error in reconstruction= 90.8895

Figure 26. Corresponding reconstructions

51

xposition=0yposition=-6

Error in reconstruction= 149.864

xposition=0yposition=-15

Error in reconstruction= 87.886

xposition=0yposition=-39

Error in reconstruction= 90.8895
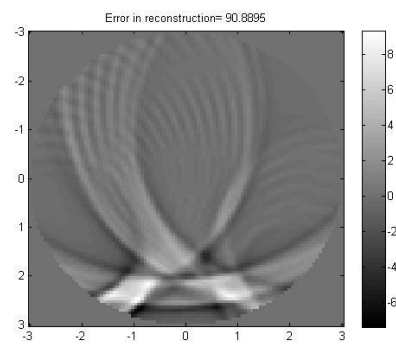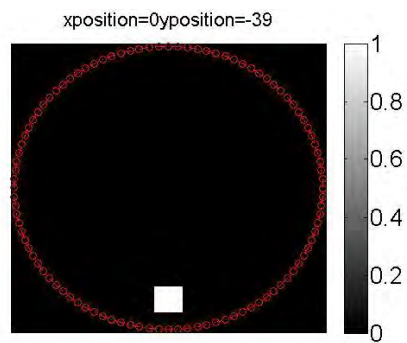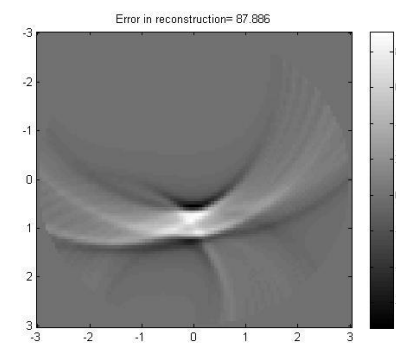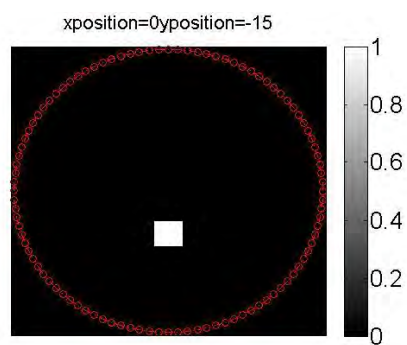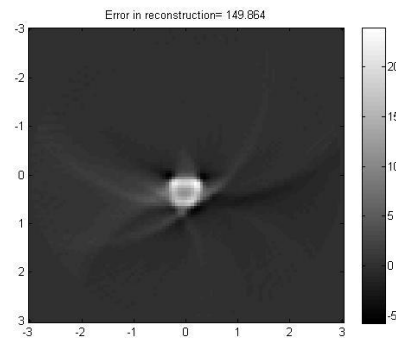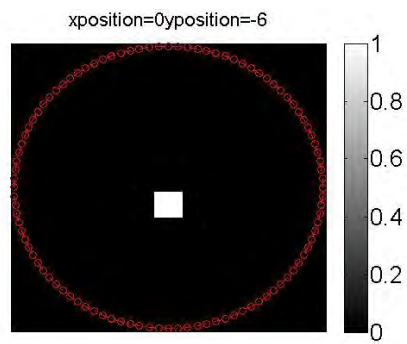
Figure 27. Phantom moved along negative y-axis while no change in x-axis
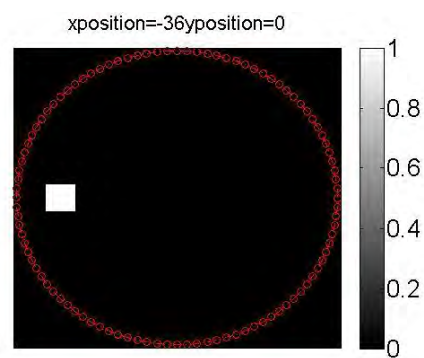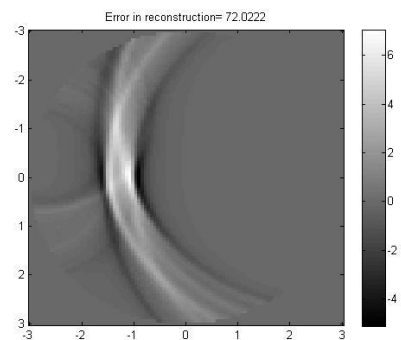
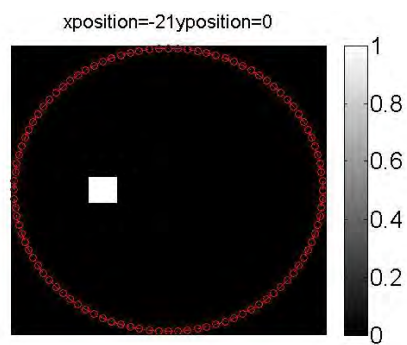**Figure 28. Corresponding reconstructions**

xposition=3yposition=-3

xposition=6yposition=-6

xposition=30yposition=-30

Error in reconstruction= 148.5313

Error in reconstruction= 126.3695

Error in reconstruction= 73.7465
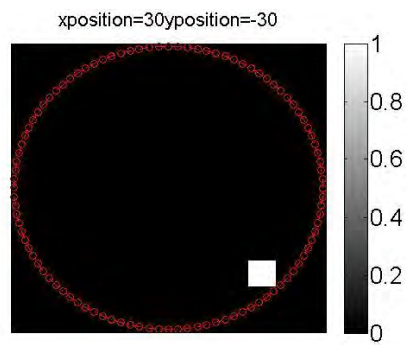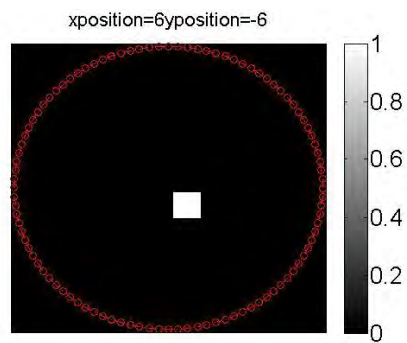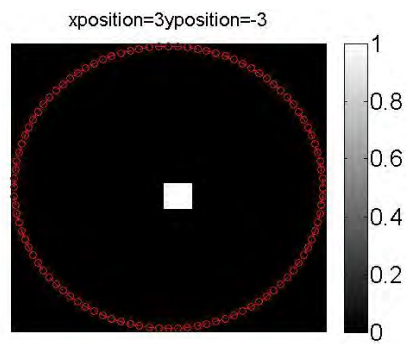
Figure 29. Phantom moved along the diagonal of the fourth quadrant of the Cartesian system
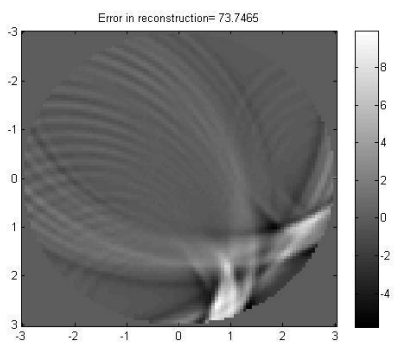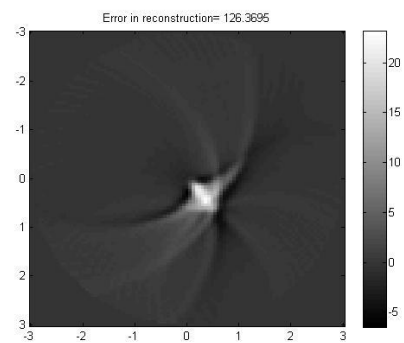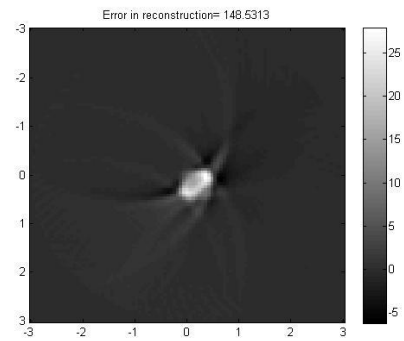
Figure 30. Corresponding reconstructions

53

The following phantom (figure 26) was used to find the effect of nearby objects to the original square in the binary phantom.
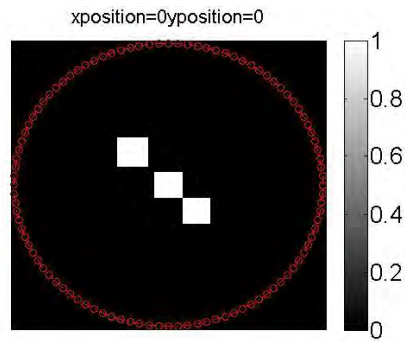
Figure 31. Objects placed next to the square in the original binary phantom
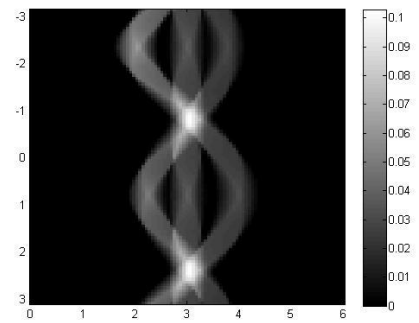
Figure 32. Corresponding sinogram

The reconstructed image is shown in Figure 33.
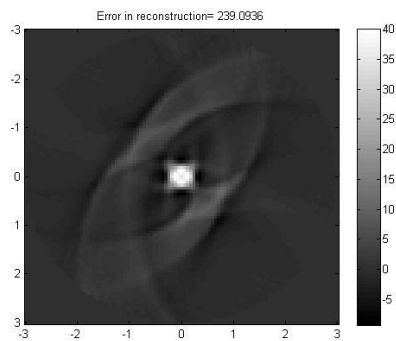
Figure 33. Reconstructed image of the phantom shown in Figure 31.

The following phantom (figure 34) was used to find the effect of the reconstruction algorithm on an asymmetrical object.
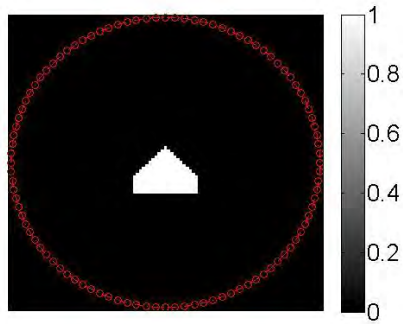
Figure 34. Objects placed next to the square in the original binary phantom
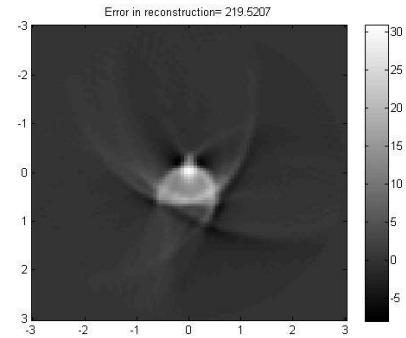
Figure 35. Reconstructed image of the phantom shown in Figure 34.

The following phantoms (figures 36 and 38) was used to find the effect of the reconstruction algorithm on the object by placing it in a random location at the top left quadrant of the Cartesian system.
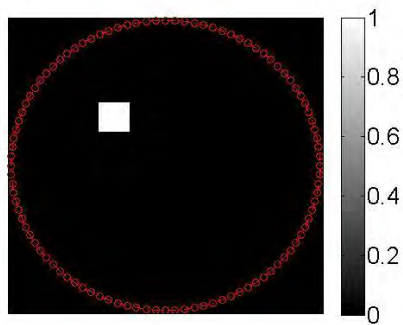
Figure 36. Objects placed in a random location on the top left quadrant
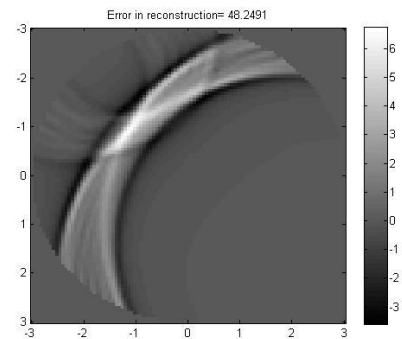
Figure 37. Reconstruction of Fig 36
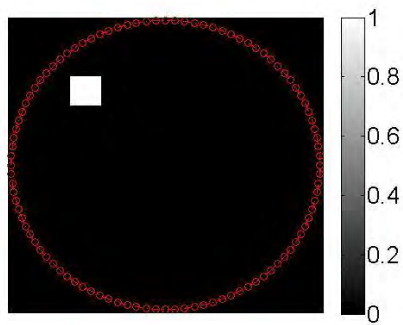
Figure 38. Objects placed in a random location on the top left quadrant
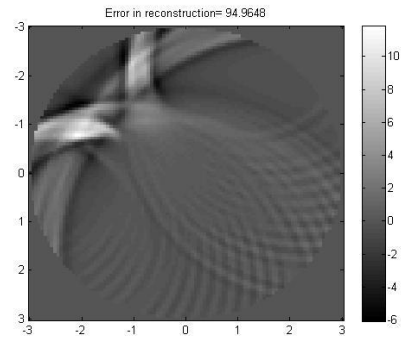
Figure 37. Reconstruction of Fig 38

The following graphs show the error in reconstruction as a function of position of the object along the x-axis, y-axis and the diagonal in the fourth quadrant of the Cartesian coordinate system.
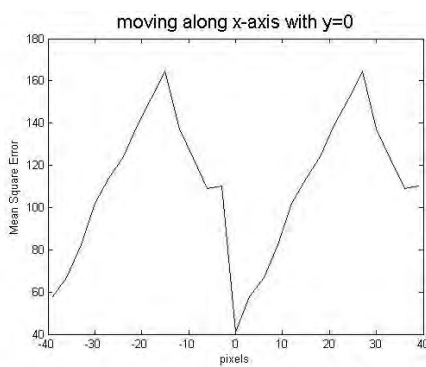
Figure 36. Error in reconstruction while phantom moved along x-axis while no change in y-axis
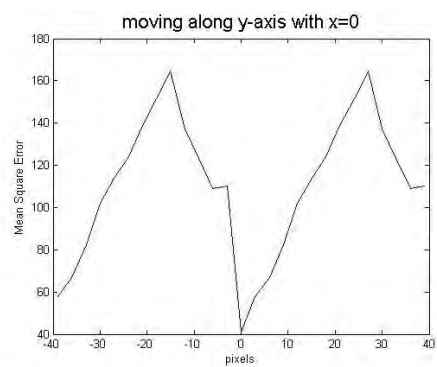
Figure 37. Error in reconstruction while phantom moved along y-axis while no change in x-axis
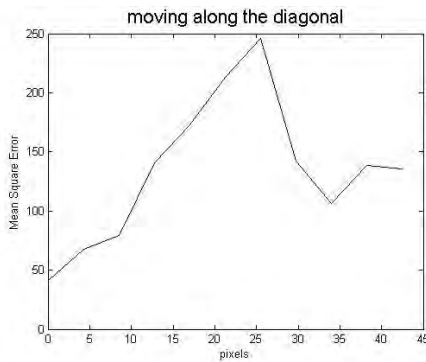
Figure 38. Error in reconstruction while phantom moved along the diagonal in the fourth quadrant of the Cartesian system

For the case of half-projections along the radial direction for all angles, the reconstruction fails to work. Figure 39, shows the sinogram for the Shepp-Logan phantom for all angles with half radial projections and Figure 40 shows the corresponding reconstruction.
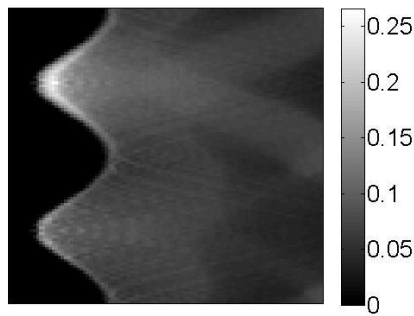
Figure 39. Sinogram for the Shepp Logan for half projections in the radial direction
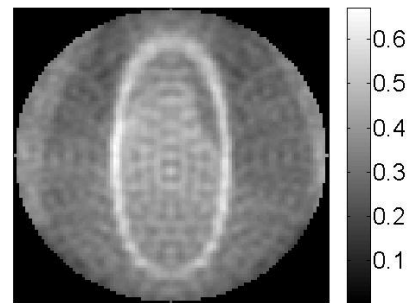
Figure 40. Recosntruction for the sinogram shown in Figure 39

57
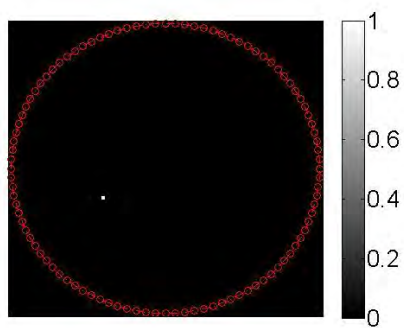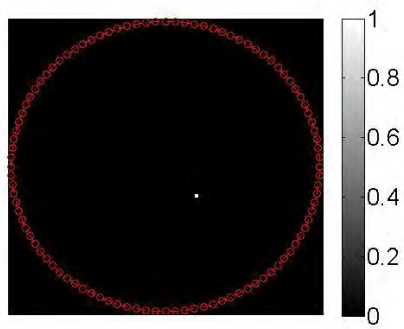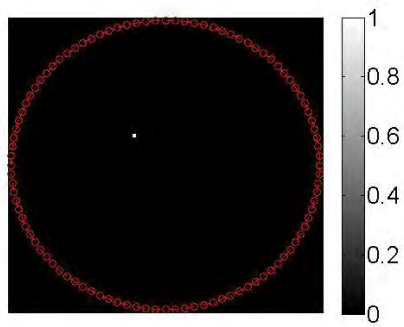
Figure 40. Moving point source around the origin
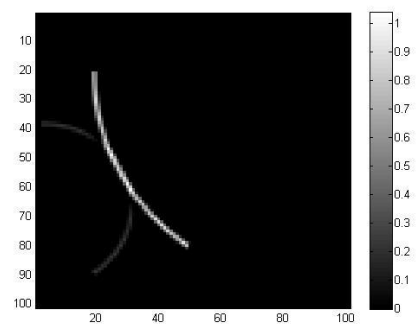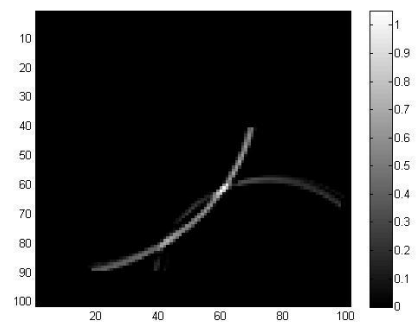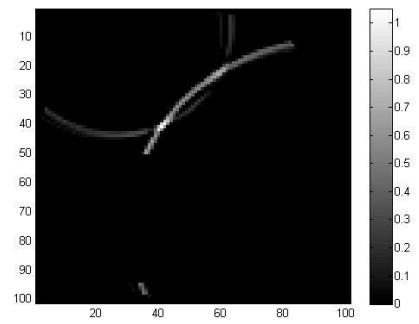
Figure 41. Corresponding reconstructions

Error in reconstruction= 87.991

Error in reconstruction= 77.0175

Error in reconstruction= 76.1921
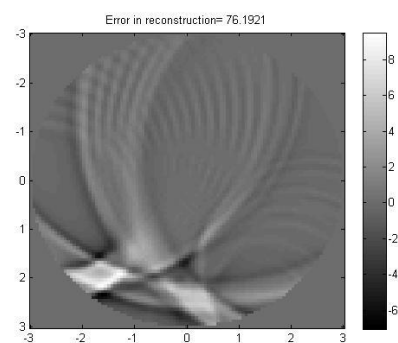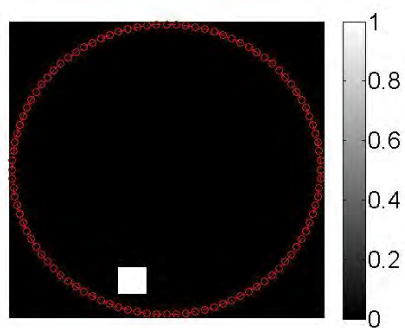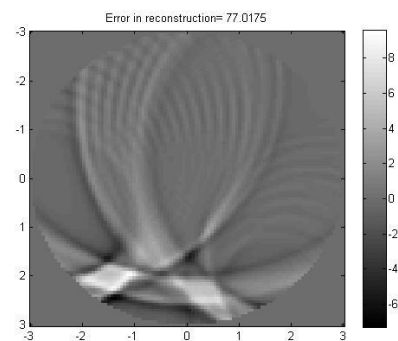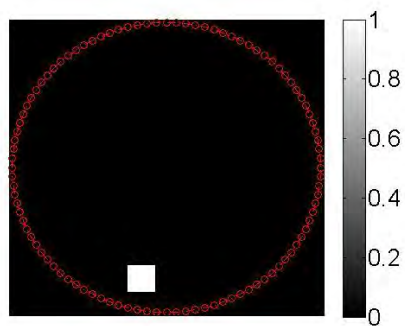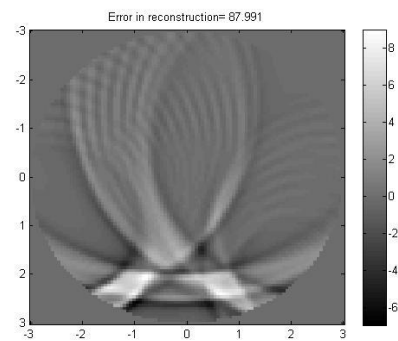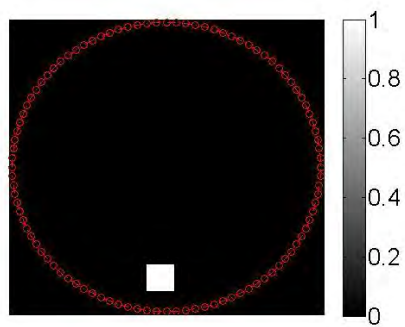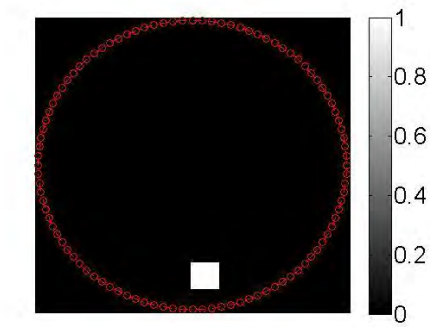
Figure 42. Moving the phantom to understand the symmetry in artifacts
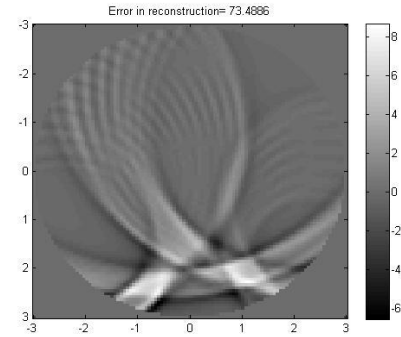
Figure 43. Corresponding reconstructions

In the case of bistatic imaging, where the radial factor in the original filter was replaced by minor axis of the ellipse over which the object is being integrated, it can be noticed that the reconstruction is favorable when the object is more towards the center of the ring of detector pairs. When the object is being displaced from the center, the reconstruction

worsens and only the artefacts are being reconstructed. This is evident from figures 26, 28 and 30.

When other squares are being added around the original object, the reconstruction still favors the square in the middle of the ring of detector pairs. The worsening of the artefacts spatially suggests that the filter (which is a log function of space) influences the reconstruction.

We can notice from figures 40 and 41 that the artefacts in the reconstruction of a point source placed at arbitrary locations around the origin splits asymmetrically which could be attributed the nonlinear nature of the filter and its effect on back smearing the obtained data.

To further understand the asymmetry, the binary square phantom was moved five pixels to left and right of the y-axis while keeping the center of the phantom around 35 pixels constantly below the x-axis. A slight flip shift in the intensities in the asymmetry could be observed between the reconstructions of the phantom on the extreme right and extreme left. A rotation of artefacts is observed while the phantom is moved from laft to right in a translational way..While the forward Radon is a linear operation, the backprojection filter does not have a linear property. And the approximation from the radial factor in the spherical Radon to the minor axis in the elliptical Radon worsens the artefacts. Though a reconstruction technique was attempted in Mensah[48], the work fails to analytically backup the reconstruction formula. The paper mentions classical Radon backprojection which cannot be applied to elliptical Radon because a Fourier slice

theorem does not exist for elliptical Radon transformed projections. Moreover, the reconstruction techniques mentioned in the paper fails to satisfy the special cases of ellipse namely, the line and the circle. When the two foci move away to infinity an ellipse become a line and the corresponding Radon becomes the classical Radon. But the parameterization of the lines in the classical Radon are in a different direction as compared to this special case of ellipse. A classical reconstruction would not work in this scenario. In the case when the two foci come together, the ellipse becomes a circle and the filter used in this paper does not match the analytically derived filter in Finch[47].

CHAPTER V

CONCLUSION AND FUTURE WORK

In the most common scenario Transrectal Ultrasound is performed using an endorectal probe containing linear arrays[50]. The primary contrast agent in the conventional imaging is the acoustic impedance mismatch. Acoustic impedance depends on the velocity and density and hence the tissue boundaries where these properties change will produce image contrast. Scatterers smaller than the wavelength can produce speckles in the ultrasound image.

Unfortunately, intracapsular prostate cancer is difficult to detect with standard 2D ultrasound. First, the prostate is a much more homogeneous tissue than the breast, and hence the contrast is limited. Furthermore, prostate cancer has a wide variation in appearance that overlaps with the appearance of other benign pathologies and hence conventional 2D ultrasound has not been shown to provide any additional sensitivity compared to digital rectal exam (DRE).

Since the progression of prostate cancer is an inherently 3D process, imaging the prostate in 3D may be useful for a radiologist. 3D TRUS is one way of imaging 3D prostate but still will suffer from contrast issues. Contrast-enhanced prostate Sonography using microbubbles has shown potential for prostate cancer detection and diagnosis[51].Although

the prostate is not as well-vascularized as the breast, there is sufficient capacity to even perform dynamic wash in/out studies using commercial microbubbles.

There also been some research work on translating transurethral ultrasound (TUUS) from therapeutic modality[52] to an imaging modality[53]. The image formation methods are different between TUUS and TRUS, novel methods can be invented combining these two.

In applications of breast imaging, photoacoustic and thermoacoustic tomography have been successful and powerful. Both these modalities merge a non-ionizing, high contrast/poor-resolution with low contrast/high resolution ultrasound to produce high quality images. However, there are technical obstacles in implementing these techniques in 3-D

In the pulse-echo method the axial resolution is inversely related to the ultrasound frequency For example to detect a 150μm sized breast microcalcification, frequencies greater than 10 MHz must be used. Higher the frequency, more they are attenuated in the body by tissues. In applications like breast imaging, reflection and transmission tomographic techniques are geometrically well-suited. Reflection tomography could be corrected for diffraction though it suffers the resolution limits like the pulse-echo methods. In transmission tomography, the Fourier diffraction tomography principle and related filtered backprojection image reconstruction algorithm can be used to produce good quantitative images of tissue attenuation and velocity[8].But they are not sensitive to hard scattering by some microcalifications Recent advances in inverse scattering

techniques are applied for breast imaging. Since the breast cannot be surrounded by detectors, as used in photoacoustic tomography, an additional angular coverage may be inherent to the collected acoustic data.

In time-domain ultrasound tomographic imaging, there exist several quantitative image reconstruction techniques. But there are limitations with FBP based techniques that reconstruct the object from integral transformed projections. One of the limitations is that all of the filtered back projection algorithms that currently exist work only if the compact of the image space is well-defined. This means that the image space is zero outside a fixed domain. This results in severe artefacts when we try and reconstruct objects that are placed exterior to the ring of detectors as shown in Figure 14. Even the reconstruction techniques suggested in[47] result in high smoothing of the object as is apparent from Figure 9 due to the log based radial filter. An additional limitation with the Radon transformed image reconstruction is that it works only when the medium is insonified by an impulse (which means infinite bandwidth). This might result in additional artefacts while reconstructing real data.

For the case of half-view data acquisition, that is, data obtained by detectors placed on a semi-circular arc around the object, the algorithm reconstructs surfaces that are touched tangentially by the circles over which they are integrated. This is evident from figure 15. It can be noticed that the sides of the squares disappear in the reconstruction. A mathematical discussion for this case can be found in[49].

As part of the future work, as a mathematical pursuit, an analytical formula to reconstruct elliptical Radon transformed data can be approached. In a special case of the elliptical Radon, a parabolic Radon can be obtained by moving one of the detectors to infinity, that is to say, keeping one of the foci of the ellipse constant and moving the other to infinity. An analytical formula for reconstruction for this case is currently not available in literature.

From an engineering perspective, reconstruction from limited number of angular projections can be approached. This will translate to lesser number of detectors in practice. Moreover, all the reconstruction algorithms assume that the speed of sound is constant. A more realistic model can be approached with varying speed of sound in an heterogeneous medium. With an integral type modeling, this will lead to a Radon transform in a different surface. It may be called the „noisy' Radon. An adaptive filter to backproject this kind of data can also be approached.

APPENDIX A

Matlab Code for forward and backprojection of Spherical Radon

```matlab
%Sradon.m need to be run with integrate1.m
%I would like to thank Marcus Haltmeier (email:
markus.haltmeier@uibk.ac.at) for sharing a partial pseudo-code and
%helping me understand the paper better

fun=phantom(101); %Insert your phantom here
radius=3;
diameter=2*radius;
angles=100;
radial=100;
sinogram=zeros(angles,radial+1);
angle_inc= 2*pi / angles;
radial_inc  = diameter/ radial;
object=linspace(-3,3,101);
object1 = linspace(-3,3,angles);
fil =linspace( 0,12,201);
fil=fil(:);
lfil=length(fil)-1;
dfil=fil(2)-fil(1);
pixel=object1(2)-object1(1)  ;
[X,Y]=meshgrid(object,object);
FINAL = zeros(101);
nfil=linspace(0,lfil-1,lfil)';
a=zeros(lfil+1,lfil);
b=zeros(lfil+1,lfil);


for i=1:lfil+1
    filtemp=fil(i) ;
    k =i-1;
    g1=-log(abs((nfil+1-k)./(nfil-k)));
    g1(i)=0;
    g2 =-filtemp*log(abs((nfil+1-k)./(nfil-k) ) );
    g2(i) = 0;
    if k>0
        g1(i-1) = 0;
        g2(i-1) = 0;
    end
    a(i,:)=g1(1:lfil);
    b(i,:)=g2(1:lfil)-fil(1:lfil).*g1(1:lfil);
end
```

```
object  = linspace( -3, 3, 101 );
ang = linspace( -pi, pi - 0.001, angles );
rad  = linspace( 0,diameter, radial+1);
xcirc = diameter/2 * cos(ang);
ycirc = diameter/2 * sin(ang);



for i=1:angles
center=[xcirc(i) ycirc(i)];
gram1 = integrate1( center,radius,fun,rad );
sinogram( i,: ) = gram1(1,:);
end

imagesc(sinogram);
radial1=radial-1;

for backp =1:angles
    cent   = [xcirc(backp); ycirc(backp)  ];
    mf(1,1:101 ) = sinogram(backp,1:101 )  ;

  mf(2:end-1)  = (mf(3:end) - mf(1:end-2))/(2*(radial_inc));
  mf = rad.*mf;
   if(backp==10)
        kk=mf;
    end
  m = [  -mf(end:-1:1) , mf(2:1:end) ];
  m = m(1:200)*a' +((m(2:201)-m(1:200) )/radial_inc)*b';
   mf(1,1:1:101) = m(1,101:1:201);
   dist=sqrt((X-cent(1)).^2+(Y-cent(2)).^2);

   fun1=interp1(rad,mf,dist) ;
  %
   FINAL=FINAL+fun1;
end
FINAL = (3*2*pi/100)*FINAL/(2*pi*3);
FINAL(not(FINAL<Inf))=0;
figure(2);
imagesc(FINAL);



%integrate1.m

function gram1 = integrate1(center,radius, fun,rad );

object = size(fun, 1 ) - 1;
xV = linspace(-radius,radius, object+1 );
```

```
mf = zeros( size(rad) );

hh = floor( 2 * object *  pi );

summe = 0;
for ir = 1:length(rad)
    r0 = rad( ir );

  beta= real( acos( r0 / (2*radius) ) ) ;
   calc  = atan2( center(2) , center(1) );
   hh2 = floor( hh * (beta/pi) * r0/(2*radius) ) + 1;
    angleV = linspace(calc+pi - beta, calc+pi + beta, hh2);
   s1 = center(1) + r0*cos( angleV );
   s2 = center(2) + r0*sin( angleV );

   fw  = interp2( xV, xV', fun, s1, s2 );
   fw( not(fw < Inf) ) = 0;
   summe = sum(fw(:));

   gram1(ir) = summe;
end
```

REFERENCES

1. Bjorn A.J. Angelsen, Ultrasound Imaging – waves, signals and signal processing, J. Acoust. Soc. Am, 121 (4), pp.1820-1820, 2007.
2. Frank Natterer, "An algorithm for 3D ultrasound tomography", Inverse problems of wave propagation and diffraction, pp.216-225, Springerlink, 2007.
3. S. J. Norton and M. Linzer, Ultrasonic reflectivity tomography: Reconstruction with circular transducer arrays, Ultrason. Imaging, 1, pp.154-184, 1979.
4. S.J.Norton and M.Linzer, Ultrasonic reflectivity imaging in three dimensions: Reconstruction with spherical transducer arrays, Ultrason. Imaging, 1, pp.210-231, 1979.
5. M.Kaveh, R.K.Mueller, and R.D.Iverson, Ultrasonic tomography based on perturbation solutions of the wave equation, Comput. Graphics and Image Processing,9,pp.105-116,1979
6. R.K. Mueller, M.Kaveh, and G.Wade, Reconstruction tomography and applications to ultrasonics, Proc. IEEE, 67, pp.567-587, 1979.
7. R.K.Mueller, M.Kaveh, and R.D.Iverson, A new approach to acoustic tomography using diffraction techniques, Acoustical holography, 8, A.Metherell, Ed. New York: Plenum, pp.615-628, 1980.
8. S.K.Lehman and S.J.Norton, Radial reflection diffraction tomography, J. Acoust. Soc. Am, 116(4), pp.2158-2172, 2004.
9. P.N.T.Wells, Biomedical Ultrasonics, Academic Press, 1977.
10. R.K.Mueller, M.Kaveh, and R.D.Iverson, A new approach to acoustic tomography using diffraction techniques, In: A. Metherall, Editor, Acoustical Imaging, Plenum Presspp.615-628, 1980.
11. E.Wolf, Three-dimensional structure determination of semitransparent objects from Holographic data, Optics Commun., pp.153-156, 1969.
12. J.F.Greenleaf *et al.,* Algebraic reconstruction of spatial distributions of acoustic velocities in tissue from their time-of-flight profiles, Acoustic Holography, 6, pp.71-90, 1975.
13. J.F.Greenleaf, S.A.Johnson,S.L.Lee,G.T.Herman, and E.H.Wood, Algebraic reconstruction of spatial distributions of acoustic absorption with tissues from their two-dimensional projections, Acoustical Holography, edited by P.S.Green(Plenum, New York),5,pp.591-603,1974.
14. R.K.Mueller, Diffraction Tomography I: The wave equation, Ultrason. Imag. , 2, pp.213-222, 1980.
15. E.Wolf, Three dimensional structure determination of semitransparent objects from holographic data, Opt. Commun.,1(4),pp.153-156,1969.

16. K.Iwata and R.Nagata, Calculation of refractive index distributions from interferograms using Born and Rytov's approximation, Jap. J. Appl. Phys, 14, pp.379-383, 1975.
17. J.M.Tribolet, A new phase unwrapping algorithm, IEEE Trans. Acoustics. Speech. Signal Proces. ASSP-25(2), pp.170-197, 1977.
18. S.A.Goss, R.L.Johnston, and F.Dunn, Comprehensive compilation of empirical ultrasonic properties of mammalian tissues, J. Acoust. Soc. Am., 64(2), pp.423-457, 1978.
19. S.A.Goss, R.L.Johnston and F.Dunn, Compilation of empirical ultrasonic properties of mammalian tissues. II, J. Acoust. Soc. Am., 68(1), pp.93-108, 1980.
20. S.J. Norton, Reconstruction of a reflectivity field from line over circular paths, J. Acoust. Soc. Am., 67(3), pp, 853-863, 1980.
21. S.J. Norton, Theory of acoustic imaging, Ph.D. thesis, Stanford University, Stanford Elect. Lab. Tech. Rept. No.4956-2, Chap. 5, 1976.
22. A. G. Bell, On the production and reproduction of sound by light, Am. J. Sci., 20, pp.305-324, 1880.
23. C. K. N. Patel and A. C. Tam, Pulsed optoacoustic spectroscopy of condensed matter, 53, pp.517-550, 1981.
24. M.Xu and L.V. Wang, Photoacoustic imaging in biomedicine, Rev. Sci. Inst.,77,pp.041101(1-22),2006.
25. G.Ku, X.wang, G.Stoica and L.-H.Wang, Multiple bandwidth photoacoustic tomography, Phys. Med. Biol., 49(7), pp.1329-1338, 2004.
26. F. A. Duck, Physical properties of tissue, Academic, London, 1990.
27. J.C. Lin, On microwave-induced hearing sensation, IRE. Trans. Microwave. Theory Tech., MTT-25, pp.605-613, 1977.
28. V.E. Gusev and A.A. Karabutov, Laser optoacoustics, American Institute of Physics, New York, 1993.
29. Photons plus ultrasound: Imaging and sensing 2005, edited by A.A Oraevsky and L.V.Wang (SPIE, Bellingham, WA, 2005), vol.5697.
30. Photons plus ultrasound: Imaging and sensing 2006, edited by A.A Oraevsky and L.V.Wang (SPIE, Bellingham, WA, 2006), vol.6086.
31. M. Haltmier, O. Scherzer, P. Burgholzer, and G. Paltauf, Thermoacoustic computed tomography using large planar receivers, 20(5), pp.1663-1674, 2004.
32. A. C. Tam, Applications of photoacoustic sensing techniques, 58(2), pp.381-431, 1986.
33. A.A. Oraevsky and A.A. Karabutov, in Biomedical Photonics Handbook, edited by T.Vo-Dinh (CRC, Boca Raton, FL), Chap. 34, 2003.
34. A. Macovski, Ultrasound imaging using arrays, Proc. IEEE, 67, pp.484-495, 1979.
35. F.Duck, S.Johnson, J.Greenleaf and W.Samayoa, Digital image focusing in the near field of a sampled acoustic aperture, Ultrasonics, 15, pp.83-88, 1977.

36. J.D.Coker and A.H. Tewfik, Multistatic SAR image reconstruction based on an elliptical geometry Radon transform, IEEE International conference on waveform diversity and design, pp.204-208, 2007.

37. Y. Xu, L.-H.Wang, G.Ambartsoumian and P.Kuchment, Reconstructions in limited-view thermoacoustic tomography, Med. Phys, 31, pp.724, 2004.

38. R. M. Arthur and S. R. Broadstone, Imaging via inversion of ellipsoidal projections of solutions to the linear acoustic wave equation, IEEE Trans. Med. Imag, 8(1), pp.89-95, 1989.

39. S. J. Norton, Reconstruction of a two-dimensional reflecting medium over a circular domain: Exact solution, J. Acoust. Soc. Am., 67(4), pp.1266-1273, 1980.

40. S.J.Norton and M.Linzer, Ultrasonic reflectivity imaging in three dimensions: Exact inverse scattering solutions for plane, cylindrical, and spherical apertures, IEEE Trans. Biomed. Engg., 28(2), pp.202-220,1981.

41. S.Aks and D.J.Vezzetti, Ultrasonic scattering theory I: Scattering by single objects, Ultrason. Imaging, 2, pp.85-101, 1980.

42. J.Ball, S.A.Johnson, and F.Stenger, Explicit inversion of the Helmholtz equation for ultrasound insonification and spherical detection, Acoustical Holography,8,A.Metherell, Ed. New York: Plenum, 1980.

43. G. Barton, Elements of Green's functions and propagation – Potentials, diffusion and waves, Oxford University Press, 1991.

44. S.Pourjavid and O. Tretiak, Ultrasound imaging through time-domain diffraction tomography, IEEE Trans. Ultrason. Ferroelectr. Freq. Control, 38, 74-85, 1991.

45. T. D. Mast, Wideband quantitative ultrasonic imaging by time-domain diffraction tomography, J. Acoust. Soc. Am., 106(6), pp.3061-3071, 1999.

46. J.M. Blackledge, R.E.Burge, K.I.Hopcraft and R.J.Wombell, Quantitative diffraction tomography: I. Pulsed acoustic fields, J. Phys. D., 20, pp.1-10, 1987.

47. D.Finch, M.Haltmeier and Rakesh, Inversion of spherical means and the wave equation in even dimensions, SIAM J. Appl. Math., 68(2), pp.392-412, 2007.

48. S.Mensah and E.Franceshini, Near-field ultrasound tomography, J. Acoust. Soc. Am., 121(3), pp.1423-1433, 2007.

49. P.Kutchment and L.Kunyansky, A survey in mathematics for industry: Mathematics of thermoacoustic tomography,Euro. Jnl. Of Appl. Mathematics,19, pp.191-224,2008.

50. ACR, ACR Practice guideline for the performance of ultrasound evaluation of the prostate (and surrounding structures), pp.1035-1038. ACR, 35 edition, 2006.

51. Ethan J Halpern, Contrast-enhanced ultrasound imaging of prostate cancer, Rev. Urol., 8(suppl 1): S29-S37, 2006.

52. C. Diedrich and E. C. Burdette, Transurethral ultrasound array for prostate thermal therapy: Initial studides. IEEE trans. On Ultrasonics, Ferroelectrics and frequency control, 43(6), pp.1011-1022, 1996.
53. J.O.Salo, T.Lehtonen and S.Rannikko, Prostate cancer protruding into the bladder imaged by transurethral and transrectal ultrasound, International journal on Nephrology, 19(2), pp.171-174, 1987.

6 Limited View Thermoacoustic Tomography

Yuan Xu
Ryerson University

Lihong V. Wang
Washington University in St. Louis

Gaik Ambartsoumian
University of Texas at Arlington

Peter Kuchment
Texas A&M University

CONTENTS

6.1 INTRODUCTION

Thermoacoustic tomography (TAT) employs the well-known [1–4] correlation between electromagnetic (EM) absorption of biological tissue and its physiological and pathological properties. To employ this contrast mechanism, a biological object is irradiated by a brief EM pulse, and the resulting thermoacoustic signals from the tissue are collected by ultrasound transducers to map the distribution of the radiation absorption within the sample (e.g., Refs. [5–9]). TAT thus combines the good spatial resolution of ultrasound imaging with the good contrast in EM absorption.

The problem we address in this chapter is of limited data (limited view), when transducers cannot be placed around the complete object. This situation is very common in TAT, for instance in its applications to breast imaging, where only a half sphere, rather than a sphere is available for placement. The question that arises is the theoretical and practical possibility of reconstruction from limited view data. Although, as we will see, mathematically rigorous uniqueness results exist that guarantee the theoretical possibility of reconstruction from limited view data, the practical situation is somewhat different. Namely, some features of the object

to be imaged (which we dub "invisible") are practically impossible to reconstruct, because they suffer from a mandatory blurring. Any attempts to overcome this difficulty are futile, unless some prior information about the object or missing data is incorporated, or the very physical set up of the measurement is altered. On the contrary, the "visible" details are easy to reconstruct stably. It is thus important to understand these limitations due to limited data. Limited view problems have been studied extensively in other, more traditional, types of tomography, such as x-ray, SPECT, diffraction tomography, and reflectivity tomography (e.g., Refs. [10,11,13–18]). The TAT situation is similar and has been discussed in various ways in Refs. [19–27]. Although the underlying mathematical technique is rather involved, the final results are easy to understand and use. The goal of this chapter is to review these results and to provide the relevant references. We will not attempt to go through the rigorous mathematical technicalities, but rather explain the basic ideas. Correspondingly, the results will sometimes be stated, when the authors feel no danger of misuse, without some necessary technical conditions under which they are proven. References, however, will be given where the rigorous details can be found.

A significant limitation of what is described in this chapter is that the speed of ultrasound in the imaged tissue is assumed to be constant. The case of a variable speed could also be treated, but this would require a somewhat different and more complex consideration, which apparently has never been completely implemented.

The paper is structured as follows: In the next section, we state the model and briefly review the existing uniqueness results, reconstruction formulas, and procedures for the full data view problem. The section that follows contains the description of how the limits of view influence the uniqueness and reconstructions. It is explained how one can determine which interfaces in the object will be blurred in the reconstructed image due to the limited view. We also introduce in this section necessary simple mathematical notions. Then the next section presents numerical examples (both from synthetic and experimental data) that illustrate the concepts. All mathematical conclusions are equally applicable to photoacoustic tomography.

6.2 MATHEMATICAL MODEL AND RECONSTRUCTION IN TAT

The accepted mathematical model of TAT involves quite a few physical constants. As it happens, their presence is irrelevant for understanding the concepts and using the limited view results. We thus present here a simplified model, where all constants are assumed to be equal to one. The full-blown models with all the complications (which do not influence the issue we discuss here), as well as more details and references, can be found in surveys [28–30] and in chapters [31,32] in this volume.

With this simplification, the model of TAT is described by the following wave equation problem:

$$\begin{cases} p_{tt} = v_s^2(x)\Delta_x p,\ t \geq 0,\ x \in \mathbb{R}^3 \\ p(x,0) = f(x), \\ p_t(x,0) = 0, \\ p(y,t) = g(y,t)\ \text{ for }\ y \in S,\ t \geq 0. \end{cases} \quad (6.1)$$

Here $p(x,t)$ is the pressure at the point x and time t, $v_s(x)$ is the speed of the ultrasound propagation in the tissue, S is the observation surface where the transducers are placed, $g(y,t)$ is the measured data, i.e., the value of the pressure at time t measured at the transducer's location $y \in S$, and $f(x)$ is the object to be reconstructed. As we have already mentioned, the results described here apply to the case of a constant sound speed only. We can also assume that $v_s = 1$, thus arriving at the simpler equations

$$\begin{cases} p_{tt} = \Delta_x p,\ t \geq 0,\ x \in \mathbb{R}^3 \\ p(x,0) = f(x), \\ p_t(x,0) = 0, \\ p(y,t) = g(y,t)\ \text{ for }\ y \in S,\ t \geq 0. \end{cases} \quad (6.2)$$

In this (constant speed) case, the well-known Kirchhoff–Poisson formulas (see, e.g., Refs. [33,34]) allow one to represent the solution $p(x,t)$ in terms of the spherical means of the function $f(x)$

$$(Rf)(y,t) := \frac{1}{4\pi}\int_{|\omega|=1} f(y+t\omega)d\omega \quad \text{for } y \in S. \quad (6.3)$$

Thus, knowledge of the data $g(y,t)$ is equivalent to knowing the integrals of the unknown function f over all spheres centered at transducers' locations $y \in S$. One immediately notices a similarity with the standard Radon transforms for x-ray tomography or MRI, where the integration is done over lines or planes rather than spheres. And indeed, most of the standard tomographic results and techniques find their analogs in TAT, albeit many aspects become much more involved (see, e.g., Refs. [28–32,35–43]). We now address the uniqueness of reconstruction and reconstruction procedures in TAT.

The reader can notice that in all feasible applications, function $f(x)$ to be reconstructed does not have "infinite tails", i.e., vanishes outside of a bounded domain. Moreover, in most practical applications, it is true that its support is completely surrounded by the observation surface S. In what follows, this will be assumed (some results and inversion formulas might fail unless this is satisfied [30,31]).

We first assume the knowledge of the full data $g(y,t)$ for an observation surface S, which is a sphere surrounding the support of the image $f(x)$. The case of limited-angle data will be considered in the next section.

A similar problem to the one we have just described in 3D can also be considered in other dimensions. For TAT, only dimensions 2 and 3 are relevant (the need to use a 2D problem arises, for instance, when one uses linear, rather than point-like, detectors [24,25]).

6.2.1 UNIQUENESS OF RECONSTRUCTION

The first question to answer is whether the data determines function f uniquely, i.e., which observation surfaces S provide uniqueness of reconstruction. In 2D, this was resolved in Ref. [35]. There is still no complete solution in 3D (see Refs. [15,28–32,35,38–41] for surveys and references). However, from the practical point of view, there is no problem. Indeed, it has been known at least since Ref. [44] (see also the references just mentioned and Ref. [45]) that if the surface S is closed, e.g., a sphere, and if f has a bounded support (not necessarily surrounded by S), then there is uniqueness.* When S is a cylinder, uniqueness also holds, and if S is a plane, uniqueness holds if f vanishes on one side of the plane (otherwise an odd function f with respect to the plane provides a counterexample). This essentially covers any feasible full-view TAT situation.

Now, when uniqueness is established, one wonders how to actually reconstruct the image f.

6.2.2 RECONSTRUCTION FORMULAS AND ALGORITHMS

Although the area had experienced a slow start, there has been a large variety of inversion formulas and algorithms developed lately (at least for the case of a constant sound speed that we consider here). One can find a thorough discussion of inversion formulas and reconstruction algorithms in the surveys [31,32] in this volume, as well as in Refs. [29–32]. We will just say a few general words about these, since the details of a particular algorithm do not seem to affect the general conclusion that we will make later about the limited view problems in TAT.

Explicit inversions based on Fourier transform techniques have been developed in the case of a planar observation surface S (see, e.g., Refs. [16,46–50]).

The most interesting case of a spherical surface S was first rigorously treated in Refs. [51,52], where the rotational invariance of the problem was used to expand the data and the image into Fourier series with respect to the angle. This resulted in explicitly solvable Abel-type integral equations for each Fourier coefficient (a la A. Cormack's work on x-ray CT). While the 2D formulas of Ref. [51] involved numerical instabilities, this was fixed in the 3D reconstructions of Ref. [52].

For quite some time, there had been no explicit filtered backprojection-type formula obtained for any closed observation surface S, and even the possibility of such a formula was questioned. Finally, in Ref. [38], such formulas were found for all odd dimensions when S is a sphere, and then extended to even dimensions in Ref. [53]. A different 3D backprojection-type formula was obtained in Ref. [54]. A backprojection formula for arbitrary dimension was found in Ref. [55], which in 3D coincided with the one in Ref. [54]. It is interesting to note that the series of formulas in Refs. [38,53]

and in Refs. [54,55] are not equivalent on nonperfect data, albeit they seem to work numerically equally well [30,31]. A different derivation of formulas in Ref. [38] has recently been proposed [56]. No closed form analytic formulas are known for surfaces S that are not spheres, cylinders, or planes.

An interesting series expansion inversion procedure that theoretically works for any closed observation surface S was suggested in Ref. [57]. The expansion of the image $f(x)$ into the eigenfunctions of the Laplace operator Δ inside S with zero Dirichlet conditions on S is obtained in terms of the corresponding expansion of the measured data. It was shown in Ref. [57] that a cubic surface used as S rather than a sphere works much better, leading to very fast, accurate, and efficient reconstructions. This series expansion procedure was generalized to variable sound speeds in Ref. [43], albeit it is doubtful that this can lead to efficient computations.

Although having analytic inversion formulas always helps in tomography, it is also known that reconstructions can often be efficiently done without having explicit formulas, by either algebraic techniques, or their combination with analytic preconditioning. This is true in TAT as well. Namely, it is not hard to write a good approximate inversion operator (technically called a **parametrics**) that gives a sufficiently good approximate reconstruction and preserves the locations and strengths of all singularities of f (e.g., sharp boundaries). Then one can bootstrap the quality of reconstruction by a standard iterative numerical procedure (e.g., Refs. [23,58,59]).

Another option is the so-called time reversal. Here one solves the wave equation backward in time, starting with a sufficiently large time, when the signal essentially disappears. Then when time $t=0$ is reached, the image $f(x)$ is recovered (e.g., Refs. [36–38,43,60,61] and references therein).

Various other discussions of inversion procedures and relevant references can be found in Refs. [29–31,36,37,62–71].

6.3 LIMITED VIEW PROBLEM

We now switch to the situation of our main interest in this paper—limited view TAT. Suppose that S is a sphere (or some other closed surface) surrounding the image f, and the only possible locations of transducers belong to a 2D piece Γ of S. In this case, we only have the data $g(y,t)$ collected at the locations y in Γ, rather than from the whole sphere. In this case, we face a limited angle (limited view) problem.

6.3.1 UNIQUENESS OF RECONSTRUCTION FROM LIMITED VIEW DATA

Let us first discuss the uniqueness of recovering the image from the data. The dimension count shows that one should use a two-dimensional piece Γ of S in order to expect uniqueness. Suppose that S is an analytic surface (say, a sphere) and Γ its two-dimensional piece. It follows from the results of Ref. [35] that if uniqueness of recovery from the data collected on the whole S is known, then there is also uniqueness of recovery with data collected on Γ. For instance, since the sphere is

---

* For the uniqueness result to hold, it is not necessary to require that f vanishes at infinity, sufficiently fast decay at infinity also suffices [45]. However, in practical situations, f does vanish at large distances.

analytic and since for the whole sphere uniqueness of reconstruction is known (see the preceding section), we conclude that with the data on any full-dimensional piece Γ of the sphere, no matter how tiny, solution of the TAT problem is unique. The same holds for a 2D piece of any closed analytic surface.[†]

Although this says that the limited view data is theoretically sufficient, anyone trying to do reconstructions faces problems, mostly related to blurring of some parts of the image. This effect is no accident and can be predicted, as explained in the rest of the chapter. Let us look first at how one can try to reconstruct the image from limited view data.

6.3.2 Limited View Reconstructions

The simplest thing one can try is just to replace the missing data with zero values[‡] (the procedure often called zero-filling or zero-padding) and then reconstruct the image as if the data were complete. In advance, one might not expect any reasonable outcome from this, however the following observations appear, independently of the exact procedure involved:

1. Some (we will call them "**visible**"[§]) parts of the tissue interfaces and other singularities contained in the true image are seen clearly and at the right locations. These parts do not depend upon the exact technique used, but do depend on the view angle available.
2. Other parts of interfaces blur away.
3. "Smooth" details of the object, i.e., exact values of $f(x)$ get distorted, in some areas significantly.

In most cases in tomography, limited data problems allow no exact reconstruction formulas. In the rare cases when these do exist, this does not change the effects listed above. As we explain below, there is a good reason for this, and, in fact, the "invisible" and "visible" parts of singularities can be easily predicted by a simple geometric consideration. In order to do so, we need to introduce some technical notions from the so-called microlocal analysis first (see, e.g., Ref. [72] for simple introduction and Refs. [15,18,23,35,39,73,74] for applications in integral geometry and tomography).

6.3.3 Wavefront Sets of Functions

Our goal is to apply known results of integral geometry concerning singularity reconstruction [11,12,15,39] to TAT [19,23]. The exact description of these would require some notions of microlocal analysis, in particular the notion of a wavefront set of a function [72]. In tomographic problems, in particular in TAT, one is most interested in only one type

of singularity: the jump of $f(x)$ across an interface (a curve in 2D or a surface in 3D). So, we will describe the wavefront set in this case first. Let $f(x)$ be smooth except for a jump across a smooth surface L (in 2D case, L is a curve), then the wavefront set WF(f) of $f(x)$ consists of pairs (x,ξ), where point x belongs to L and $\xi \neq 0$ is a nonzero vector normal to L at x, as shown in Figure 6.1.

Before introducing the wavefront set in the general case, let us recall that smoothness is reflected as decay in the Fourier domain. Indeed, if $f(x)$ is smooth and has compact support (or decays sufficiently fast with its derivatives), then its Fourier transform $\hat{f}(\xi)$ decays faster than any power of $|\xi|$ in all directions of the ξ-space. If we are interested in detecting the smoothness of f only locally, near a point x_0, we cut other parts off by multiplying f by a smooth function ϕ that is nonzero only near x_0. Then, again, the Fourier transform $\widehat{\phi f}(\xi)$ of the product decays faster than any power of $|\xi|$ in all directions of the ξ-space. Well, what does it mean now that f is **not smooth** near x_0? This means that $\widehat{\phi f}(\xi)$ will not be decaying, unless ϕ vanishes at x_0, which we will prohibit. However, it might still decay **in some directions**. This now leads to the general definition (e.g., Refs. [39,72]) of the wavefront set, which picks up for each point x_0 the bad directions ξ_0 only. It thus consists of pairs (x,ξ_0), where ξ_0 must be a nonzero vector (in order to determine a direction). It is easier to describe which pairs (x_0,ξ_0) (where $\xi_0 \neq 0$) **do not** belong to the wavefront set WF(f) of a function f. Namely, this happens if there is a neighborhood u of x_0 and a conic neighborhood

$$V_\epsilon = \left\{ \xi \neq 0, \quad \text{such that} \quad \left| \frac{\xi}{|\xi|} - \frac{\xi_0}{|\xi_0|} \right| < \epsilon \right\}$$

of the direction ξ_0, such that for any smooth function ϕ supported inside u, the Fourier transform $\widehat{\phi f}(\xi)$ of the function ϕf decays to zero faster than any power of $|\xi|$ when $\xi \to \infty$ in V_ϵ. The role of the function ϕ is to eliminate the possible bad behavior of f away from x_0 and keep only the local
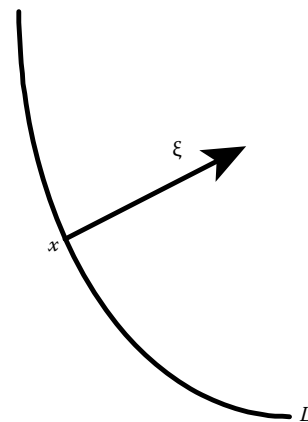
FIGURE 6.1   If $f(x)$ is smooth, except a jump singularity across L, then its wavefront set WF(f) consists of pairs (x,ξ), where x belongs to the jump interface L, and ξ is a nonzero vector normal to L, at x. (Reproduced from Xu, Y., L.V. Wang, G. Ambartsoumian, and P. Kuchment, *Med. Phys.* 31(4):724–33, 2005. With permission.)

[†] A similar result holds also in x-ray CT, where limited view data uniquely determine the image. This immediately follows from the projection-slice theorem and analyticity of the Fourier transform of a compactly supported function.

[‡] It is advisable sometimes to smooth out the jump between zeros and actual data.

[§] Another name sometimes used is "audible" [39].

information about properties of f at x_0. Thus, the wavefront set of f carries the information about singularities of f, which is localized both in spatial variable x and frequency variable ξ (the word used is "microlocalization", and thus "microlocal analysis"). Projecting the wavefront set onto the space component x (by forgetting the frequency variable ξ), one obtains the so-called singular support of f, i.e., the set of all singularities of f—points near which f is not smooth. For instance, it is easy to check that the wavefront set of the delta function consists of $(0, \xi)$ for any $\xi \neq 0$.

6.3.4 "Visible" Singularities and Their Reconstruction

The general idea of the microlocal approach to limited view problems is the following [11] (see a somewhat different, more limited approach in Ref. [12]). One tries to determine which wavefront set elements (x, ξ) of the object f lead to singularities, i.e., wavefront set elements in the measured data g. This can be done by the technique of the so-called Fourier integral operators (FIOs) [73,74], which is beyond the scope of the current consideration. If such a pair (x, ξ) does lead to a singularity in g, it is called "**visible**" or "**audible**". Such wavefront set points of the object can be stably reconstructed from the data g, and thus the singularity will show up in the reconstruction. If a particular wavefront set point does not influence the singularities of the data g (i.e., it is smoothed out), it becomes "invisible" and thus will be blurred away. This blurring effect is intrinsic to the problem and cannot be overcome by changing analytic or numerical techniques, unless some extra information is incorporated into the problem.

This concept is not hard to understand. Imagine, for instance, that the operator that maps the unknown f into the data set g, turns all images even the ones with singularities, into smooth functions g. In the Fourier domain, this can be interpreted as an operation that turns slowly decaying Fourier transforms into the ones that decay faster than any power. For instance, one can imagine that this is done by applying a filter that decays extremely fast, and essentially acts as a low-pass filter. Trying to invert the procedure and reconstruct the object f from the data g, one runs into trouble, since the required filters will grow faster than any power (often exponentially). This clearly indicates impossibility of stable reconstruction of high-frequency components, and thus of any sharp details.¶ A "microlocal" extension of this consideration shows that if some part of the wavefront set (i.e., a singularity) of the image f does not contribute to the wavefront set of the data, then this singularity cannot be stably recovered from the data.

It is thus important to be able to understand in advance which wavefront set elements (x, ξ) of the (unknown) f would lead to some wavefront set elements in g. This would determine which singularities are "visible" from the data g.

Fortunately, there is a very simple answer to this question in the cases of x-ray tomography, SPECT, TAT, and some other imaging methods [11,15,18,19,39] (while its justification is very nontrivial). We will describe it following Ref. [19] (see also Ref. [23]), as applied to TAT:

The "visibility" condition

An element (x, ξ) of the wavefront set of f cannot be recovered looking at the singularities of the spherical integrals data, unless there is a detector location and a sphere centered at this location that passes through the point x and is normal to ξ at this point. In other words, in TAT one can see without blurring only those parts of the interfaces that can be touched tangentially by spheres centered at detector positions. This means that in order to recover stably (i.e., without blurring) the interface L, one needs to have for each point of L a detector located along the normal line to L at this point. If for some part of L, the normals do not pass through the detectors, this part will be "invisible" and will be mandatorily blurred away.

Remark 1 *This principle does not depend upon a particular reconstruction method. So, a bad method can increase blurring, but even the best methods cannot recover sharply the "invisible" interfaces. This is why in this text we do not go into any details of reconstructions. Certainly, incorporation of additional a priori information about the image (e.g., that it consists of a few simple "blocks") could potentially lead to improvements.*

The visibility condition described above is not hard to understand. Indeed, assume for simplicity that the integration that produces the measured data is done along planes rather than spheres, and that the interface is also planar. Then, if one integrates along a stack of parallel planes $x \cdot \omega = s$ that is not parallel to the interface L (i.e., the normal vector ω to the plane of integration is not normal to L), the singularity of f along the interface is smoothed out, and the resulting value depends on s smoothly. Only if one has at one's disposal a set of planes parallel to the interface (i.e., ω is normal to L), then the integration of f will result in a singularity with respect to s. This indicates that invisible parts of the wavefront set do not show up as singularities in the measured data, and thus cannot be stably reconstructed. This hand-waving explanation can be made precise, with substantial technical effort.

Notice that if at some location x, any line passing through x crosses a detector position, then for any image, we expect its details near x to be reconstructed sharply. This leads us to the following notion:

Definition 2 *Suppose that detectors can be located along a 2D (1D in the planar case) piece Γ of the observation surface S only. The **detectable region** consists of such points x inside S that every line passing through x crosses Γ.*

According to the visibility condition, any object supported inside the detectable region will be sharply reconstructed, while the objects reaching outside the detectable region will have some parts of their interfaces blurred away.

¶ One faces such instabilities, for instance, trying to solve the heat equation back in time, or dealing with electrical impedance imaging or optical tomography.
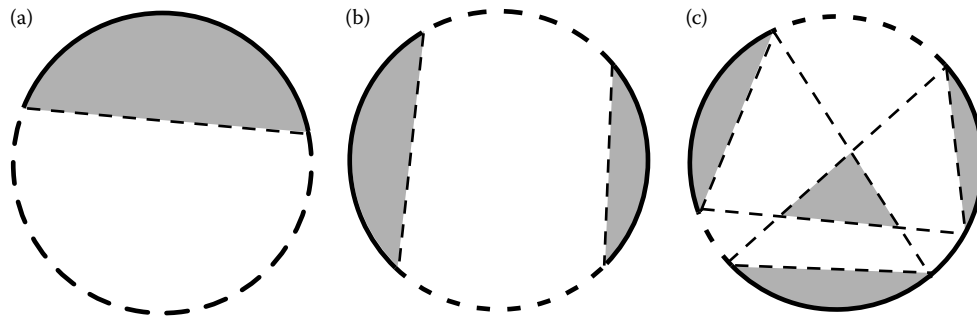
FIGURE 6.2 (a) Illustration of the "detectable regions" (shaded areas) of circular Radon transformation, when the detector moves along a single arc (solid) of a circle. (b) Two arcs. (c) Three arcs. (Reproduced from Xu, Y., L.V. Wang, G. Ambartsoumian, and P. Kuchment, *Med. Phys.* 31(4):724–33, 2005. With permission.)
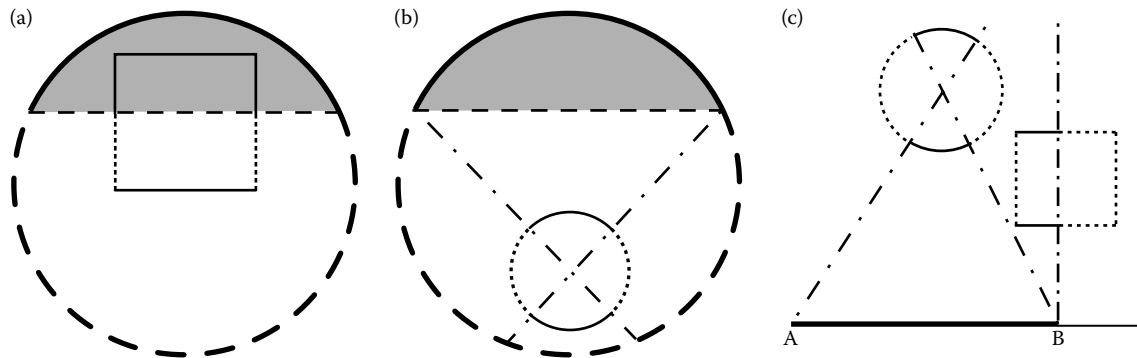
FIGURE 6.3 (a) "Visible" (solid line) and "invisible" (dashed) boundaries of a square object, and the "detectable regions" (shaded areas) when the detector moves along an arc (solid). (b) Same as (a) for a disk phantom. (c) Same as (a) except that the detector moves along the line segment AB and the objects are a square and a disk. The "visible" boundaries are expected to be recoverable stably, while the "invisible" boundaries should be blurred away. (Reproduced from Xu, Y., L.V. Wang, G. Ambartsoumian, and P. Kuchment, *Med. Phys.* 31(4):724–33, 2005. With permission.)

Figure 6.2 illustrates the detectable regions. Figure 6.3 shows the expected behavior of the reconstructed interfaces of simple square and disk phantoms with limited view data.

Results of reconstructions from synthetic and experimental data, which confirm this conclusion, are shown in Section 6.4.

6.3.5 HALF-SPHERE PROBLEM

A particular case of interest, which has attracted the attention of several researchers, is when the detectors can be placed along half of the observation sphere *S*, and thus the detection region is the corresponding half-ball. It is assumed that the object is located inside the detection region. Then, the principle discussed in the previous section predicts that all singularities of the object are "visible" and thus reconstructions should be sharp. If one attempts to zero-fill the data from the other half sphere and use any of the standard reconstruction methods, the interfaces truly remain sharp, but the intensities deteriorate towards the missing equator. Having an exact reconstruction formula for half-sphere data would fix this problem, but such a formula has not been found so far.** So, different partial remedies for this ailment have been sug-

gested: better approximate inverses, corrective coefficients, numerical minimization, using range conditions for recovering the missing data, etc. (e.g., Refs. [22,26,27]). A very recent work [77] shows great promise for the final resolution, albeit at the moment of writing this chapter, not all necessary details have been filled in.

6.3.6 LOCAL TOMOGRAPHY AND SINGULARITY SHARPENING

We would like to mention briefly the principle of the so-called **local tomography** [18,78–80]. In this method, before backprojection, an additional growing filter in the frequency domain is applied in order to sharpen singularities. The resulting reconstruction has incorrect numerical values of *f(x)*, but significantly emphasized interfaces and other singularities, which, for instance, can be useful when small blood vessels or region of interest tomography are of interest. Local tomography applies to TAT as well [19,23]. In the case of limited view data, it also recovers the "visible" parts of the interfaces only. Some of the reconstructions shown in the next section include their local tomography counterparts.

It is interesting to notice (see more about this in the following section), that transducers' responses often act as that extra filter needed for local tomography, and thus boundaries are emphasized without any extra effort.

** In SPECT, a similar problem waited quite a long time before its satisfactory resolution [75,76].

6.4 NUMERICAL AND EXPERIMENTAL VERIFICATION

In this section, we will illustrate our theoretical analysis and conclusions with reconstructions [23] from both synthetic and experimental (i.e., collected from a physical phantom) TAT data. We do not mention details of specific reconstruction methods used because, as explained earlier, the "visibility–invisibility" effect does not depend on the method used.

6.4.1 RECONSTRUCTION FROM SYNTHETIC LIMITED VIEW THERMOACOUSTIC TOMOGRAPHY DATA

A numerical phantom that contains four sharp and one soft inclusion is shown in Figure 6.4. Among the sharp inclusions, we have one large and two small squares and one disk. The object value is set to be 0.5 within the largest square, unity within other sharp inclusions, and zero elsewhere. Inside the "soft" circular inclusion, this value drops linearly with the radius from unity at the center to zero at the interface, in order to simulate a gradual interface. The imaged field of 154 mm by 154 mm is mapped with a 128×128 mesh. The detection circle has a radius of 133 mm and is centered at the center of the picture. We scan 200 steps in all the simulations. The gray scale and the scale bar of the images are shown below the images in Figure 6.5. The top row of reconstructions employs the local tomography formula that emphasizes the boundaries. The next one uses the approximate filtered-backprojection (FBP) formula in Ref. [23], and the lowest one shows the improvements
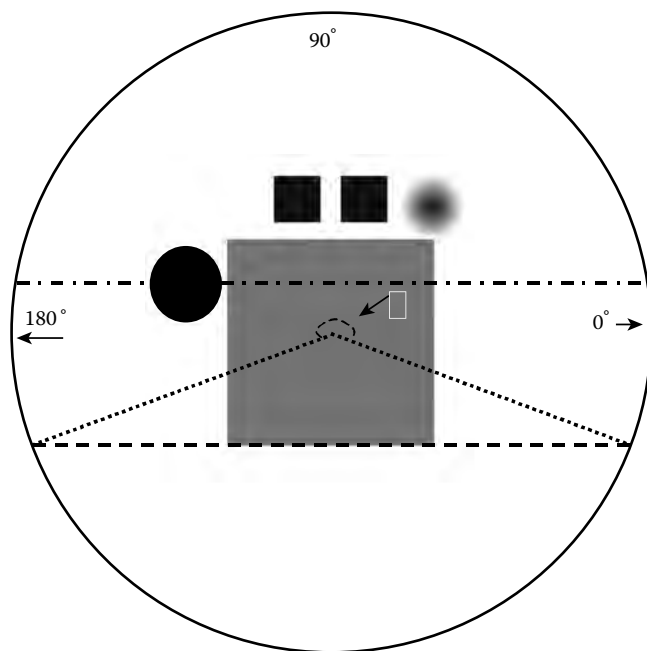
achieved by running the algebraic reconstruction method (TCG), starting with the FBP as an initial guess [23].

The left column uses only the data collected from the $\pi/2$ detection arc in the first quadrant. None of the phantom inclusions fit into the "detectable region". One can see that all parts of the inclusion boundaries the normals to which do not intersect the detection arc are blurred (even in the local tomography reconstruction). Other parts of the boundaries are sharp. This is in perfect agreement with our theoretical prediction. The soft inclusion is not significantly affected by the artifacts.

The middle column employs the data collected from the detection arc of approximately 217 degrees (the angle θ in Figure 6.4), whose chord coincides with the bottom side of the large square inclusion. In this case, all inclusions are in the "detectable region", and hence all the boundaries are reconstructed sharply. The third column represents the full data reconstruction. Notice that the quality of the final reconstructions in the last two columns is the same. Figure 6.6a and b show the reconstructed image $f(x)$ along the dashed-dotted line in Figure 6.4, using the FBP (Figures 6.5d through f) and TCG reconstructions (Figure 6.5g through i), respectively. The exact value is also shown for comparison. It can be found in Figure 6.6a that the results of FBP are in good agreement with the real value for the case of 217-degree and 360-degree detection, where all objects are in the "detectable region". Iteration improves the results further, as shown in Figure 6.6b. Even for the case of a 90-degree detection curve, the profile of the objects is reconstructed. Comparing Figure 6.6a and b, one finds that the significant overshoot and undershoot in FBP can be considerably reduced by TCG iterations (we remind the reader that FBP is only an approximation rather than the implementation of an exact formula).

Figure 6.7 shows the relative error of each reconstruction as a function of the scanned angular range with respect to the center of the scan. We study the mean reconstruction values in the hard sphere, the central square, and the background. The errors of reconstruction are normalized to the corresponding real values in the cases of the hard sphere and the central square, and to the real value of the hard sphere in the case of the background (because its real value is zero). When the scanned angular range is less than π, the errors decrease sharply with increasing scanned angular range. By contrast, when the scanned angular range is larger than π, the errors change much more slowly as the scanned angular range increases. The results agree with our theoretical conclusions. However, there are some fluctuations added to the trends of the curves. By comparing the three curves in Figure 6.7, we find that these fluctuations depend strongly on the location of the object with respect to the detection curve. More extensive study is needed to understand these fluctuations. There are some residual errors even in the full-view detection in Figure 6.7. This is because we used an approximate backprojection algorithm, rather than an exact inversion (which was not available at that time).

FIGURE 6.4 Diagram of inclusions in TAT (used in Figure 6.5). The value of the image $f(x)$ is set to be 0.5 in the largest square, and unity within other sharp inclusions, and zero elsewhere. Inside the "soft" circular inclusion, this value drops linearly with the radius from unity at the center to zero at the interface. (Reproduced from Xu, Y., L.V. Wang, G. Ambartsoumian, and P. Kuchment, *Med. Phys.* 31(4):724–33, 2005. With permission.)

FIGURE 6.5 Images reconstructed from simulated TAT data corresponding to the phantom in Figure 6.4. The three columns correspond from left to right to detection angles of 90 degrees (from 0º to 90º), 217 degrees (from –19º to 198º as shown by the angle θ in Figure 6.4), and 360 degrees, respectively. The three rows correspond from top to bottom to the local tomographic reconstruction, FBP, and FBP with the consecutive TCG, respectively. The values (minimum, maximum) of the gray scale for (a–i) are (–0.8081, 1.0000), (–0.8302, 1.0000), (–0.7515, 1.0000), (–2.0745, 1.7899), (–0.6385, 1.0723), (–0.1030, 1.0349), (–0.9284, 1.2859), (–0.0326, 1.0030), and (–0.0149, 1.0021), respectively. The maxima of the local reconstructions are normalized to unity. (Reproduced from Xu, Y., L.V. Wang, G. Ambartsoumian, and P. Kuchment, *Med. Phys.* 31(4):724–33, 2005. With permission.)

6.4.2 Reconstruction from Experimental Limited View Thermoacoustic Tomography Data

The experimental setup is described in [23,67] and will not be repeated here. The sample and the polar coordinate system describing the scanning orbit are shown in Figure 6.8a. The sample consists of a muscle cylinder of 4 mm in diameter and 5 mm in length, embedded in a chunk of pork

fat of 1.2 cm in radius, r_f. There is a 10-mm fat layer below the muscle and another 7-mm one above it. An EM pulse is delivered to the sample from below (i.e., from behind the picture plane). With a scanning radius of $r_d = 7.1$ cm, thermoacoustic data are collected around the sample over a 2π angular span with 161 steps. The EM pulse profile and the impulse response function of the ultrasonic transducer impose a filter on the thermoacoustic signals. We
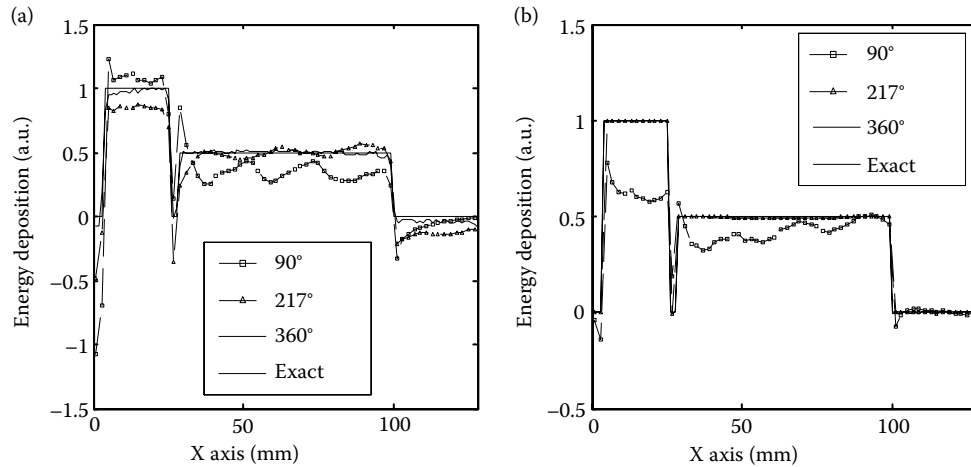
FIGURE 6.6 (a) The graphs of FBP reconstructions shown in Figure 6.5d through f, and the corresponding exact value along the dashed-dotted line in Figure 6.4. (b) The graphs corresponding to TCG reconstructions, Figure 6.5d through f, along the same line as in (a). (Reproduced from Xu, Y., L.V. Wang, G. Ambartsoumian, and P. Kuchment, *Med. Phys.* 31(4):724–33, 2005. With permission.)
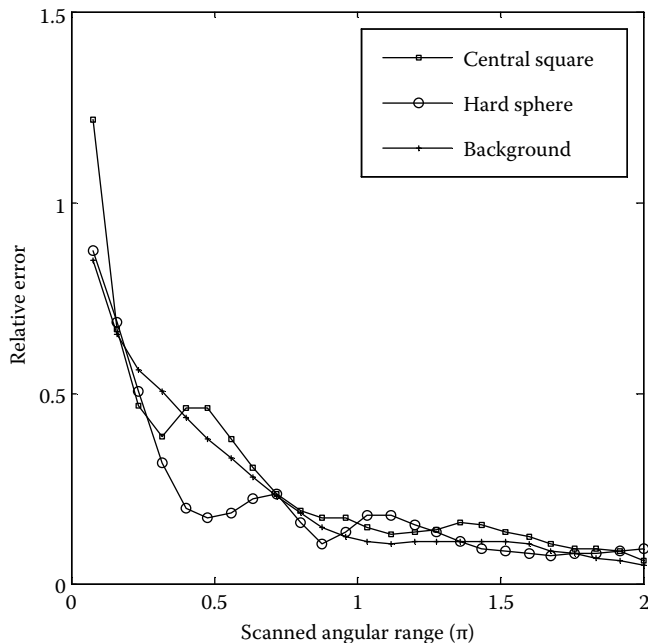
FIGURE 6.7 Dependence of the relative errors of the mean values in the hard sphere (circle markers), the central square (square markers), and the background (asterisks) on the scanned angular range. (Reproduced from Xu, Y., L.V. Wang, G. Ambartsoumian, and P. Kuchment, *Med. Phys.* 31(4):724–33, 2005. With permission.)

attempted to correct this effect using deconvolution, but found that the resulting images were distorted, due to the lack of precise knowledge of the filter. Therefore, we do not use deconvolution in the reconstruction. This leads, as explained earlier, to somewhat emphasized interfaces. Figure 6.8b through d show the reconstructed images using FBP with three sets of data. In Figure 6.8b, we choose the data collected along a circular detection arc of 92 degrees, located at the top of the picture and almost symmetric with respect to its vertical axes. One sees that the left and right

boundaries of the muscle cylinder and of the pork chunk are blurred away, since their normal lines do not touch the detection arc, while the rest of the boundary is sharp. The next figure shows the reconstructed image obtained with the data collected from a 202-degree arc, where the whole phantom fits into the detectable region. All boundaries are sharp now. Finally, the last figure shows the image reconstructed with the full-view data.

Notice that although no local reconstruction algorithms are applied, the boundaries are somewhat emphasized. The reason for this is the presence in the data of the impulse response function of the ultrasonic transducer, which has an effect similar to the application of an additional derivative with respect to the radius of the circle of integration. The presence of such a derivative emphasizes high frequencies and makes the reconstruction similar to a version of a local tomography algorithm.

6.4.3 DISCUSSION ON EXPERIMENTAL RESULTS

As mentioned earlier, although circular scanning is used in both our numerical and experimental studies, our conclusions can be applied to other configurations as well. In TAT with a planar configuration [62,64–66], detections are implemented on a part of a line or a plane where the scanning view is quite limited; consequently, artifacts and interface blurring appear in the reconstructed images. In fact, in planar and linear scanning geometries, one can never have an object immersed entirely into the "detectable region" because the normal lines to any interfaces that are orthogonal to the detection plane (line) never pass through a detector. As a consequence, those parts of the interfaces will be blurred in any kind of reconstruction. For a sufficiently large view, these parts will be small, but theoretically will never disappear. For example, 2D planar detection is utilized to image artificial blood vessels [64]; the scanning view is about 2.18 steradians. Therefore, it is not surprising that only the interfaces more-or-less parallel
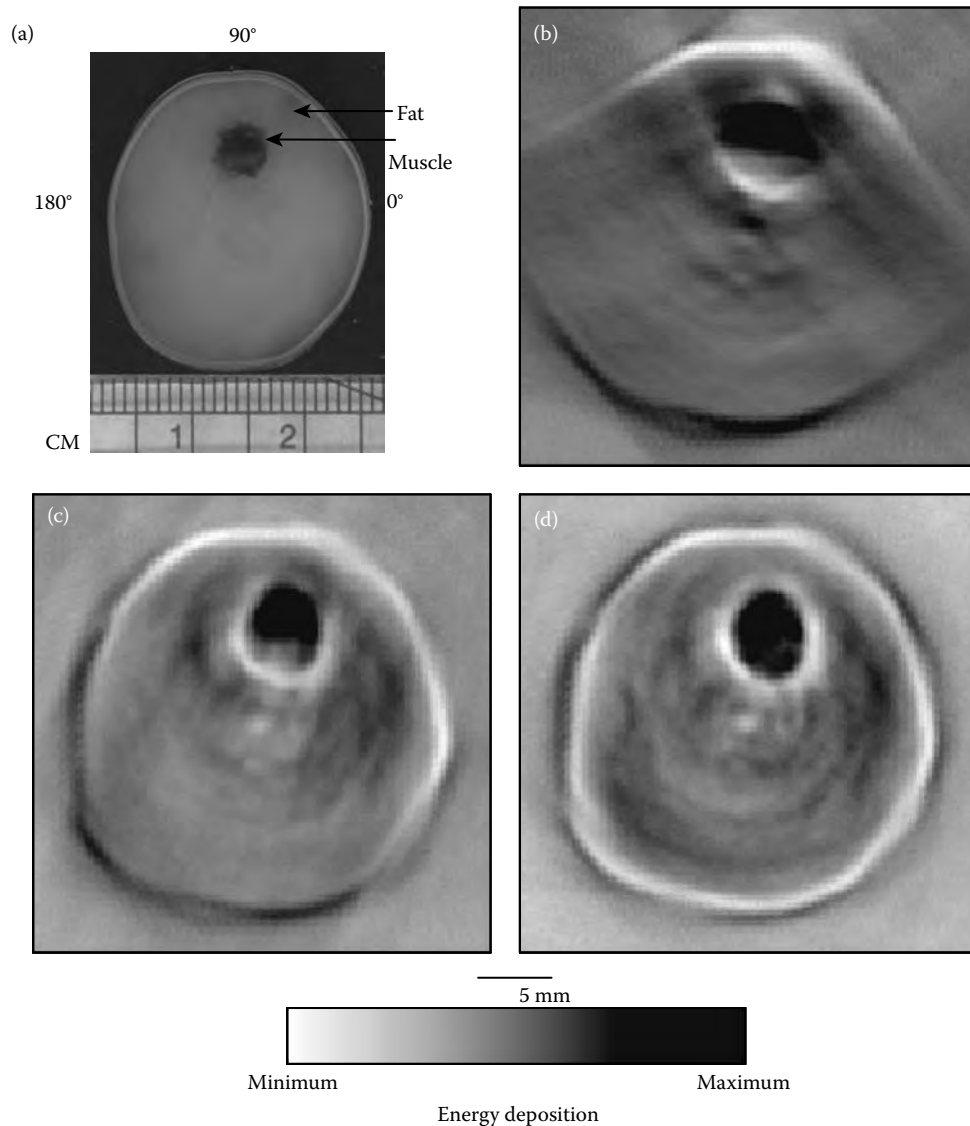
FIGURE 6.8 (a) Photograph of the experimental sample. (b–d) TAT images reconstructed using detection arcs of 92 degrees (from 50° to 142° in (a)), 202 degrees (from –18° to 184°), and 360 degrees, respectively. The blurred parts of the boundaries in (b) due to the limited view agree with the theoretical predictions. In (c) all the boundaries are resolved, since the object fits into the "detectable region". (Reproduced from Xu, Y., L.V. Wang, G. Ambartsoumian, and P. Kuchment, *Med. Phys.* 31(4):724–33, 2005. With permission.)

to the plane of detection are well imaged. Linear scanning detection was used in Ref. [66] to image a 2D phantom. Because the view of the linear scanning in Ref. [66] is much larger than that of planar scanning in Ref. [64], the interfaces are recovered much more completely. However, due to a limited view, artifacts and interface blurring similar to those demonstrated in our numerical and experimental studies still appear in the images [66].

By comparing Figures 6.5 and 6.8, we observe that the images reconstructed from incomplete data when an object is in the detectable region, have comparable quality with those from the full-view data. Scanning a smaller range has the advantages of reducing the scanning time or the size of the acoustic transducer array. It should be pointed out that this advantage usually exists when both the sample and medium are relatively acoustically homogeneous. When

strong wavefront distortion caused by acoustic heterogeneities occurs, it might be beneficial to collect signals from all directions.

6.5 ADDITIONAL REMARKS AND CONCLUSIONS

As mentioned before, one may incorporate some additional information about the image, or change the physical set-up of the problem to stabilize the inverse problem and make all or some formerly invisible interfaces visible. Recently, it was shown [70] that taking into account some *a priori* knowledge about the interfaces leads to reconstruction of previously invisible parts. In another direction, acoustic reflectors were proposed as a means of reflecting the acoustic waves, which would otherwise not be measured, back onto the sensor. It was

shown in that case an existing FFT-based image reconstruction algorithm can be used to reconstruct the image without the limited view-induced blurring [71,81].

The main points of this survey can be summarized as follows:

- A geometric principle is described that allows a simple determination of which sharp parts of the object are expected to be blurred when reconstructed from limited view thermoacoustic data.
- This blurring is independent of the particular reconstruction method and cannot be overcome, unless some extra information about the object is known.
- Numerical results using synthetic and experimental data are shown that support the conclusions.

ACKNOWLEDGMENTS

REFERENCES

1. Joines, W.T. 1980. Microwave-power absorption differences between normal and malignant-tissue. *Int. J. Radiat. Oncol. Biol. Phys.* 6:681–87.
2. Chaudhary, S.S. 1984. Dielectric-properties of normal and malignant human-breast tissues at radiowave and microwave-frequencies. *Indian J. Biochem. Biophys.* 21:76–79.
3. Joines, W.T., Y. Zhang, C.X. Li, and R.L. Jirtle. 1994. The measured electrical-properties of normal and malignant human tissues from 50 to 900 MHz. *Med. Phys.* 21(4): 547–50.
4. Cheong, W.F., S.A. Prahl, and A.J. Welch. 1990. A review of the optical-properties of biological tissues. *IEEE J. Quantum Electron.* 26 (12):2166–85.
5. Kruger, R.A., P.Y. Liu, Y.R. Fang, and C.R. Appledorn. 1995. Photoacoustic ultrasound (PAUS)—reconstruction tomography. *Med. Phys.* 22 (10):1605–609.
6. Oraevsky, A.A., and A.A. Karabutov. 2002. In *Handbook of optical biomedical diagnostics*, ed. V.V. Tuchin, Chap. 10. Bellingham, WA: SPIE.
7. Oraevsky, A.A., and A.A. Karabutov. 2003. Optoacoustic tomography. In *Biomedical photonics handbook*, ed. T. Vo-Dinh, Chap. 34. Boca Raton, FL: CRC.
8. Wang, L.V., and H. Wu. 2007. *Biomedical optics. Principles and imaging*. New York: Wiley-Interscience.
9. Xu, M., and L.-H. V. Wang. 2006. Photoacoustic imaging in biomedicine. *Rev. Sci. Instrum.* 77:041101-01–22.
10. Natterer, F. 1986. *The mathematics of computerized tomography*. New York: Wiley.
11. Quinto, E.T. 1993. Singularities of the x-ray transform and limited data tomography in R(2) and R(3). *SIAM J. Math. Anal.* 24(5):1215–25.
12. Ramm, A.G., and A.I. Zaslavsky. 1993. Reconstructing singularities of a function from its Radon Transform. *Math. Comput. Modelling* 18(1):109–38.
13. Delaney, A.H., and Y. Bresler. 1998. Globally convergent edge-preserving regularized reconstruction: An application to limited-angle tomography. *IEEE Trans. Image Processing* 7(2):204–21.
14. Pan, X.C., and M.A. Anastasio. 1999. Minimal-scan filtered backpropagation algorithms for diffraction tomography. *J. Opt. Soc. Am. A* 16(12):2896–2903.
15. Kuchment, P., and E.T. Quinto. 2003. Some problems of integral geometry arising in tomography, Chapter XI in L. Ehrenpreis *The universality of the radon transform*. Oxford: Oxford University Press.
16. Natterer, F., and F. Wübbeling. 2001. *Mathematical methods in image reconstruction*. Philadelphia, PA: SIAM.
17. Pan, X.C., Y. Zou, and M.A. Anastasio. 2003. Data redundancy and reduced-scan reconstruction in reflectivity tomography. *IEEE Trans. Image Processing* 12(7):784–95.
18. Kuchment, P., K. Lancaster, and L. Mogilevskaya. 1995. On local tomography. *Inverse Problems* 11(3):571–89.
19. Louis, A.K., and E.T. Quinto. 2000. Local tomographic methods in Sonar. In *Surveys on solution methods for inverse problems*, eds. D. Colton, H. Engl, A. Louis, J. McLaughlin, and W. Rundell, 147–54. Vienna: Springer.
20. Palamodov, V.P. 2000. Reconstruction from limited data of arc means. *J. Fourier Anal. Appl.* 6(1):25–42.
21. Patch, S.K. 2000. Moment conditions indirectly improve image quality. *Contemp. Math.* 278:193–205.
22. Patch, S.K. 2004. Thermoacoustic tomography – consistency conditions and the partial scan problem. *Phys. Med. Biol.* 49:1–11.
23. Xu, Y., L.V. Wang, G. Ambartsoumian, and P. Kuchment. 2004. Reconstructions in limited-view thermoacoustic tomography. *Med. Phys.* 31(4):724–33.
24. Paltauf, G., R. Nuster, M. Haltmeier, and P. Burgholzer. 2007. Experimental evaluation of reconstruction algorithms for limited view photoacoustic tomography with line detectors. *Inverse Problems* 23:S81–S94.
25. Paltauf, G., R. Nuster, P. Burgholzer, and M. Haltmeier. 2007. Three-dimensional photoacoustic tomography (PAT) using optical line detection of ultrasound. Lecture at the Workshop on Bioimaging, Johann Radon Institute for Computational and Applied Mathematics, Linz, Austria, 12–17 November.
26. Andreev, V., D. Sushko, A. Oraevsky, A. Karabutov, and D. Popov. 2002. Image reconstruction in 3D optoacoustic tomography system with hemispherical transducer array. *Proc. SPIE* 4618:1605-7422/02.
27. Anastasio, M.A., J. Zhang, E.Y. Sidky, Y. Zou, D. Xia, and X. Pan. 2005. Feasibility of half-data image reconstruction in 3-D reflectivity tomography with a spherical aperture. *IEEE Trans. Med. Imaging* 24(9):1100–12.
28. Finch, D., and Rakesh. 2007. The spherical mean value operator with centers on a sphere. *Inverse Problems* 23(6):S37–S50.
29. Patch, S.K., and O. Scherzer. 2007. Photo- and thermoacoustic imaging. *Inverse Problems* 23(6):S1–S10.
30. Kuchment, P., and L. Kunyansky. 2008. Mathematics of thermoacoustic tomography. *Eur. J. Appl. Math.* 19(2):191–224.
31. Agranovsky, M., P. Kuchment, and L. Kunyansky. 2009. On reconstruction formulas and algorithms for the thermoacoustic and photoacoustic tomography. In *Photoacoustic Imaging and Spectroscopy*, ed. Lihong Wang, 89–102, Boca Raton, FL: CRC press.

32. Finch, D., and Rakesh. 2009. Recovering a function from its spherical mean values in two and three dimensions. In *Photoacoustic Imaging and Spectroscopy*, ed. Lihong Wang, 77–88, Boca Raton, FL: CRC press.

33. Arfken, G.B., and H.J. Weber. 2005. *Mathematical methods for physicists*. New York: Academic Press.

34. Courant, R., and D. Hilbert. 1962. *Methods of mathematical physics, Volume II Partial differential equations*. New York: Wiley-Interscience.

35. Agranovsky, M.L., and E.T. Quinto. 1996. Injectivity sets for the Radon transform over circles and complete systems of radial functions. *J. Funct. Anal.* 139(2):383–414.

36. Xu, Y., and L.H.V. Wang. 2004. Time reversal and its application to tomography with diffracting sources. *Phys. Rev. Lett.* 92(3):4.

37. Xu, Y., and L.H.V. Wang. 2004. Time reversal and its application to thermoacoustic tomography. *Proc. SPIE* 5320:257–63.

38. Finch, D., S. Patch, and Rakesh. 2004. Determining a function from its mean values over a family of spheres. *SIAM J. Math. Anal.* 35(5):1213–40.

39. Palamodov, V.P. 2004. *Reconstructive integral geometry*. Basel: Birkhäuser.

40. Ambartsoumian, G., and Kuchment, P. 2005. On the injectivity of the circular Radon transform. *Inverse Problems* 21:473–85.

41. Kuchment, P. 2006. Generalized transforms of radon type and their applications. In *The Radon Transform, Inverse Problems, and Tomography. American Mathematical Society Short Course January 3–4, 2005, Atlanta, Georgia*, eds. G. Olafsson and E.T. Quinto, 67–91. Proc. Symp. Appl. Math., v. 63, Providence, RI: AMS.

42. Agranovsky, M., P. Kuchment, and E.T. Quinto. 2007. Range descriptions for the spherical mean Radon transform, *J. Funct. Anal.* 248:344–86.

43. Agranovsky, M., and P. Kuchment. 2007. Uniqueness of reconstruction and an inversion procedure for thermo-coustic and photoacoustic tomography. *Inverse Problems* 23:2089–102.

44. Kuchment, P. 1993. Unpublished.

45. Agranovsky, M., C. Berenstein, and P. Kuchment. 1996. Approximation by spherical waves in L_p-spaces. *J. Geom. Anal.* 6(3):365–83.

46. Fawcett, J.A. 1985. Inversion of n-dimensional spherical averages. *SIAM J. Appl. Math.* 45:336–41.

47. Andersson, L.E. 1988. On the determination of a function from spherical averages. *SIAM J. Math. Anal.* 19:214–32.

48. Nilsson, S. 1997. Application of fast backprojection techniques for some inverse problems of integral geometry, PhD thesis, Linkoping University, Linkoping.

49. Denisjuk, A. 1999. Integral geometry on the family of semi-spheres. *Fract. Calc. Appl. Anal.* 2:31–46.

50. Xu, Y., D.Z. Feng, and L.H.V. Wang. 2002. Exact frequency-domain reconstruction for thermoacoustic tomography – I: Planar geometry. *IEEE Trans. Med. Imaging* 21(7):823–28.

51. Norton, S.J. 1980. Reconstruction of a two-dimensional reflecting medium over a circular domain: Exact solution. *J. Acoust. Soc. Am.* 67:1266–73.

52. Norton, S.J., and M. Linzer. 1981. Ultrasonic reflectivity imaging in three dimensions: Exact inverse scattering solution for plane, cylindrical and spherical aperture. *IEEE Trans. Biomed. Eng.* BME-28:202–20.

53. Finch, D., M. Haltmeier, and Rakesh. 2007. Inversion of spherical means and the wave equation in even dimensions. *SIAM J. Appl. Math.* 68(2), 392–412.

54. Xu, M., and L.-H.V. Wang. 2005. Universal back-projection algorithm for photoacoustic computed tomography. *Phys. Rev. E* 71:016706.

55. Kunyansky, L., 2007. Explicit inversion formulae for the spherical mean Radon transform. *Inverse Problems* 23:373–83.

56. Rubin, B. 2007. Spherical means in odd dimensions and EPD equations. Preprint arXiv:arXiv:0711.1897.

57. Kunyansky, L. 2007. A series solution and a fast algorithm for the inversion of the spherical mean Radon transform. *Inverse Problems* 23(6):S11–S20.

58. Popov, D.A., and D.V. Sushko. 2002. A parametrix for the problem of optical-acoustic tomography. *Dokl. Math.* 65(1):19–21.

59. Popov, D.A., and D.V. Sushko. 2004. Image restoration in optical-acoustic tomography. *Problems Inform. Transmission* 40(3):254–78.

60. Burgholzer, P., G. Matt, M. Haltmeier, and G. Paltauf. 2007. Exact and approximate imaging methods for photoacoustic tomography using an arbitrary detection surface. *Phys. Rev. E* 75:046706.

61. Hristova, Y., P. Kuchment, and L.V. Nguyen. 2008. On reconstruction and time reversal in thermoacoustic tomography in acoustically homogeneous and inhomogeneous media. *Inverse Problems* 24:055006.

62. Hoelen, C.G.A., F.F.M. de Mul, R. Pongers, and A. Dekker. 1998. Three-dimensional photoacoustic imaging of blood vessels in tissue. *Opt. Lett.* 23(8):648–50.

63. Kostli, K.P., M. Frenz, H. Bebie, and H.P. Weber. 2001. Temporal backward projection of optoacoustic pressure transients using Fourier transform methods. *Phys. Med. Biol.* 46(7):1863–72.

64. Hoelen, C.G.A., and F.F.M. de Mul. 2000. Image reconstruction for photoacoustic scanning of tissue structures. *Appl. Opt.* 39(31):5872–83.

65. Ku, G., and L.H.V. Wang. 2001. Scanning microwave-induced thermoacoustic tomography: Signal, resolution, and contrast. *Med. Phys.* 28(1):4–10.

66. Feng, D.Z., Y. Xu, G. Ku, and L.V. Wang. 2001. Microwave-induced thermoacoustic tomography: Reconstruction by synthetic aperture. *Med. Phys.* 28(12):2427–31.

67. Xu, M.H., and L.H.V. Wang. 2002. Time-domain reconstruction for thermoacoustic tomography in a spherical geometry. *IEEE Trans. Med. Imaging* 21(7):814–22.

68. Xu, Y., M.H. Xu, and L.H.V. Wang. 2002. Exact frequency-domain reconstruction for thermoacoustic tomography - II: Cylindrical geometry. *IEEE Trans Med. Imaging* 21(7):829–33.

69. Haltmeier, M., T. Schuster, and O. Scherzer. 2005. Filtered backprojection for thermoacoustic computed tomography in spherical geometry. *Math. Methods Appl. Sci.* 28:1919–37.

70. Wang, L.H.V., and X.M. Yang. 2007. Boundary conditions in photoacoustic tomography and image reconstruction. *J. Biomed. Opt.* 12(1):10.

71. Cox, B.T., and P.C. Beard. 2007. Exact photoacoustic image reconstruction using a planar sensor array and image sources. *SPIE* 6437:64371H.

72. Strichartz, R.S. 2003. *A guide to distribution theory and Fourier transforms*. Singapore: World Science.

73. Quinto, E.T. 1980. The dependence of the generalized Radon transform on defining measures. *Trans. Am. Math. Soc.* 257:331–46.

74. Beylkin, G. 1984. The inversion problem and applications of the generalized radon-transform. *Commun. Pure Appl. Math.* 37:579–99.

75. Noo, F., and J.-M. Wagner, 2001. Image reconstruction in 2*D* SPECT with 180° acquisition. *Inverse Problems* 17:1357–71.

76. Rullgård, H. 2004. An explicit inversion formula for the exponential Radon transform using data from 180°. *Ark. Mat.* 4(2):353–62.

77. Kunyansky, L. 2008. Thermoacoustic tomography with detectors on an open curve: an efficient reconstruction algorithm. *Inverse Problems* 24(5):055021.

78. Faridani, A., E.L. Ritman, and K.T. Smith. 1992. Examples of local tomography. *SIAM J. Appl. Math.* 52(4):1193–98.

79. Faridani, A., E.L. Ritman, and K.T. Smith. 1992. Local tomography. *SIAM J. Appl. Math.* 52(2):459–84.

80. Faridani, A., D.V. Finch, E.L. Ritman, and K.T. Smith. 1997. Local tomography. 2. *SIAM J. Appl. Math.* 57(4): 1095–1127.

81. Cox, B.T., S.R. Arridge, and P.C. Beard. 2007. Photoacoustic tomography with a limited-aperture planar sensor and a reverberant cavity. *Inverse Problems* 23:S95–S112.

SOME PROBLEMS OF INTEGRAL GEOMETRY IN ADVANCED IMAGING

by

RIM GOUIA

Presented to the Faculty of the Graduate School of

The University of Texas at Arlington in Partial Fulfillment

of the Requirements

for the Degree of

DOCTOR OF PHILOSOPHY

THE UNIVERSITY OF TEXAS AT ARLINGTON

May 2011

بسم الله الرحمن الرحيم

In the name of GOD, Most Gracious, Most Merciful

ACKNOWLEDGEMENTS

First of all, I am grateful to my supervising professor Dr. Gaik Ambartsoumian for his constant support, his thoughtful leadership and invaluable advice. His patience, seriousness, and commitment have helped me grow academically and face challenging problems with confidence. These words are too short of truly thanking his understanding and guidance. I will forever be in debt to him.

I thank my academic advisors Dr. Su, Dr. Liao, Dr. Aktosun, Dr. Lewis, and Dr. Kojouharov for their interest in my research and for their kind agreement to serve in my dissertation committee. I also thank my academic advisors, Dr. Grantcharov, and Dr. Burghduff for taking the time to write my recommendation letters and for contributing to my professional success.

I acknowledge all the faculty and staff at the Department of Mathematics at the University of Texas at Arlington, who helped me to finish my Ph.D. and all the friends that I met as a graduate student, especially the following people: Dr. Zhu, Dr. Hawkins, Dr. Jorgensen, Dr. Shipman, Dr. Korzeniowski, Dr. Gornet, Dr. Liu, Dr. Pankavich, Dr. Vancliff, Mr. Smith, Dr. Topsakal, Vishti, Kim, Cecelia, Shelley, Beth, Manizheh, Padmini, Alicia, Jennifer, Kristen, Angela and Julie... (I am missing many more).

I am grateful to all the teachers who taught me during my years in school in Tunisia and France. I owe special thanks to those special math professors Dr. Boukrisha, Mr. Latrach, and Dr. Colin who inspired me through my high school and undergraduate studies.

Last and definitely not the least, none of this would have been close to reality if not for my graceful parents Dr. Houda Abdellah and Dr. Ridha Gouia and their unconditional love and support. They inspired every moment of my life from the baby steps to dreams and aspirations I carry in my heart. I will never be able to return their favors on me. I can only pray for their blessing. I forever indebted to my husband Samir and my beloved son Mohamed-Aziz for their unconditional support and love, no matter what the circumstances were.

March 30, 2011

ABSTRACT

SOME PROBLEMS OF INTEGRAL GEOMETRY IN ADVANCED IMAGING

Rim Gouia, Ph.D.

The University of Texas at Arlington, 2011

Supervising Professor: Dr. Ambartsoumian

During the past decade, our society has become dependent on advanced mathematics for many of our daily needs. Mathematics is at the heart of the 21st century technologies and more specifically the emerging imaging technologies from thermoacoustic tomography (TAT) and ultrasound computed tomography (UCT) to nondestructive testing (NDT). All of these applications reconstruct the internal structure of an object from external measurements without damaging the entity under investigation. The basic mathematical idea common to such reconstruction problems is often based upon Radon integral transform.

The Radon integral transform $R : f \mapsto Rf$ puts into correspondence to a given function f its integrals over certain subsets. In this work, we focus on the situation when the subsets are circles. The major problems related to this transform are the existence and uniqueness of its inversion, inversion formulas, and the range description of the transform. When Rf is known for circles of all possible radii, there are well developed theories addressing most of the questions mentioned above. However, many of these questions are still open when Rf is available for only a part of all possible radii.

The aim of my dissertation is to derive some new results about the existence and uniqueness of the representation of a function by its circular Radon transform

with radially partial data for both interior and exterior problems. The presented new results open new frontiers in the field of medical imaging such as intravascular ultrasound (IVUS) and transrectal ultrasound (TRUS).

TABLE OF CONTENTS

LIST OF FIGURES

LIST OF TABLES

CHAPTER 1

INTRODUCTION

During the past decade, our society has become dependent on advanced mathematics for many of our daily needs. Mathematics is at the heart of the 21st century technologies and more specifically the emerging imaging technologies from thermoacoustic tomography (TAT) and ultrasound computed tomography (UCT) to nondestructive testing (NDT). All of these applications reconstruct the internal structure of an object from external measurements without damaging the entity under investigation. Very often the basic mathematical idea common to such reconstruction problems is based upon integral geometry.

In accordance with the terminology used by I. Gelfand and G. Shilov in [31], integral geometry is the branch of geometrical analysis that analyzes integral transforms of geometrical nature. More specifically, integral geometry is dealing with properties of functions that can be determined by transforms integrating the function over subsets. This type of transforms are named Radon integral transforms after the Austrian mathematician, Johann Radon (1887-1956), who studied the transform that integrates functions of two independent variables over all lines in the plane for pure mathematical reasons. In 1963, the physicist Allan M. Cormack reinvented the classical Radon transform and supplanted it as the mathematical model of X-ray computed tomography (CT) in which the internal structure of an object can be determined by its integrals over all lines in the plane. Based upon Cormack's work, the engineer Godfrey Hounsfield invented the CT that revolutionized the field of medical imaging and resulted in the 1979 Nobel Prize in Physiology and Medicine.

The success of this imaging method and the tremendous improvement in the computing capabilities boosted the connection between integral geometry and medical

imaging as well as other fields of imaging such as non-destructive testing, geophysics, radar and sonar. Indeed, integral geometry is used in medicine to visualize internal organs, in non-destructive testing to evaluate the thickness of objects and flaws in materials, in geophysics to explore oil and gas, and in remote sensing to detect objects and monitor risk areas.

In the next chapter, we give a brief survey of some of the major imaging applications that deal with reconstructing the internal structure of an object without causing damage to it. The basic mathematical idea common to such reconstruction problems is based upon integral transforms of Radon type. In chapter 3, some of these transforms are defined and studied from a theoretical point of view. We first define the classical Radon transform, then we generalize it to the spherical and the elliptical Radon transforms, which are more relevant tools in the imaging applications that we consider. In chapter 4, we discuss some of the main mathematical problems that typically arise while determining a function from its Radon transforms. We start by a quick summary of the results regarding the inversion of the classical Radon transform in $\mathbb{R}^2$. We provide some of the important techniques that are used in the case of main interest. Then we intensively study the inversion of the spherical Radon transform in $\mathbb{R}^2$ and in $\mathbb{R}^n$ for $n > 2$. Once we show some of the techniques of reconstruction using complete data of the spherical Radon transform, we then concentrate, in chapter 5, on the question of representing a function by its circular Radon transform with partial data. We focus on the case of transforms integrating functions of two independent variables along circles, and present a new inversion formula when the Radon transform is known for only a part of all possible radii, for both interior and exterior problems. Finally in chapter 6, an approximate backprojection algorithm is developed to recover a 2D function from its integrals over a family of ellipses. We

also present the results of the numerical simulation where the center of the ellipses is rotating around the origin.

CHAPTER 2

MAJOR FIELDS OF APPLICATION

There are numerous imaging applications that deal with reconstructing the internal structure of an object without causing damage to it. The basic mathematical idea common to many of such reconstruction problems is based upon integral geometry. In this chapter, we describe some of the typical applications that use integral geometry in their mathematical models.

2.1   X-ray computed tomography

X-ray computed tomography, abbreviated to CAT or CT, consists of a tube emitting a thin collimated beam of X-rays that penetrates the object under investigation, and of a detector, which is recording the intensity loss of the transmitted X-rays. By rotating the source and the detector in the same plane around the patient, it is possible to obtain a set of projections. This collected data is processed by a computer to produce an image of the internal structure of the object from the external
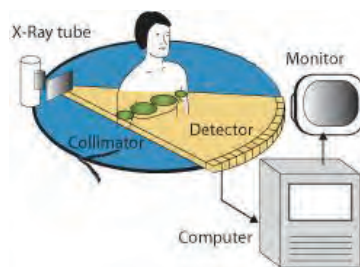
Figure 2.1. Principle of measurement of an X-ray computed tomography.

measurements. Invented by the engineer Godfrey Hounsfield and the physicist Allan Cormack in 1972, the CT revolutionized the field of medical imaging.

As X-rays travel along a line L from the X-ray source through the object to an X-ray detector, the energy is attenuated by the material on the line L. The attenuation coefficient $f(x)$ at the point x is the function that quantifies the tendency of an object to absorb X-rays. Assuming all X-rays are sent in the same plane $x = (x_1, x_2)$ is a two dimensional variable, and $f(x)$ represents an image of a cross-sectional slice of the body. Let $I_{(\text{source})}$ and $I_{(\text{detector})}$ are, respectively, denote the initial intensity of the beam and the intensity of the beam after passing the object. So the relative intensity loss when the X-rays traverse a distance $\triangle x$ is

$$\triangle I / I = -f(x) \triangle x.$$

By integrating from the source to the detector, we get the following integral transform

$$\ln \left[\frac{I_{(\text{source})}}{I_{(\text{detector})}} \right] = \int_L f(x) dx.$$

Since $I_{(\text{source})}$ and $I_{(\text{detector})}$ are measured, the line integrals of the attenuation coefficient f along each of the lines L are known and can be used to reconstruct f. It is this mathematical model upon which CT is used in medicine as well as in industry for internal inspection of components, flaw detection, failure analysis, and metrology. An in-depth discussion of the X-ray tomography can be found in [23, 25, 33].

2.2   Ultrasound tomography

Ultrasound tomography is very similar to X-ray tomography. In both cases, we are trying to reconstruct a cross-sectional image from the recorded data. However, when using ultrasound as a form of energy to illuminate the object, the transmitted signal is almost immeasurable as most of the the energy is reflected by density contrasts. Hence, the reconstruction is done using reflected signals (Figure 2.2).
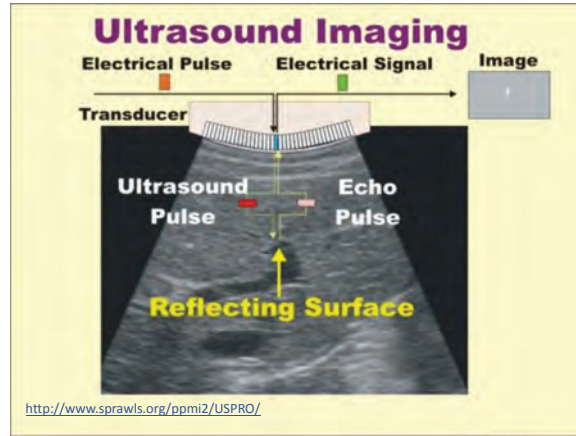
Figure 2.2. The basic ultrasound imaging process.
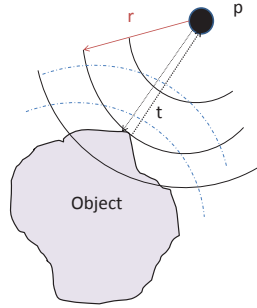
Figure 2.3. The receiver coincides with the source.

The transducer placed at the edge of the body works in dual modes first as an emitter of sound waves, and then as a receiver, registering the reflection of ultrasound waves from the inclusions inside the body.

Assuming that (1) the pulse radiates isotropically in the form of expanding spherical waves, (2) the speed of sound propagation c is constant, (3) the receiver coincides with the source, and (4) the medium is weakly reflecting (here by weakly reflecting we mean that multiple reflections are ignored), the signals registered by a transducer at any moment of time t would be generated by inclusions lying on a

sphere of radius $r = ct/2$ (Figure 2.3) centered at the transducer location. In other words, the recorded data $g(p, r)$ is surface integrals over spheres $S(p, r)$ centered at the transducer locations p and of radius $r = ct/2$.

$$g(p, r) = \int_{S(p,r)} f(x) \, d\sigma.$$

By moving the transducer over a hyperplane or on a hypersphere around the object, it is possible to collect enough data to reconstruct the image of the entire object.

One needs to notice that in the case of the omission of one of these assumptions, the spherical integral geometry is no longer valid. For example, in a bistatic setup where the receiver and the source are no longer collocated, the collected data $g(r, s, t)$ is the integrals of the image function f along ellipses with foci the source s and the receiver r, and semi-major axis $t/2$ (see e.g. [39, 40]). This leads us to another integral transform

$$g(r, s, t) = \int_{E(r,s,t)} f(x) \, d\sigma.$$

To reduce the imaging geometry to two dimensions, we consider a transducer that generates a cylindrical wavefront instead of spherical wavefront. This can be achieved in practice by using a transducer that focuses in the axial direction and reduce the thickness of the lateral direction.

The most well known application of ultrasound tomography is its use in medical imaging to produce pictures of the internal structure of the human body. Moreover, there are a vast number of other applications including radar imaging (Figure 2.5) and sonar (see e.g. [16, 18, 38]) for the case where the receiver coincides with the
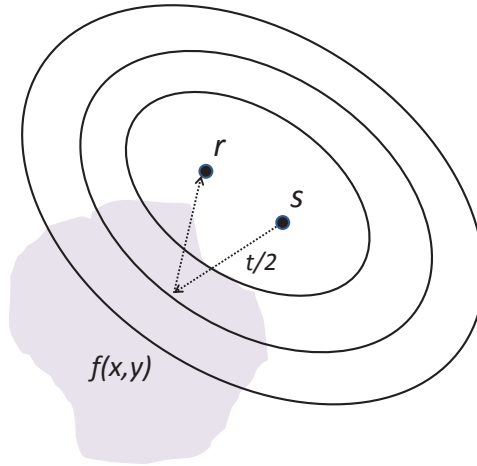
Figure 2.4. The receiver and the source are no longer collocated.

source, and geophysics (Figure 2.6) for the case where the receiver and the source are not collocated.

2.3 Thermoacoustic/photoacoustic tomography

Thermoacoustic tomography (TAT) and photoacoustic (PAT) tomography are two emerging medical imaging modalities based on a physical effect originally discovered by Alexander Graham Bell in 1880. These novel hybrid methods combine the advantages of optical absorption contrast with ultrasonic spatial resolution (see [3, 34] for a comprehensive survey on mathematical problems in TAT and PAT).

The part of the human body being imaged is exposed to a short pulse of electromagnetic (EM) radiation (radio-frequency (RF) waves in TAT, and lasers in PAT). A portion of this radiation is absorbed in the body, heating up the tissue, and causing
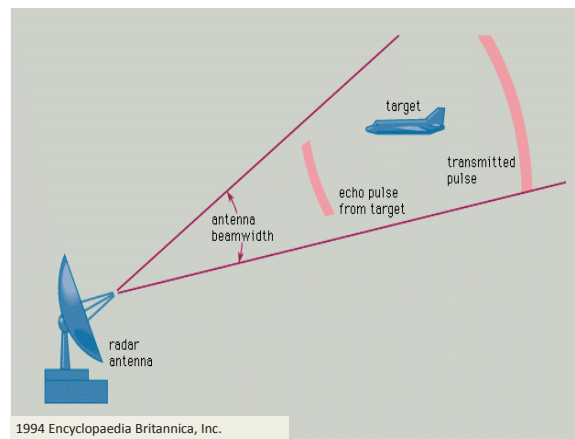
Figure 2.5. Radar.
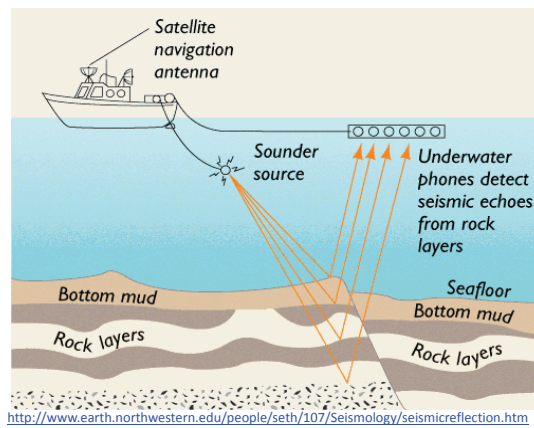
Figure 2.6. Geophysics.

thermal expansion, which in turn generates pressure waves (an ultrasound signal) traveling through the body. These acoustic waves are measured by multiple trans-ducers placed along the body. Then the collected data is processed to generate an image of the heat absorption function inside the body. The premise here is that there exists a strong contrast in the amount of absorbed EM energy between different types of tissues. For example cancerous cells absorb several times more energy than the healthy ones, hence recovery of the RF absorption function inside the body can help

RF pulse

r=ct

transducer

Thermoacoustic tomography
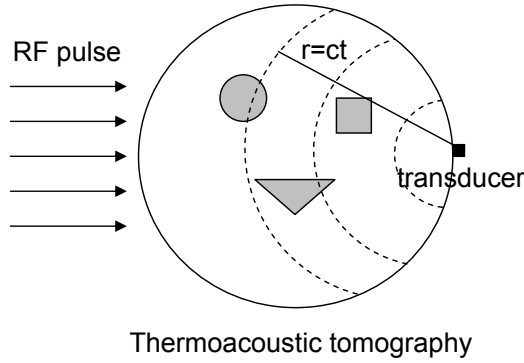
Figure 2.7. A sketch of TAT/PAT.

both to diagnose and to locate cancer. Figure 2.7 illustrates the process by which TAT and PAT are generated.

Since sound waves have very weak contrast in the tissue, we can simplify the model assuming the sound speed c to be constant in the body. Under this assumption the signals registered by a transducer at any moment of time t would be generated by inclusions lying on a sphere of radius $r = ct$ centered at the transducer location. Thus the problem of image reconstruction in TAT and PAT is equivalent to the recovery of the RF absorption function (the image to be reconstructed) from its integrals along spheres centered at available transducer locations. To reduce the imaging process to two dimensions, we limit the detection to circular signals by focusing the microphone to the plane.

In this chapter, we have concentrated on some of the imaging applications in which integral geometry has been found useful. Although a lot of advances have been made in this field, there are still cases (e.g. incomplete data problems) when the desired resolution and contrast are not yet achieved. Therefore, there remains a compelling need for the advancement of integral geometry and more specifically of

the knowledge about integral transforms of Radon type. That is what motivates our study in the upcoming chapters.

CHAPTER 3

SOME RADON INTEGRAL TRANSFORMS

The problem of image reconstruction in all the applications presented in the previous chapter, is equivalent to the recovery of the unknown function f from the collection of measured data Rf which is the set of integrals of the function f over certain hypersurfaces. In this chapter, we present a mathematical description of the relations between f and Rf for various choices of integration subsets. These relations are named Radon integral transforms after the Austrian mathematician J. Radon (1887-1956), who studied the transform that integrates functions of two and three independent variables respectively over lines and hyperplanes. It was later generalized to higher dimensions, and extended to broader geometries in the context of integral geometry introduced by I. Gelfand and G. Shilov in [31].

Next, we define and study some of the generalized Radon integral transforms from a theoretical point of view. First, we define the integral transform along the simplest path which is the straight line, called the classical Radon transform [1]. Then we generalize it to the spherical and the elliptical Radon transforms which are more relevant tools in advanced imaging that we consider.

3.1   Classical Radon transform

- Two dimensions

The classical Radon transform in 2D maps a function on $\mathbb{R}^2$ into the set of its integrals over straight lines in the plane. Let (x, y) designate coordinates of points in the plane and $f(x,y)$ be an arbitrary function defined on some domain $D \subset \mathbb{R}^2$. The classical

---

[1]While this is not the topic of our research, some of the methods and approaches developed for the study of these transforms prove to be useful for our models later.
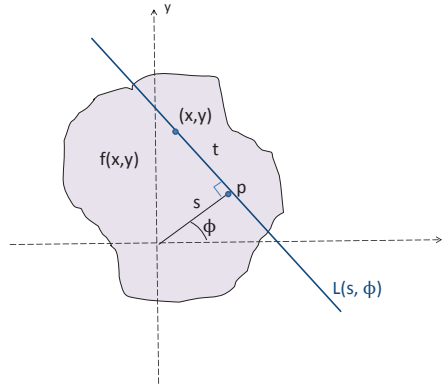
Figure 3.1. Geometric setup of integration along the line $L(s, \phi)$.

Radon transform Rf of f is a function defined on the space of straight lines L in $\mathbb{R}^2$ by the integral of f along each such line:

$$Rf(L) = \int_L f(x, y) \, dl,$$

where dl is the arc length element along L. The lines in the plane can be parameterized by 2 variables (s, ϕ), s.t. $L(s, \phi)$ denotes the line at oriented distance s from the origin and perpendicular to the vector $(\cos(\phi), \sin(\phi))$ (see Figure 3.1). Any point (x, y) along $L(s, \phi)$ can be parameterized by:

$$x(t) = s \cos \phi - t \sin \phi,$$

$$y(t) = s \sin \phi + t \cos \phi,$$

where the parameter $t \in (-\infty, \infty)$ is the signed distance measured from p to the point (x, y) on L (see Figure 3.1). The classical Radon transform can be expressed in these coordinates by

$$Rf(s, \phi) = \int_{-\infty}^{\infty} f(s \cos \phi - t \sin \phi, s \sin \phi + t \cos \phi) \, dt.$$

Alternative notation using the one-dimensional Dirac δ function is

$$Rf(s, \phi) = \int_{-\infty}^{\infty} \int_{-\infty}^{\infty} f(x, y)\, \delta(x \cos \phi + y \sin \phi - s)\, dx\, dy.$$

Note that Rf is an even function in the sense that

$$Rf(s, \phi) = Rf(-s, -\phi). \tag{3.1}$$

- Higher dimensions

More generally, in the n-dimensional space $\mathbb{R}^n$, the classical Radon transform maps a function on $\mathbb{R}^n$ into the set of its integrals over hyperplanes. Points in $\mathbb{R}^n$ are denoted by single letters $x = (x_1, x_2, \cdots, x_n)$ and functions defined on $\mathbb{R}^n$ by $f(x) = f(x_1, x_2, \cdots, x_n)$. The unit sphere in $\mathbb{R}^n$ is denoted by S^{n-1}. Let $H(s, \phi) = \{s \in \mathbb{R} : x \cdot \phi = s\}$ be the hyperplane orthogonal to $\phi \in S^{n-1}$ with oriented distance s from the origin. Using these notations, the classical Radon transform of f is defined by

$$Rf(s, \phi) = \int_{H(s, \phi)} f(x)\, dx.$$

Alternative notation is

$$Rf(s, \phi) = \int_{x \cdot \phi = s} f(x)\, dx.$$

We can also generalize the classical Radon transform by integrating over k-dimensional subspaces of $\mathbb{R}^n$; see, e.g. [32]. The ray transform is the most common case of this generalization, and is obtained by integrating functions over straight lines in $\mathbb{R}^n$. Thus for $n = 2$, the classical Radon transform and the ray transform differ only in the notation.

As previously explained, a simple imaging modality using the classical Radon transform is the X-ray tomography that consists of line integrals of the attenuation coefficient along all lines in the plane. A more precise definition of X-ray tomography can be found in chapter 2.
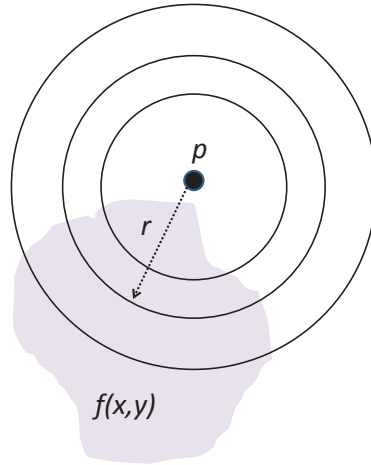
Figure 3.2. Geometric setup of integration along the circle $C(p, r)$.

3.2 Spherical Radon transform (SRT)

One can generalize the classical Radon transform to the spherical Radon transform for functions defined on $\mathbb{R}^2$, then on $\mathbb{R}^n$ as follows.

- Two dimensions

As the circle is the simplest curve in the plane next to the straight line, by analogy with the classical Radon transform, we define the circular Radon transform (CRT) of a function to be the path integral of the function along a circle of radius r and centered at the point $p \in \mathbb{R}^2$.

Let $f(x, y)$ be a continuous function on $\mathbb{R}^2$, then the CRT can be written as

$$Rf(p, r) = \int_{C(p,r)} f(x, y) \, dl,$$

where dl is the arc length element on the circle $C(p, r)$ of radius r and centered at $p \in \mathbb{R}^2$. Alternative notation using the one-dimensional Dirac δ function is

$$Rf(p, r) = \int_{-\infty}^{\infty} \int_{-\infty}^{\infty} f(x, y) \, \delta(r - \sqrt{x^2 + y^2}) \, dx \, dy.$$

Remark: Although a lot of problems related to these Radon integral transforms have direct applications to mathematical models of modern technologies, some of them are investigated for pure theoretical reasons as they raise interesting and challenging mathematical questions.

- Extension to higher dimensions

More generally, in the n-dimensional space $\mathbb{R}^n$, we define the spherical Radon transform of a function to be the surface integral of the function along a hypersphere of radius r and centered at the point $p \in \mathbb{R}^n$. Let $f(x)$ be a continuous function on $\mathbb{R}^n$, then the spherical Radon transform of f can be written as

$$Rf(p, r) = \int_{|x-p|=r} f(x)\, d\sigma,$$

where $d\sigma$ is the area element on the sphere $|x - p| = r$ centered at $p \in \mathbb{R}^n$.

As mentioned before, the spherical Radon transform is commonly used in the reconstruction procedure adopted in ultrasound tomography. Indeed, under certain physical assumptions (1) the pulse radiates isotropically in the form of expanding spherical waves, (2) the speed of sound propagation c is constant, and (3) the receiver coincides with the source the problem of image reconstruction in ultrasound tomography is equivalent to the recovery of the image function f from Rf data along spheres centered at available transducer locations. Chapter 2 provides a more detailed description of ultrasound tomography and its imaging technique.

As mentioned before, in the case of the omission of one of these assumptions, the collected data Rf is the integrals of the image function f along ellipses with foci the source and the receiver locations. This leads us to the next section on the study of the elliptical Radon transform.
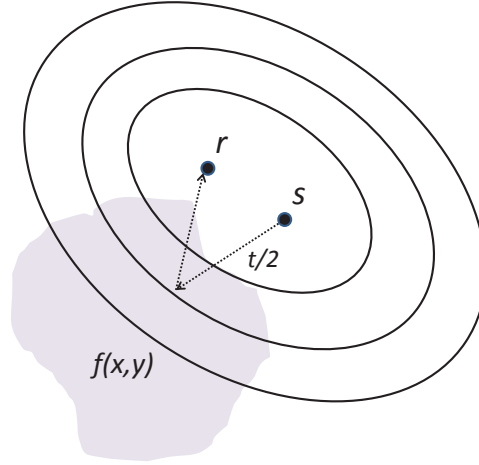
Figure 3.3. Geometric setup of integration along the ellipse $E(r, s, t)$.

3.3 Elliptical Radon transform (ERT)

We define the elliptical Radon transform of a function to be the path integral of the function along an ellipsoid of rotation with semi-major axis $t/2$ and foci $r, s \in \mathbb{R}^n$ (see e.g. [39, 40]).

- Two dimensions

Let $f(x, y)$ be a continuous function on $\mathbb{R}^2$, then the elliptical Radon transform can be written as

$$Rf(r, s, t) = \int_{E(r,s,t)} f(x, y) \, dl,$$

where dl is the arc length element on the ellipse $E(r, s, t)$. In this work, we only consider the 2D case, and possible future work can be done in 3D case.

Through this chapter, we presented some Radon integral transforms from a theoretical point of view and how they are related to data measured in applications. Therefore, the inverse problem that we consider is to reconstruct the unknown image

function f from the collection of measurements Rf. This reconstruction problem is equivalent to that of inverting the operator R defined as follows:

$$R: \quad f \longrightarrow Rf$$

$$\text{Unknown?} \longrightarrow \text{Data.}$$

Many mathematical problems naturally arise while studying the inversion question such as the existence and uniqueness of the inversion, inversion formulas and algorithms, the stability of these inversion algorithms, and the range of the Radon transforms (What conditions must the data satisfy?). These problems, with the exception of the stability and range descriptions, will be discussed intensively in the next chapter. For the detailed description and known results about stability and range descriptions, we refer the reader to papers [4, 10, 29, 56].

CHAPTER 4

MAIN MATHEMATICAL PROBLEMS AND KNOWN RESULTS

Among the major problems that naturally arise while studying the Radon integral transforms are the existence and uniqueness of their inversions, and inversion formulas and algorithms (e.g. [24, 42, 43]). These problems will be discussed throughout this chapter. We start by a quick summary of the results regarding the inversion of the classical Radon transform in $\mathbb{R}^2$ without providing details, as they are not our case of main interest [1]. Then we discuss in more details the inversion of the spherical Radon transform in $\mathbb{R}^2$ and in $\mathbb{R}^n$ for $n > 2$.

4.1   Classical Radon transform

Despite the discovery of the inversion formula of the classical Radon transform derived by J. Radon in his early work in 1917 for pure mathematical reasons, very little attention was given to implementing the inversion in a practical situation prior to the pioneering work of A. Cormack in [19] who won the Nobel Prize in Physiology and Medicine in 1979. Since then, this field has been investigated intensively. Today, there are well developed theories addressing the reconstruction problem. Several different approaches exist in the literature for inverting the classical Radon transform. The first one we introduce employs the harmonic decomposition technique used by A. Cormack. Then, we present the Fourier slice theorem, establishing a connection between the Fourier transform and the Radon transform. In the third section, we explore the most popular implementation of the Fourier slice theorem called filtered backprojection formula.

---

[1] While this is not the topic of our research, some of the methods and approaches developed for the study of these transforms prove to be useful for our models later.

19
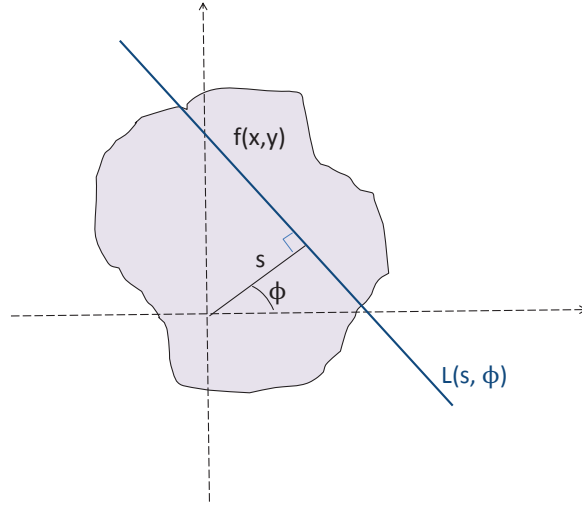
Figure 4.1. Coordinates to describe the line $L(s, \phi)$.

4.1.1 The Cormack method

Let $f(r, \theta)$ denote an unknown function supported inside the unit disc centered at the origin, where (r, θ) are polar coordinates measured from the center of the disc.

The classical Radon transform of f along the line L defined by the parameters (s, ϕ) is denoted by

$$g(s, \phi) = Rf(s, \phi) = \int_L f(r, \theta) \, dl. \tag{4.1}$$

Equation (4.1) is an integral equation in two variables but it may be reduced to a set of integral equations in one variable as follows. Since $f(r, \theta)$ and $g(s, \phi)$ are periodic with respect to the corresponding angular variables θ and ϕ, they can be expanded as Fourier series

$$f(r, \theta) = \sum_{n=-\infty}^{\infty} f_n(r) \, e^{in\theta}, \tag{4.2}$$

$$g(s, \phi) = \sum_{n=-\infty}^{\infty} g_n(s) \, e^{in\phi}, \tag{4.3}$$

where the Fourier coefficients $f_n(r)$ and $g_n(s)$ are computed by

$$f_n(r) = \frac{1}{2\pi} \int_0^{2\pi} f(r,\theta)\, e^{-in\theta} d\theta, \qquad (4.4)$$

$$g_n(s) = \frac{1}{2\pi} \int_0^{2\pi} g(s,\phi)\, e^{-in\phi} d\phi. \qquad (4.5)$$

The relation between $g_n(s)$ and $f_n(r)$ is given in [19] as

$$g_n(s) = 2 \int_s^1 \frac{f_n(r)\, T_{|n|}(s/r)\, r\, dr}{(r^2 - s^2)^{\frac{1}{2}}}, \qquad (4.6)$$

where $T_n(x)$ is the n-th order Tchebychev polynomial of the first kind (e.g. see [50]). It is easy to notice that by passing to the basis of complex exponentials, A. Cormack diagonalized the classical Radon transform, i.e. the n-th Fourier coefficient of g depends only on n-th Fourier coefficient of f. Equation (4.6) has the solution

$$f_n(r) = -\frac{1}{\pi} \frac{d}{dr} \int_r^1 \frac{g_n(s)\, T_{|n|}(s/r)\, s\, ds}{s(s^2 - r^2)^{\frac{1}{2}}}. \qquad (4.7)$$

This formula is called Cormack's first inversion formula. Cormack's second inversion formula with imposed stability properties was derived later in [20]. Using the Zernicke polynomials (e.g. see [15]) $R_n{}^l(r)$, he derived the following reconstruction formula

$$f_n(r) = \sum_{l=0}^{\infty} (n + 2l + 1)\, a_n{}^l\, R_n{}^l(r),$$

where the $a_n{}^l$ are the coefficients appearing in the expansion

$$g_n(s) = 2 \sum_{l=0}^{\infty} a_n{}^l \sin\left[(n + 2l + 1)\arccos(s)\right].$$

4.1.2 Fourier slice theorem

The Fourier transform and Radon transform are connected in a simple way. In imaging, this connection is called the Fourier slice theorem or equivalently the

projection-slice theorem. Following the same notation as in the previous section, let us define the one-dimensional Fourier transform of Rf

$$\widehat{Rf}(\rho, \phi) = \int_{-\infty}^{\infty} Rf(s, \phi) \, e^{-2\pi i \rho s} \, ds,$$

and the two-dimensional Fourier transform of f

$$F(u, v) = \int_{-\infty}^{\infty} \int_{-\infty}^{\infty} f(x, y) \, e^{-2\pi i(x\,u + y\,v)} \, dx \, dy. \tag{4.8}$$

According to the Fourier slice theorem, there is a connection between the two-dimensional Fourier transform of the function f and the one-dimensional Fourier transform of the Rf.

Let f be an absolutely integrable function in a domain $D \subset \mathbb{R}^2$. For any real number ρ and any angle ϕ, the Fourier slice theorem states

$$\widehat{Rf}(\rho, \phi) = F(\rho \cos \phi, \rho \sin \phi).$$

For an in-depth treatment of the theorem and its extension to n dimensions see [23].

4.1.3   Filtered backprojection method

Let us recall first the Fourier inversion of equation (4.8) in polar coordinates when f is an absolutely integrable function in a domain $D \subset \mathbb{R}^2$ and F is absolutely integrable

$$f(x, y) = \int_0^{2\pi} \int_0^{\infty} F(\rho \cos \phi, \rho \sin \phi) \, e^{2\pi i \, (x\rho \cos \phi + y\rho \sin \phi)} \, \rho \, d\rho \, d\phi. \tag{4.9}$$

Making use of the Fourier slice theorem, the equation (4.9) and the evenness property of Rf defined previously in the equation (3.1), we can establish the filtered backprojection (FBP) formula that states

$$f(x, y) = \int_0^{\pi} \int_{-\infty}^{\infty} \widehat{Rf}(\rho, \phi) \, e^{2\pi i \rho \, (x \cos \phi + y \sin \phi)} \, |\rho| \, d\rho \, d\phi.$$

The FBP formula can be understood as a two-step process:

1. The first inner integral is a filter applied to the Radon transform Rf. The filter represents a weighting of each projection in the frequency domain.

2. The outer integral is the backprojection of the filtered Radon transform.

To reconstruct the image at every point (x, y), the data is transformed to the frequency domain using one-dimensional Fourier transform, multiplied by the filter in the frequency domain, and then transformed back to the time domain using the one-dimensional inverse Fourier transform. The Radon transform data are referred to as the sinogram due to its characteristic sinusoidal shape. If the reconstruction were done without filtering, the form of the recovered image would be blurred. So in order to avoid artifacts and improve the quality of the reconstructed image, it is necessary to filter the data.

The next step involves a process known as backprojection which takes the filtered data and projects it back along the same lines from where the data was collected. So to compute the function at any given point (x, y), we average the filtered projections over all lines passing through that point. This FBP approach is useful for our discussion of the approximate inversion of the elliptical Radon transform developed in chapter 6.

Numerous other reconstruction schemes have been developed for inverting the Radon transform. For a survey see, e.g., [23, 25, 42]. Notice that all these inversion formulas uniquely determine the unknown function f from its classical Radon transform Rf. Hence, the uniqueness question is well known and answered. The same question when Rf is known only on a subset of the support of f is more complicated but well studied for the classical Radon transform (for more details, see [42]).

4.2 Spherical Radon transform

4.2.1 Uniqueness of reconstruction

Unlike the case of the classical Radon transform, the problem addressing the uniqueness of reconstruction is still not completely understood for the spherical Radon transform. In this section, we first formulate the problem of uniqueness of the spherical Radon transform and then present some of the recent mathematical results on uniqueness in $\mathbb{R}^2$ and $\mathbb{R}^n$ for $n > 2$.

4.2.1.1 Formulation of the problem

Let $f(x)$ be a continuous function on $\mathbb{R}^n$, the spherical Radon transform can be written as

$$Rf(p,r) = \int_{|x-p|=r} f(x)\, ds,$$

where ds is the surface area on the sphere $|x - p| = r$ centered at $p \in \mathbb{R}^n$. Without any restrictions on the set of centers p or radii r, $Rf(p,r)$ depends on $n+1$ variables (one for the radius and n for the center's location). It is clear that the reconstruction of the function $f(x)$ of n variables from $Rf(p,r)$ is an overdetermined problem. It is reasonable to expect that one can still uniquely recover f from Rf after reducing the degrees of freedom of Rf by one. There are many different ways to reduce the dimensions of the Rf, e.g. by considering only the data coming from spheres of a certain fixed radius, spheres passing through a fixed point, spheres tangent to a hyperplane, spheres with centers located on a hypersurface, etc. All of these approaches lead to interesting mathematical problems and various research groups have done extensive amount of work on this subject. One can find good surveys and abundant lists of references to papers dedicated to these topics in [6, 9, 28, 30].

Motivated by several imaging applications described in chapter 2, we restrict the centers p to a set $\Gamma \subset \mathbb{R}^n$ while not imposing any conditions on the radii. So the first question that arises is whether knowing all the values of Rf on the set Γ uniquely determines the function f. Before addressing this problem, let us first define the notion of injectivity sets.

Definition 1. *Suppose Γ is a subset of $\mathbb{R}^n$. The spherical Radon transform is injective on Γ if for any $f \in C_c(\mathbb{R}^n)$, the condition $Rf(p, r) = 0$ for all $r \geq 0$ and for all $p \in \Gamma$ implies $f \equiv 0$. Such subsets Γ are called sets of injectivity for the spherical Radon transform on the class of compactly supported smooth functions.*

Here $C_c(\mathbb{R}^n)$ denotes the space of compactly supported continuous functions on $\mathbb{R}^n$. Using this definition, we can formulate the uniqueness question as follows: Which subsets Γ of $\mathbb{R}^n$ are injectivity sets of the spherical Radon transform?

4.2.1.2   Uniqueness of the circular Radon transform

The problem of describing the sets of injectivity of the circular Radon transform has been investigated intensively due to their connection to nodal sets for eigenfunctions of the Laplacian. The first work concerning non-injectivity sets was made in [37] by V. Lin and A. Pincus who considered the problem in relation to approximation theory. They proved that if Rf is not injective on Γ then Γ is contained in the zero set of a harmonic polynomial.

Their results were used in [6] by M. Agranovsky and T. Quinto who completely characterized the structure of the injectivity sets of a compactly supported function f when Rf is known along circles of all possible radii and centered on a given set. We will state their results but refer the reader to [6] for further details. Let us first introduce the following definition.
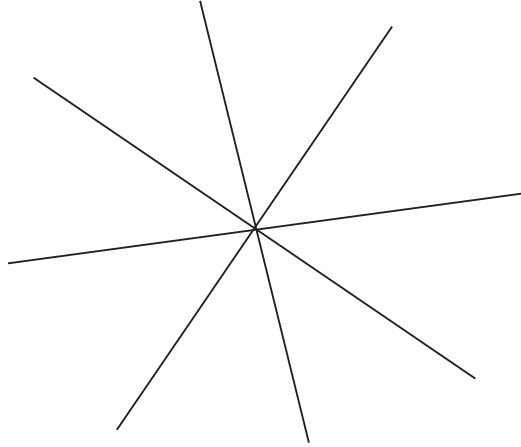
Figure 4.2. $L_k = \{te^{\frac{i\pi k}{N}}\,|-\infty < t < \infty\}$.

Definition 2. *For any positive integer N define $\sum_N$ to be the Coxeter system of N lines $L_0, ..., L_{N-1}$*

$$L_k = \{r\,e^{i\pi k/n}|k = 1, ..., N,\, r \in \mathbb{R}\}.$$

$\sum_N$ are N lines passing through the origin and forming equal angle π/N.

M. Agranovsky and T. Quinto characterized the injectivity sets in $\mathbb{R}^2$ in terms of Coxeter systems of lines.

Theorem 3. *A subset $\Gamma \subset \mathbb{R}^2$ is a set of injectivity for Rf on $\mathbb{R}^2$ if and only if Γ is not contained in any set of the form $Q(\sum_N) \cup Y$ for some N, for some rigid motion Q in the plane and some finite set Y.*

So the only subsets Γ of $\mathbb{R}^2$ which fail to be injectivity sets are either an empty set, a finite set or the union of a finite set and a Coxeter system of lines $\sum_N$. Any rigid motion Q preserves non-injectivity property, so $Q(\sum_N)$ is also a non-injectivity set.

For example in planar geometry, the line is a non-injectivity set, i.e. we can not recover f from the circular Radon transform Rf centered on a line. Indeed, if $f(x)$ is odd with respect to a line L, then if we integrate the function along circles centered on L, the measured data Rf is zero. So clearly the line, which is a subset of the $\sum_N$, is eliminated from the injectivity sets of the circular Radon transform. However, it is well known that functions that are even with respect to a line L can be reconstructed using the circular Radon transform centered on L (see [21]). It is also easy to see from this statement, that the functions supported only on one side of the line can be recovered uniquely (consider an even function which is equal to half of the previous function in the support).

4.2.1.3   Uniqueness of the spherical Radon transform

M. Agranovsky and T. Quinto in [6] conjectured the structure of the injectivity sets for the spherical Radon transform on the class of compactly supported function in higher dimensions.

Conjecture 4. *A set $\Gamma \subset \mathbb{R}^n$ is an injectivity set for the spherical Radon transform on $C_c(\mathbb{R}^n)$, if and only if it is not contained in any set of the form $Q(\sum_N) \cup Y$, where Q is a rigid motion of $\mathbb{R}^n$, $\sum_N$ is the zero set of a non-zero homogeneous harmonic polynomial, and Y is an algebraic subset in $\mathbb{R}^n$ of co-dimension at least 2.*

Unfortunately, the techniques of microlocal analysis and geometric properties of zero sets of harmonic polynomials used to prove the 2-dimensional conjecture, do not work well in dimensions higher than two or when the function is not compactly supported. So no proof of the conjecture is known at this time, as well as little is known about the non-injectivity sets for functions that are not compactly supported. A new alternative method based on a relation between the solutions of the wave equation and the spherical Radon transform has been investigated by M. Agranovsky,

C. Berenstein and P. Kuchment in [2]; D. Finch, S. Patch and Rakesh in [30]; and G. Ambartsoumian and P. Kuchment in [9]. This approach has led to new results promising possible progress to prove the n-dimensional conjecture.

We first mention the theorem in [2] of M. Agranovsky, C. Berenstein and P. Kuchment, who used PDE tools to study the injectivity of the spherical Radon transform when $f \in L^p(\mathbb{R}^n)$ and Rf is known for spheres of all possible radii centered at every point of the boundary of some domain.

Theorem 5. *The boundary Γ of any bounded domain in $\mathbb{R}^n$ is uniqueness set for $f \in L^p(\mathbb{R}^n)$ iff $p \leq \frac{2n}{n-1}$.*

In [30], D. Finch, S. Patch and Rakesh studied this uniqueness problem for smooth f supported in a bounded connected domain, proving the uniqueness of inversion using Rf from spheres centered on any open subset of the boundary of D and all possible radii $D \subset \mathbb{R}^n$.

Theorem 6. *Suppose D is a bounded open subset of $\mathbb{R}^n$, $n \geq 2$, with a smooth boundary S and the closure set $\bar{D}$ is strictly convex. Let Γ be any relatively open subset of S. If f is a smooth function on $\mathbb{R}^n$, supported in $\bar{D}$, and $Rf(p, r) = 0$ for all $p \in \Gamma$ and all $r \in [0, diam\, D]$ then $f \equiv 0$.*

Another result was reported in [9] by G. Ambartsoumian and P. Kuchment who reproved some known theorems using simpler methods and obtained further results on the injectivity of spherical Radon transform. They discovered same strong necessary conditions that any non-injectivity set has to satisfy, regardless of the dimensions of the problem and without requiring finite support of f. The formulation of the full result will require substantial space for extra definitions, so we present here just one corollary of the main theorem, referring the reader to [9] for more details.

Theorem 7. *Let Γ be a relatively open piece of C^1-hypersurface and $f \in C_c(\mathbb{R}^n)$ be such that $Rf(p,r) = 0$ for all $(p,r) \in \Gamma \times \mathbb{R}$. If there is a point $p_0 \in \Gamma$ such that the support of f lies strictly on one side of the tangent plane $T_{p_o}\Gamma$ to Γ at p_0, then $f \equiv 0$.*

Conclusion: We have presented some of the recent mathematical results on the uniqueness of the spherical Radon transform. In the case of compactly supported functions, non-uniqueness sets of the circular Radon transform are completely characterized. However, the uniqueness problem remains unresolved in dimensions higher than two, and even in dimension two it is not resolved for functions that are not compactly supported. Indeed, the problem is much harder to study without compactness of support.

Remark: All three theorems above guarantee the unique inversion of Rf in circular acquisition geometry when Rf is available for all possible radii (complete data). But the uniqueness question when Rf is available for only a part of all possible radii (partial data) is still an open problem. In the case of odd n, D. Finch, S. Patch and Rakesh proved in [30] the uniqueness of inversion from data with spheres centered at every point of the boundary and radii limited to $r < (\operatorname{diam} D)/2$. The proof of the latter result would not extend to even dimensions, since it was based on the solution properties of certain problems related to wave equation, that hold only in odd dimensions. In addition, M. Anastasio et al. showed in [11] that the 3D spherical Radon data for half of all possible radii is sufficient for unique reconstruction of the unknown function supported inside the sphere.

However, to the best of our knowledge no uniqueness result is known for even dimensions when only partial data is available. In our paper [7], we made progress in filling this gap in $\mathbb{R}^2$, by proving uniqueness for the circular Radon transform collected along all circles of radii $r < (\operatorname{diam} D)/2$. We also addressed another open problem of

uniqueness when the support of the unknown function extends outside of the circle. These new results are presented in details in the next chapter.

4.2.2 Reconstruction formulas

Many explicit inversion formulas have been derived from the spherical Radon transform centered on some simple geometries. The first studied geometry was the hyperplane in [14, 21, 26, 44]. As it has been mentioned in the previous section, there is no uniqueness in this case, only even functions can be reconstructed from the spherical Radon transform. Another geometry investigated in [47, 54] was the infinite cylinder in three-dimensional space. We do not provide details about the reconstruction formulas in these geometries as they are not our case of interest.

In this section, we confine our discussion to the spherical geometry as it is the most relevant acquisition to the imaging modalities described in the first chapter. We state some of the known methods to derive explicit inversion formulas from the spherical Radon transform centered on a sphere.

4.2.2.1 Fourier expansion methods

The first approach to tackle the problem of reconstructing a function supported in a disc D from its spherical Radon transform along circles centered on the boundary of D, was described by S. Norton [46] in his study of ultrasonic reflection tomography. He derived an inversion formula based on harmonic decompositions for the measured circular Radon transform and the 2D unknown function. This paper has been an inspiration to many subsequent works.

Throughout this section $f(r, \theta)$ denotes a two-dimensional function supported inside the disc $D(0, R)$, where (r, θ) are polar coordinates measured from the center of that disc, and $R > 0$ is a fixed number. The circular Radon transform Rf along a
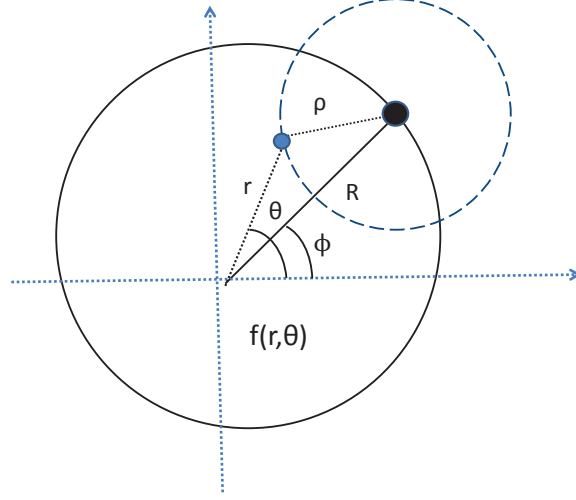
Figure 4.3. Circle geometry $C(\rho, \phi)$.

circle of radius ρ centered at a point with polar coordinates (R, ϕ) (see Figure 4.3) is denoted by

$$g(\rho, \phi) = Rf(\rho, \phi) = \int_{C(\rho,\phi)} f(r, \theta)\, ds. \tag{4.10}$$

Since $f(r, \theta)$ and $g(s, \phi)$ are periodic with respect to the corresponding angular variables θ and ϕ, they can be expanded as Fourier series

$$f(r, \theta) = \sum_{n=-\infty}^{\infty} f_n(r)\, e^{in\theta}, \tag{4.11}$$

$$g(\rho, \phi) = \sum_{n=-\infty}^{\infty} g_n(\rho)\, e^{in\phi}, \tag{4.12}$$

where the Fourier coefficients $f_n(r)$ and $g_n(\rho)$ are computed in (4.4) and (4.5).

The circular Radon transform as expressed by Eq.(4.10), can be written in terms of Dirac delta function

$$g(\rho, \phi) = \int_0^\infty r\, dr \int_0^{2\pi} d\theta\, f(r, \theta)\, \delta[\rho - (r^2 + R^2 - 2rR\, \cos(\phi - \theta))^{1/2}].$$

The solution to the problem is obtained by using the property of Dirac delta function

$$\delta(\beta - \rho) = \rho \int_0^\infty J_0(\beta z) J_0(\rho z) z \, dz,$$

and deriving a relation expressing the n-th Fourier coefficient $f_n(r)$ in terms of the n-th Fourier coefficient $g_n(\rho)$. In other words, the circular Radon transform is diagonalized by passing to the basis of complex exponentials. This is not surprising due to the rotation invariance of $g(\rho, \phi)$ in the circular geometry. As a result the problem breaks down to the following set of one-dimensional integral equations

$$g_n(\rho) = 2\pi\rho \int_0^\infty z J_0(\rho z) J_n(Rz) \mathcal{H}_n\{f_n(r)\} dz, \tag{4.13}$$

where $\mathcal{H}_n$ with $\mathcal{H}_n\{p(r)\}_z = \int_0^\infty p(r) J_n(rz) r dr$ is the n-th order Hankel transform and $J_n(r)$ are the Bessel functions of the first kind.

Using the fact that the Hankel transform is its own inverse, the coefficients $f_n(r)$ can be recovered by the following formula

$$f_n(r) = \mathcal{H}_n \left\{ \frac{1}{J_n(Rz)} \mathcal{H}_0 \left\{ \frac{g_n(\rho)}{2\pi\rho} \right\}_z \right\}_r. \tag{4.14}$$

The function $f(r, \theta)$ can now be reconstructed by inserting the $f_n(r)$ into the angular Fourier series (4.11). Notice this inversion formula requires a division of the Hankel transform by the Bessel functions that have infinitely many zeros. In the numerical implementation, these zeros would create instabilities. So recently, there have been new additions in this approach in [34] to avoid this instability problem by replacing the Bessel functions by Hankel functions $H_n^{(1)}$ which does not have zeros for any real values. Eq. (4.14) becomes

$$f_n(r) = \mathcal{H}_n \left\{ \frac{1}{H_n^{(1)}(Rz)} \int_0^{2R} g_n(\rho) H_0^{(1)}(\rho z) d\rho \right\}. \tag{4.15}$$

In a similar way, S. Norton and M. Linzer in [47] derived an inversion formula for the three-dimensional case involving a series expansion in spherical harmonics.

All these mentioned works assume that the object of interest is entirely surrounded by the circular aperture. They also require a complete knowledge of the circular Radon transforms $g(\rho, \phi)$ for all the values of ρ and ϕ. In fact, to be able to reconstruct the function f at any point (r, θ), all the values of $g(\rho, \phi)$ are essential.

4.2.2.2 Filtered backprojection methods

The filtered backprojection method is the most common technique in image reconstruction that requires the inversion of the spherical Radon transform. It transforms the data to the frequency domain, then filters in order to smooth out the noise, returns to the time domain and then applies a backprojection. The inversion formulas of filtered backprojection type do not involve series but are instead given as integrals. The first exact formulas of this type were proven in [30] by D. Finch, S. Patch and Rakesh in odd dimensions, and then extended recently to even dimensions in [27] by D. Finch, M. Haltmeier and Rakesh.

Let us start with some notations to state the explicit inversion formulas. For any integer $n > 1$, we assume that the unknown function $f(x)$ is supported inside the ball B of radius R in $\mathbb{R}^n$, which is centered at the origin. We also assume that the spherical Radon transform $Rf(p, r) = g(p, r)$ is known for all spheres of radius r centered at the point p on the spherical boundary S_R of the ball.

$$g(p, r) = \int_{|p-x|=r} f(x)\, d\sigma. \tag{4.16}$$

Let $\hat{C}^\infty(S_R \times [0, \infty))$ denote the class of smooth functions $g(p, t)$ which are zero to infinite order in t at $t = 0$. The operator $\mathcal{D}$ is defined as follows

$$\mathcal{D} : \hat{C}^{\infty}(S_R \times [0, \infty)) \quad \to \quad \hat{C}^{\infty}(S_R \times [0, \infty))$$

$$g(p, t) \quad \to \quad \left(\frac{1}{2t} \frac{\partial}{\partial t} \right) g(p, t).$$

It is also convenient to define $\mathcal{N}$

$$\mathcal{N} : C_0^{\infty}(\bar{B}) \quad \to \quad \hat{C}^{\infty}(S_R \times [0, \infty))$$

$$f(p, t) \quad \to \quad t^{n-2} g(p, t),$$

whose L^2-adjoint is $\mathcal{N}^*$, which is given as follows

$$\mathcal{N}^* : \hat{C}^{\infty}(S_R \times [0, \infty)) \quad \to \quad C_0^{\infty}(\mathbb{R}^n)$$

$$F(x) \quad \to \quad \frac{1}{w_{n-1}} \int_{|p|=R} \frac{F(p, |p - x|)}{|p - x|} \, ds,$$

where w_{n-1} surface area of the unit sphere. Since the inversion formulas are different for the odd and even dimensions, we state them separately.

- *Inversion for odd n*

Theorem 8. *If n is odd and $f \in C_0^{\infty}(\bar{B})$ then for all $x \in B$, the following reconstruction formulas hold true*

$$f(x) = \frac{c_n}{R} \triangle_x \left(\mathcal{N}^* t \mathcal{D}^{n-3} t^{n-4} g \right)(p, t),$$

where $\triangle_x$ is the Laplacian with respect to the first variable and

$$c_n = \frac{(-1)^{(n-1)/2} \pi}{2\Gamma(n/2)^2}.$$

In the case $n = 3$, it may be written

$$f(x) = -\frac{1}{2\pi R} \triangle_x \int_{|p|=R} \frac{1}{|x - p|} g(p, |x - p|) ds.$$

The proof of the three-dimensional theorem is based on an explicit computation of the integral. However, the n-dimensional theorems were deduced by the use of spherical harmonic expansions.

- *Inversion for even n*

Theorem 9. *If n is even and $f \in C_0^\infty(\bar{B})$ then for all $x \in B$*

$$f(x) = \frac{2}{c_n R} \int_{|p|=R} \int_0^{2R} \left(\log|t^2 - |x - p|^2| \right) \left((t\mathcal{D}^{n-1} t^{n-1} \partial_t g)(p,t) \right) \, dt \, ds,$$

where

$$c_n = (-1)^{n-2/2} 2 \left[(n-2)/2)! \right] \pi^{n/2}.$$

In the case $n = 2$, it may be written

$$f(x) = \frac{1}{2\pi R} \int_{|p|=R} \int_0^{2R} \log|t^2 - |x - p|^2|(\partial_t \, t \, \partial_t \, g)(p,t) \, dt \, ds. \qquad (4.17)$$

The theorem was proved in [27] using a spherical harmonic expansion and the trace of the solution of the wave equation in even dimensions.

Another interesting inversion formula for the spherical geometry was presented by M. Xu and L. Wang in [54] called the universal backprojection algorithm which offers exact reconstruction for three common geometries: planar, spherical and cylindrical surfaces.

In [35], L. Kunyansky presented an inversion formula for any arbitrary dimensions $n > 1$, similar to the result of M. Xu and L. Wang in [54].

Remark: We have summarized some of the recent mathematical results for the problem of recovering a function from the spherical Radon transform. All presented formulas assume that a complete data set is available, i.e. the values of the spherical Radon transforms $g(p, r)$ are known for all the values of p and r. For example in the equation (4.17), a complete knowledge of $g(p, r)$ is needed to reconstruct the function f at any point x. So how to recover f if the experimental implementation does not provide the complete data set?

The hypothesis that all the values of the spherical Radon transform are known, is not always possible in imaging applications. For example, in some cases, because some regions of the object to be imaged strongly attenuate the signal, only partial data is available. In [12], M. Anastasio and his collaborators showed that using a partial data in Norton's formula [46] ($r \leq (\operatorname{diam} D)/2$) instead of the complete data ($r \leq \operatorname{diam} D$), results in severe image artifacts. Clearly, there is a significant need for a new reconstruction formula using partial data.

In our paper [7], we made progress in filling this gap by deriving new inversion formulas for the circular Radon transform collected along all circles of radii $r \leq r_0$ for $\forall r_0 < (\operatorname{diam} D)/2$. These new results are presented in details in the next chapter.

CHAPTER 5

RECONSTRUCTION FROM PARTIAL DATA OF SRT[1]

After we have shown some of the techniques of reconstructing f using com-
plete data of the spherical Radon transform Rf, we now concentrate on the question
of representing a function by its circular Radon transform with partial data. In
this chapter, we present our new results about the existence and uniqueness of such
representations, and a new inversion formula in the case of the circular acquisition
geometry for both interior and exterior problems. The results are not only interesting
as original mathematical discoveries, but can also be useful for many applications,
e.g. in medical imaging.

5.1 Interior problem

Throughout this section $f(r, \theta)$ denotes an unknown function supported inside
the disc of radius R, where (r, θ) are polar coordinates measured from the center of
that disc, and $R > 0$ is a fixed number. The circular Radon transform of f along a
circle of radius ρ centered at a point with polar coordinates (R, ϕ) (see Figure 5.1) is
denoted by

$$g(\rho, \phi) = Rf(\rho, \phi) = \int_{C(\rho, \phi)} f(r, \theta)\, d\sigma. \tag{5.1}$$

The Fourier series generated by $f(r, \theta)$ and $g(\rho, \phi)$ with respect to corresponding
angular variables are denoted by

$$f(r, \theta) = \sum_{n=-\infty}^{\infty} f_n(r)\, e^{in\theta}, \tag{5.2}$$

$$g(\rho, \phi) = \sum_{n=-\infty}^{\infty} g_n(\rho)\, e^{in\phi}, \tag{5.3}$$

where the Fourier coefficients $f_n(r)$ and $g_n(\rho)$ are computed in (4.4) and (4.5).

---
[1] This chapter is mainly based on the paper [7].
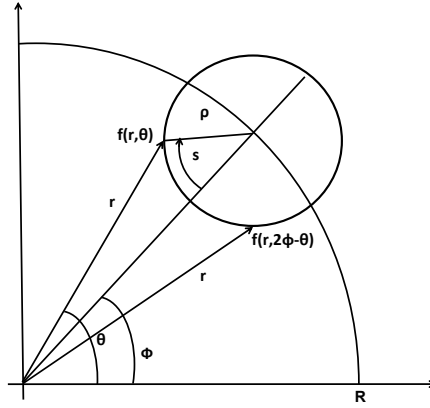
Figure 5.1. Geometric setup of integration along the circle $C(\rho, \phi)$.

We show that the function f can be uniquely recovered from Radon data with only part of all possible radii, and then provide a reconstruction formula.

5.1.1 Uniqueness of reconstruction

Theorem 10. *Let $f(r, \theta)$ be an unknown continuous function supported inside the annulus $A(\varepsilon, R) = \{(r, \theta) : r \in (\varepsilon, R), \theta \in [0, 2\pi]\}$, where $0 < \varepsilon < R$. If $Rf(\rho, \phi)$ is known for $\phi \in [0, 2\pi]$ and $\rho \in [0, R - \varepsilon]$, then $f(r, \theta)$ can be uniquely recovered in $A(\varepsilon, R)$.*

Proof. We use an approach similar to Cormack's inversion of the classical Radon transform [19]. Let us rewrite formula (5.1) by considering the contribution dg to $g(\rho, \phi)$ from two equal elements of arc ds of the circle $C(\rho, \phi)$. If the two elements of the arc are located symmetrically with respect to the polar radius of the center of integration circle (see Figure 5.1), then

$$dg = \sum_{n=-\infty}^{\infty} \left[f_n(r)\, e^{in\theta} + f_n(r)\, e^{in(2\phi-\theta)} \right] ds, \qquad 0 \leq \phi \leq \theta \leq 2\pi$$

so we can write

$$g(\rho, \phi) = \int_{C^+(\rho,\phi)} \sum_{n=-\infty}^{\infty} [f_n(r)\, e^{in\theta} + f_n(r)\, e^{in(2\phi-\theta)}]\, ds, \quad 0 \le \phi \le \theta \le 2\pi,$$

where $C^+(\rho, \phi)$ denotes half of the circle $C(\rho, \phi)$ corresponding to $\theta \ge \phi$. Notice that $e^{in\theta} + e^{in(2\phi-\theta)} = 2\, e^{in\phi} \cos[n(\theta - \phi)]$, and $s = \rho \arccos\left(\frac{\rho^2 + R^2 - r^2}{2\rho R}\right)$, hence

$$ds = \frac{r\, dr}{R\sqrt{1 - \left(\frac{\rho^2 + R^2 - r^2}{2\rho R}\right)^2}}.$$

Exchanging the order of summation and integration and using these relations we get

$$g(\rho, \phi) = \sum_{n=-\infty}^{\infty} 2\, e^{in\phi} \int_{R-\rho}^{R} \frac{f_n(r)\, r \cos[n(\theta - \phi)]}{R\sqrt{1 - \left(\frac{\rho^2 + R^2 - r^2}{2\rho R}\right)^2}}\, dr.$$

Applying $\theta - \phi = \arccos\left(\frac{r^2 + R^2 - \rho^2}{2rR}\right)$, we obtain

$$g(\rho, \phi) = \sum_{n=-\infty}^{\infty} 2\, e^{in\phi} \int_{R-\rho}^{R} \frac{f_n(r)\, r \cos\left[n \arccos\left(\frac{r^2 + R^2 - \rho^2}{2rR}\right)\right]}{R\sqrt{1 - \left(\frac{\rho^2 + R^2 - r^2}{2\rho R}\right)^2}}\, dr. \tag{5.4}$$

Comparing equations (5.3) and (5.4) it is easy to notice that by passing to the basis of complex exponentials we diagonalized the circular Radon transform, i.e. the n-th Fourier coefficient of g depends only on n-th Fourier coefficient of f. This is not surprising, due to rotation invariance property of Rf in the circular geometry. As a result our problem breaks down to the following set of one-dimensional integral equations

$$g_n(\rho) = 2 \int_{R-\rho}^{R} \frac{f_n(r)\, r\, T_{|n|}\left(\frac{r^2 + R^2 - \rho^2}{2rR}\right)}{R\sqrt{1 - \left(\frac{\rho^2 + R^2 - r^2}{2\rho R}\right)^2}}\, dr, \tag{5.5}$$

where $T_k(x)$ is the k-th order Chebyshev polynomial of the first kind (e.g. see [50]). Let us make a change of variables in the integral (5.5) by setting $u = R - r$. Then equation (5.5) becomes

$$g_n(\rho) = \int_0^{\rho} \frac{f_n(R-u)\, 4\rho\, (R-u)\, T_{|n|}\left[\frac{(R-u)^2 + R^2 - \rho^2}{2R\,(R-u)}\right]}{\sqrt{\rho - u}\sqrt{(u+\rho)(2R + \rho - u)(2R - \rho - u)}}\, du, \tag{5.6}$$

which can be rewritten as

$$g_n(\rho) = \int_0^\rho \frac{F_n(u)\, K_n(\rho, u)}{\sqrt{\rho - u}}\, du, \tag{5.7}$$

where

$$F_n(u) = f_n(R - u), \tag{5.8}$$

$$K_n(\rho, u) = \frac{4\rho\,(R - u)\, T_{|n|}\left[\frac{(R-u)^2 + R^2 - \rho^2}{2R(R-u)}\right]}{\sqrt{(u + \rho)(2R + \rho - u)(2R - \rho - u)}}. \tag{5.9}$$

Equation (5.7) is a Volterra integral equation of the first kind with weakly singular kernel (e.g. see [49, 51]). Indeed, due to the assumptions on the support of f we know, that $F_n(u) \equiv 0$ for u close to R or 0. Therefore from formula (5.9) and the properties of Chebyshev polynomials, it follows that the kernel $K_n(\rho, u)$ is continuous in its arguments (and hence bounded) along with the first order partial derivatives on the support of F_n. To remove the singularity in the kernel of equation(5.7), we apply the standard method of kernel transformation [53]. Multiplying both sides of equation (5.7) by $\dfrac{1}{\sqrt{t - \rho}}\, d\rho$ and integrating from 0 to t we get

$$\int_0^t \frac{g_n(\rho)}{\sqrt{t - \rho}}\, d\rho = \int_0^t \int_0^\rho \frac{F_n(u) K_n(\rho, u)}{\sqrt{\rho - u}\sqrt{t - \rho}}\, du\, d\rho, \quad t > 0.$$

Changing the order of integration, we obtain

$$\int_0^t \frac{g_n(\rho)}{\sqrt{t - \rho}}\, d\rho = \int_0^t F_n(u)\, Q_n(t, u)\, du, \tag{5.10}$$

where

$$Q_n(t, u) = \int_u^t \frac{K_n(\rho, u)}{\sqrt{\rho - u}\sqrt{t - \rho}}\, d\rho.$$

The advantage of equation (5.10) in comparison to equation (5.7) is that the modified kernel $Q_n(t, u)$ is finite. Indeed, making a change of variables $\rho = u + (t - u)\, l, 0 \leq l \leq 1$ in the last integral, we get

$$Q_n(t, u) = \int_0^1 \frac{K_n(u + (t - u)\, l, u)}{\sqrt{l}\,\sqrt{1 - l}}\, dl. \tag{5.11}$$

Since K_n is bounded (say $|K_n| < M$), we obtain

$$|Q_n(t,u)| < M \int_0^1 \frac{dl}{\sqrt{l}\,\sqrt{1-l}} = M\pi.$$

In addition $Q_n(t,t) = \pi K_n(t,t) = \pi \sqrt{\frac{2t\,(R-t)}{R}} \neq 0$ on the support of F_n. Now we can easily modify equation (5.10) to a Volterra equation of second kind. Differentiating equation (5.10) with respect to t we get

$$\frac{d}{dt} \int_0^t \frac{g_n(\rho)}{\sqrt{t-\rho}}\,d\rho = \pi F_n(t)\,K_n(t,t) + \int_0^t F_n(u) \left[\frac{\partial}{\partial t} \int_u^t \frac{K_n(\rho,u)}{\sqrt{\rho-u}\sqrt{t-\rho}}\,d\rho \right] du.$$

Dividing both sides of the last equation by $\pi K_n(t,t)$ and denoting

$$G_n(t) = \frac{1}{\pi K_n(t,t)} \frac{d}{dt} \int_0^t \frac{g_n(\rho)}{\sqrt{t-\rho}}\,d\rho, \tag{5.12}$$

and

$$L_n(t,u) = \frac{1}{\pi K_n(t,t)} \frac{\partial}{\partial t} \int_u^t \frac{K_n(\rho,u)}{\sqrt{\rho-u}\sqrt{t-\rho}}\,d\rho. \tag{5.13}$$

We finally obtain a Volterra equation of second kind

$$G_n(t) = F_n(t) + \int_0^t F_n(u)\,L_n(t,u)\,du, \tag{5.14}$$

where the kernel $L_n(t,u)$ is continuous on the support of F_n. To see the continuity of L_n one can make a change of variables in equation (5.13)

$$\rho = t\cos^2 \beta + u\sin^2 \beta, \quad \beta \in [0, \pi/2],$$

and express L_n as

$$L_n(t,u) = \frac{2}{\pi K_n(t,t)} \frac{\partial}{\partial t} \int_0^{\pi/2} K_n(t\cos^2 \beta + u\sin^2 \beta, u)\,d\beta.$$

The Volterra equation of the second kind (5.14) has a unique solution, which finishes the proof of the theorem. $\square$
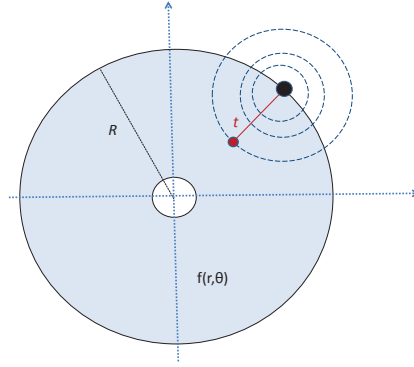
Figure 5.2. The interior problem.

5.1.2 Reconstruction formulas

Using the Picard process of successive approximations (e.g. see [51]) for the solution of Volterra equations of second kind one can immediately obtain the following

Corollary 11. *An exact solution of equation (5.14) is given by the formula*

$$F_n(t) = G_n(t) + \int_0^t H_n(t, u) \, G_n(u) \, du, \tag{5.15}$$

where the resolvent kernel $H_n(t, u)$ is given by the series of iterated kernels

$$H_n(t, u) = \sum_{i=1}^{\infty} (-1)^i L_{n,i}(t, u), \tag{5.16}$$

defined by

$$L_{n,1}(t, u) = L_n(t, u), \tag{5.17}$$

and

$$L_{n,i}(t, u) = \int_u^t L_{n,1}(t, x) \, L_{n,i-1}(x, u) \, dx, \quad i \geq 2. \tag{5.18}$$

This corollary (with notations defined in formulas (5.8), (5.9), (5.12), (5.13)) provides a new exact formula for inversion of the circular Radon transform in circular acquisition geometry. Its advantage compared to all the other known exact inversion formulas is the fact that only part of the Rf data is used. Notice that to reconstruct the function $f(r, \theta)$ in any subset Ω of the disc of its support $D(0, R)$, the inversion

formula in Corollary 11 requires the knowledge of $Rf(\rho, \phi)$ only for $\rho < R - R_0$, where $R_0 = \inf\{|x|, \ x \in \Omega\}$. In medical imaging reducing the radial data redundancy can be essential for increasing the depth and reducing the time of imaging.

We can also remark that the resolvent kernel $H_n(t, u)$ is the same for any functions f and g. Hence in practice one needs to compute it with the desired accuracy only once, and then it can be used with any data set.

In Theorem 10, we require f to be continuous, which guarantees the convergence of the Fourier series (5.2) and (5.3) almost everywhere. If one needs to ensure convergence everywhere, then some additional conditions on f (e.g. bounded variation) should be added in all the theorems.

5.2 Exterior problem

Let us now consider an exterior problem in the circular acquisition geometry, i.e. the Radon data is still collected along circles centered on a circle of radius R, however the unknown function f is supported outside of the disc $D(0, R)$.

Theorem 12. *Let $f(r, \theta)$ be an unknown continuous function supported inside the annulus $A(R, 3R) = \{(r, \theta) : r \in (R, 3R), \ \theta \in [0, 2\pi]\}$. If $Rf(\rho, \phi)$ is known for $\phi \in [0, 2\pi]$ and $\rho \in [0, R_1]$, where $0 < R_1 < 2R$ then $f(r, \theta)$ can be uniquely recovered in $A(R, \ R + R_1)$.*

Proof.

The argument of the proof of the previous theorem repeats here with minimal changes. The condition $0 < R_1 < 2R$ guarantees that all integration circles $C(\rho, \phi)$ intersect the boundary of the disc $D(0, R)$. Hence equation (5.4) in this case becomes

$$g(\rho, \phi) = \sum_{n=-\infty}^{\infty} 2\, e^{in\phi} \int_R^{R+\rho} \frac{f_n(r)\, r \cos\left[n \arccos\left(\frac{r^2 + R^2 - \rho^2}{2rR}\right)\right]}{R \sqrt{1 - \left(\frac{\rho^2 + R^2 - r^2}{2\rho R}\right)^2}}\, dr. \tag{5.19}$$
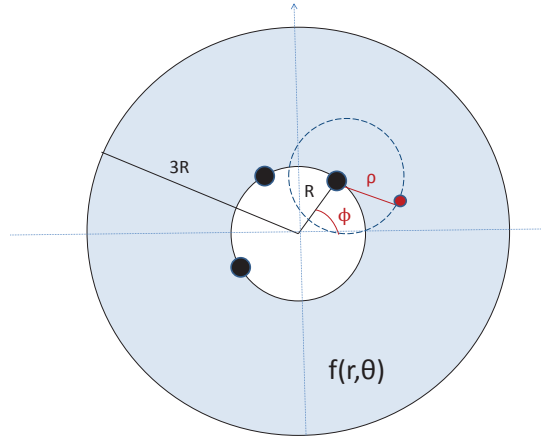
Figure 5.3. The exterior problem.

Then in a similar way, we have

$$g_n(\rho) = 2 \int_R^{R+\rho} \frac{f_n(r) \; r \; T_{|n|}\left(\frac{r^2+R^2-\rho^2}{2rR}\right)}{R \sqrt{1 - \left(\frac{\rho^2+R^2-r^2}{2\rho R}\right)^2}} \; dr, \tag{5.20}$$

Now making a change of variables $u = r - R$ in the last expression we get

$$g_n(\rho) = \int_0^\rho \frac{f_n(R+u) \, 4\rho \, (R+u) \, T_{|n|}\left[\frac{(R+u)^2+R^2-\rho^2}{2R\,(R+u)}\right]}{\sqrt{\rho - u}\sqrt{(u+\rho)(2R+u+\rho)(2R+u-\rho)}} \; du. \tag{5.21}$$

which can be rewritten as

$$g_n(\rho) = \int_0^\rho \frac{F_n(u) \, K_n(\rho, u)}{\sqrt{\rho - u}} \; du, \tag{5.22}$$

where

$$F_n(u) = f_n(R+u), \tag{5.23}$$

$$K_n(\rho, u) = \frac{4\rho \, (R+u) \, T_{|n|}\left[\frac{(R+u)^2+R^2-\rho^2}{2R\,(R+u)}\right]}{\sqrt{(u+\rho)(2R+u+\rho)(2R+u-\rho)}}. \tag{5.24}$$

Notice, that if one would allow $\rho > 2R$, then $K_n(\rho, u)$ would become unbounded due to the last multiplier in the denominator. This shows that $3R$ is an accurate upper limit for the outer radius of the annulus in the hypothesis of the theorem.

In analogy with the proof of the previous theorem we get

$$K_n(t,t) = \sqrt{\frac{2t\,(R+t)}{R}} \neq 0.$$

All the other steps literally repeat the proof of Theorem 10.

5.3 Special case

It is easy to note that in some special cases one can combine the results of the previous two theorems to reconstruct a function whose support is located both inside and outside of the circular path $C(R)$ of data acquisition. For example

Theorem 13. *Let f be an unknown continuous function supported inside the disc $D(0, 2R)$. Assume also that $f \equiv 0$ in some neighborhood of the circle $C(R)$, and all its Fourier coefficients are even (or odd) with respect to $C(R)$, i.e. $f_n(R + u) = f_n(R - u)$ (or $f_n(R + u) = -f_n(R - u)$) for $\forall u \in [0, R]$. If $Rf(\rho, \phi)$ is known for $\phi \in [0, 2\pi]$ and $\rho \in [0, R_1]$, where $0 < R_1 < R$ then $f(r, \theta)$ can be uniquely recovered in $A(R - R_1, R + R_1)$.*

Proof. Combining the two previous results, we obtain a Volterra integral equation of the first kind

$$g_n(\rho) = \int_0^\rho \frac{F_n(u) K_n(\rho, u)}{\sqrt{\rho - u}} \, du, \tag{5.25}$$

where

$$F_n(u) = f_n(R + u), \tag{5.26}$$

and

$$K_n(\rho, u) = \tag{5.27}$$

$$\frac{4\rho}{\sqrt{u+\rho}} \left\{ \frac{(R+u)\, T_{|n|}\left[\frac{(R+u)^2+R^2-\rho^2}{2R\,(R+u)}\right]}{\sqrt{(2R+u+\rho)(2R+u-\rho)}} \pm \frac{(R-u)\, T_{|n|}\left[\frac{(R-u)^2+R^2-\rho^2}{2R\,(R-u)}\right]}{\sqrt{(2R+\rho-u)(2R-\rho-u)}} \right\}.$$

The rest of the proof is carried out along the same lines as before.

It is interesting to note that the circular Radon transform in the linear acquisition geometry can be uniquely inverted on the class of continuous functions that are even with respect to the linear path of the data acquisition. At the same time all odd functions are mapped to zero by that transform. In our case of circular acquisition geometry, the circular Radon transform can be uniquely inverted on classes of functions with Fourier coefficients that are even with respect to the circular path of data acquisition, as well as with the ones that are odd.

Conclusion: The purpose of this chapter has been to present our new mathematical results on uniqueness and recovery of the image function from radially partial data. To our knowledge, this is the first work to explicitly formulate such inversion formulas in the case of the circular acquisition geometry for both interior and exterior problems. The numerical implementation of these formulas is an important topic for future investigation.

The results are not only interesting as original mathematical discoveries, but can also be useful for applications, e.g. in medical imaging. While it is well established that acoustic tomography in its various forms is a classic example of spherical Radon-based imaging *inside* a spherical/circular (3D/2D) aperture, the case of imaging *outside* a spherical aperture is less described biomedically. Two biomedical imaging methods can currently be modeled in the time domain through spherical transforms of a function exterior to the aperture: transrectal ultrasound (TRUS) [48] and intravascular ultrasound (IVUS) [17]. In both TRUS (Figure 5.5) and IVUS (Figure 5.4), a ultrasound array arranged on the surface of a cylinder is introduced
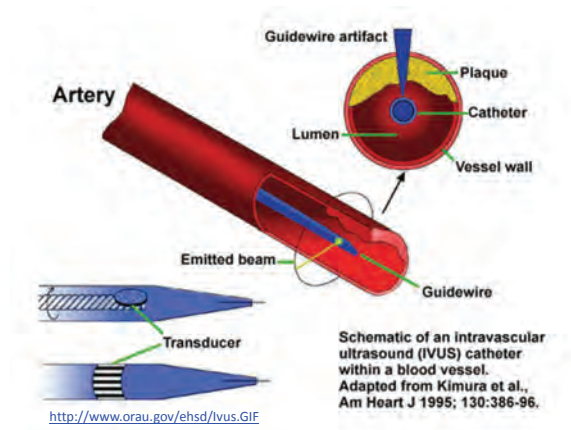
Figure 5.4. Intravascular ultrasound.
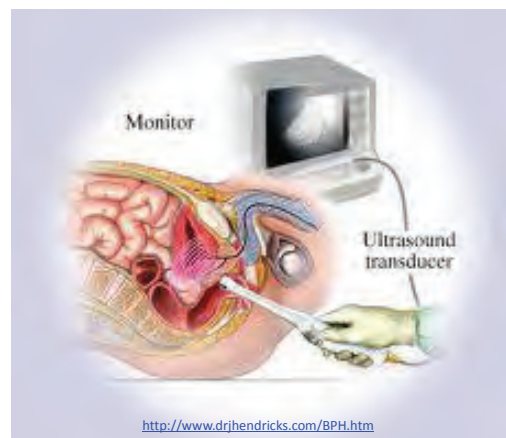
Figure 5.5. Transrectal ultrasound.

into the body with the goal of producing a transverse or axial image. In TRUS, the typical application is imaging of the male prostate, while IVUS is a higher resolution ultrasound technique typically used to evaluate plaques in blood vessels. A less natural setup where the support of the unknown function is located on both sides of the data acquisition path may not be relevant to medical imaging, however it can be applicable in radar and sonar imaging.

CHAPTER 6

APPROXIMATE INVERSION OF ERT: NUMERICAL RESULTS

In circular acquisition geometry, we presented several exact inversion formulas to recover an unknown function from its circular Radon transform. That setup corresponds to the mathematical model of ultrasound reflection tomography in monostatic regime. As it was mentioned before, in bistatic regime the corresponding mathematical model is based on the elliptical Radon transform. Although, S. Mensah and E. Franceschini investigated the inversion of the elliptical Radon transform in [39, 40], this case is still not completely understood. To the best of our knowledge no exact inversion formula is known for the reconstruction from elliptical Radon transform in the circular aperture. Instead, many authors resort to approximate inversion algorithms, such as the recent publication [52] and the work done by T. Quinto and his student H. Levinson to develop novel local reconstruction methods for bistatic radar and ultrasound imaging [36].

In this chapter, we describe an approximate inversion of the elliptical Radon transform when the source and the receiver (the foci of the integration ellipse) are rotating around the origin at a fixed distance from each other, as illustrated in Figure 6.1. We demonstrate the efficiency of the suggested algorithm by presenting a computational implementation of the method on a numerical phantom. We explain how to generate a sample image, collect its integrals over a family of ellipses and then derive a filtered backprojection (FBP) algorithm to reconstruct important features (e.g. boundaries) of the original image.
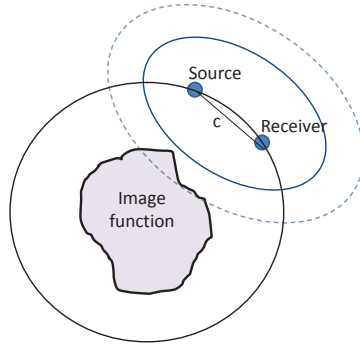
Figure 6.1. Circular acquisition geometry.

6.1 Reconstruction algorithm

Let C designate the circle centered at the origin $(0,0)$ and of radius R. We consider the case of circular acquisition geometry where the source and the receiver are rotating on the circle C. We also assume that the distance c between the source and the receiver is constant (see Figure 6.1). We parameterize the source and the receiver location by the angle ϕ, where $\phi \in [0, 2\pi)$ is the polar angle of the midpoint (cx, cy) measured from the x-axis. For simplicity, we assume that the centers (cx, cy) are rotating on the unit circle. The Figure 6.2 illustrates the circular acquisition geometry and the center's location at a rotation angle ϕ.

To generate the data, we create a sample image called a phantom. Then we compute its integrals over family of ellipses with foci at the source and the receiver locations. The collected integrals are the values of elliptical Radon transform Rf that we use later in the FBP algorithm to reconstruct the features of the original phantom. Now let us look at each of these steps in a little more detail.
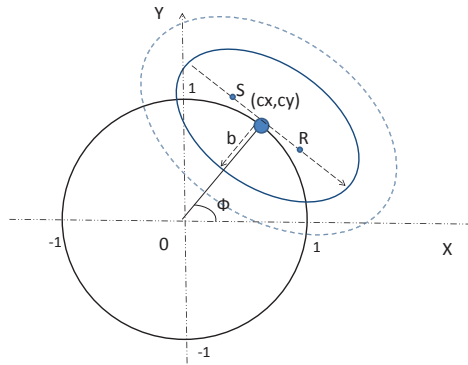
Figure 6.2. Geometric setup of integration.
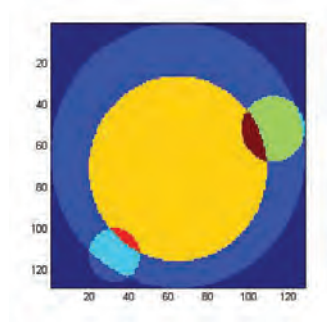
Figure 6.3. Phantom image.

6.1.1 Generation of the phantom image

Numerically, we consider the grid that specifies a pixelated representation of [-1,1] × [-1,1]. The phantom images that we consider are represented by sums of indicator functions of simple objects, like circles and squares. To determine whether a particular pixel lies in the interior of a circle or a square, we look at the center of the pixel. If the center of the pixel lies within a circle/square then we attribute the intensity of the circle/square to the pixel's value. If a pixel is not part of any
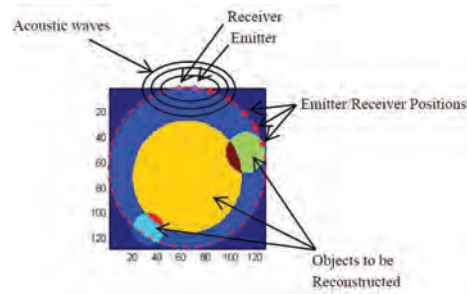
Figure 6.4. Projection data.

circles/squares, its value is 1. In other words, the intensity values of all the pixels in the unit circle define the function $f(x, y)$ as follows:

$$f(x, y) = \begin{cases} I & \text{the center of the pixel inside some of the circles/squares,} \\ 1 & \text{the center of the pixel outside all circles/squares.} \end{cases}$$

where I is equal to the sum of the additive intensity values of all circles/squares that the pixel is a part of.

6.1.2 Computation of the projection data

Once we create the phantom, we need to generate the projection data which is the integrals of the phantom over family of ellipses. As defined in the introduction, we specify the position of the integration ellipse $E(b, \phi)$ by the angle ϕ which is the polar angle of the center of the ellipse (cx, cy) and the semi-minor axis b. Because in practical applications the data is sampled at a finite set of points on the unit circle, we discretize the problem by considering only a finite number of angles ϕ and a finite number of samples of the semi-minor axis b. So we uniformly discretize the data
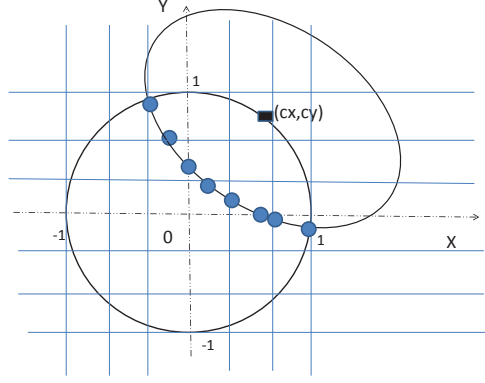
Figure 6.5. Intersection points of an ellipse with the grid.

$[0, 2] \times [0, 2\pi]$ of b and ϕ to N_b and N_ϕ points, respectively. At each point (b^k, ϕ^j), we compute the value of the elliptical Radon transform $Rf(b^k, \phi^j)$:

$$Rf(b^k, \phi^j) := Rf^{k,j} \quad (k, j) \in \{0, ..., N_b\} \times \{0, ..., N_\phi\}.$$

Our appraoch for approximating the integral of the intensity function along any given ellipse $E(b^k, \phi^j)$ is to measure the distance between the neighboring intersection points of the ellipse with vertical and horizontal grid lines and then multiply it by the intensity of the pixel where the points are located.

- *Step 1*

Using $N \times N$ grid that represents [-1,1] $\times$ [-1,1], we compute the intersections of a given ellipse $E(b^k, \phi^j)$ with all vertical and horizontal grid lines located in the unit circle (Figure 6.5).

- *Step 2*

Then by applying the equation (6.1), we estimate the polar angle α between the vector v (connecting the intersection point and (cx, cy)) and the unit vector $\hat{i}$ of the x-axis (Figure 6.6).

$$\alpha = \pm \arccos \left(\frac{v \cdot \hat{i}}{\|v\| \|\hat{i}\|} \right). \tag{6.1}$$
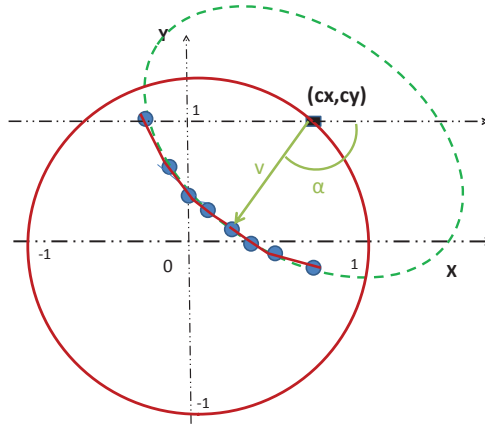
Figure 6.6. The vector v and the angle α.

A major advantage of computing the values of α for the forward problem is that now one can sort the intersection points into the order in which they occur along the ellipse clockwise starting at the west pole. Then, we can easily measure the distance between any consecutive points (see Figure 6.6).

- *Step 3*

Once we measure the distance between any two intersection points, we multiply it by the intensity of the pixel where the points are located. The obtained value is the approximation of the integral of the intensity function along the arc joining these points. This operation is repeated for each pair of intersection points and the resulting values are summed to form an approximate integral of the phantom along the ellipse $E(b^k, \phi^j)$.

We repeat the same process for all the ellipses $E(b^k, \phi^j)$ with $(k, j) \in \{0, ..., N_b\} \times \{0, ..., N_\phi\}$. The result is the discrete value of the elliptical Radon transform Rf that we will use in the FBP algorithm to reconstruct the phantom.

6.1.3   Reconstruction of the phantom image

In the following reconstruction approach, we simply use an approximate FBP algorithm similar to the reconstruction algorithm for the classical Radon transform described in chapter 4. The FBP algorithm involves two steps: (1) each of the projections in the Radon transform is filtered then (2) backprojected to reconstruct the original image.

- *Step 1*

Here we implement a similar procedure for the elliptical Radon transform using the coordinates (b, ϕ) that are analogs of (ρ, ϕ) in the classical Radon transform. Let us recall the filter F defined in the equation (4.9) and represented as follows:

$$Ff(w) = \int_{-\infty}^{\infty} \hat{f}(b) \, e^{ibw} \, |b| \, db. \tag{6.2}$$

This equation represents a filtering operation that can be expressed as a composition of two simpler operations: differentiation and the Hilbert transform. In fact, the Fourier transform of the derivative of the function f is equal to the Fourier transform of f multiplied by ib

$$\widehat{\partial_t f(b)} = (i\,b) \, \hat{g}(b).$$

So to use differentiation and account for the difference between b and $|b|$, we define another operator called the Hilbert transform

$$Hf(x) = \frac{1}{\pi} \int_{-\infty}^{\infty} \frac{f(y)}{x - y} \, dy.$$

This implies that

$$\widehat{Hf(w)} = (-i\,\mathrm{sgn}(w)) \, \hat{f}(w),$$

where

$$\text{sgn}(w) = \begin{cases} 1 & \text{if } w > 0, \\ 0 & \text{if } w = 0, \\ -1 & \text{if } w < 0. \end{cases}$$

By the above equation (6.2), the filtering operation consists of differentiating the function with respect to the semi-minor axis b and then applying the Hilbert transform.

- *Step 2*

The next main reconstruction step involves a process known as backprojection which takes the data from the filtered projections and projects it back along the same ellipses from where the data was collected. So to compute the function at any given point (x, y) in the unit circle, we average the filtered data over all ellipses passing through that point.

$$f(x, y) = \int_0^{2\pi} F(b(\phi), \phi) \, d\phi,$$

This equation adds the resulting filtered projections $F(b, \phi)$ for different angles ϕ to form the estimate of $f(x, y)$. A common discrete approximation to the integral is obtained by:

$$f(x_n, y_n) = \triangle\phi \sum_{m=0}^{N_\phi} F(b(\phi_m), \phi_m),$$

where $\triangle\phi = \frac{2\pi}{N_\phi}$. N_ϕ is the number of angles ϕ for which the projections $Rf(b, \phi)$ are known. It should be noted here that the value of $b(\phi_m)$ may not correspond exactly to a value of m for the filtered projections that we calculated in the previous step. In order to be able to compute $f(x_n, y_n)$ one must then interpolate $b(\phi_m)$.

To implement the algorithm, we sampled the filter and discretized the backprojection operation. The important steps of the approximate FBP are outlined below:

1. Perform the FFT of the projection data for each angle ϕ.

2. Multiply the result with response function in the frequency domain.

3. Perform the IFFT of the result. This provides us the filtered projections in the discrete domain at the various angles ϕ.

4. Sum the filtered projections. The result $f_{FBP}(x,y)$ is an approximation of $f(x,y)$.

6.2   Numerical results

In this section, we present some numerical results of our inversion algorithm for different phantoms to demonstrate its performance. The data is collected from detectors located on the unit circle. Therefore, the region of reconstruction is the unit circle centered at the origin.

In a recent work [8], the authors studied microlocal properties of the ERT in the circular acquisition geometry, and showed that the composition of the ERT with its adjoint (the backprojection operator) is an elliptic pseudo-differential operator. This means that the approximate inversion algorithm based on the backprojection correctly reconstructs the singularities of the object and does not add any additional singularities. Our numerical experiments below validate this result, and present an effective implementation of the technique. Similar algorithms have been recently by other authors, including [36], and [52].

In the results in Figure 6.7, the resolution is 64×64. The angles ϕ of the center locations were uniformly discretized to $N_\phi = 64$ points between 0 and 2π. The semi-minor axis of the integration ellipses were uniformly discretized to $N_b = 64$ points between 0 and 2.
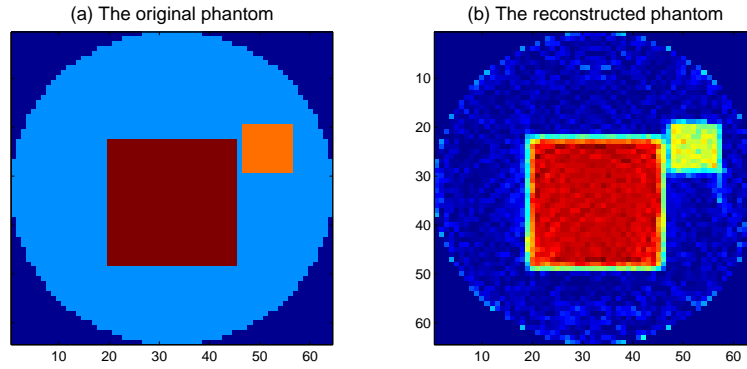
Figure 6.7. Numerical results for 2 squares using $N = 64$.
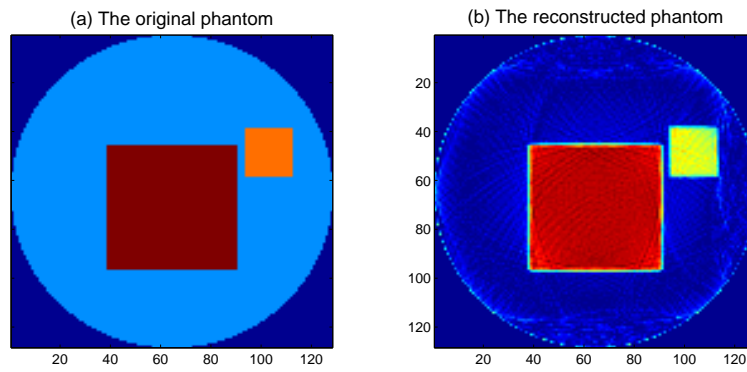
Figure 6.8. Numerical results for 2 squares using $N = 128$.

Next, we increase the number of discretization. We present new set of results with resolution 128×128. As one might expect, we achieve a better reconstruction when we decrease the sampling interval (see Figure 6.8). Additionally, the noisy images in Figure 6.7 appear to be smoothed as compared to the Figure 6.8.

We tested the algorithm on a phantom containing 3 circles (Figure 6.10), the parameters of which are given in Table 6.1. We enumerate the circles from 1 to 3 starting with the circle with highest center.
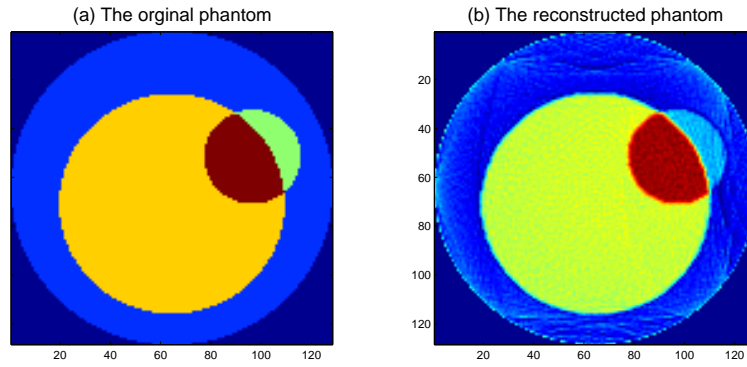
Figure 6.9. Numerical results for a phantom with 2 circles.

Table 6.1. Parameters for the Fig. 6.10

Circle	Coordinates of the center (x, y)	radius	intensity
1	(0.6,0.4)	0.2	2
2	(0.0,-0.1)	0.5	3
3	(-0.5,-0.5)	0.1	1

We tested the algorithm on a phantom containing 3 squares (Figure 6.11), the parameters of which are given in Table 6.2. We enumerate the squares from 1 to 3 starting with the square with highest center.

Table 6.2. Parameters for the Fig. 6.11

Square	Coordinates of the center (x, y)	length	intensity
1	(0.4,0.5)	0.2	1
2	(0.6,0.25)	0.3	2
3	(0.0,-0.1)	0.8	3

(a) The original phantom

(b) The reconstructed phantom
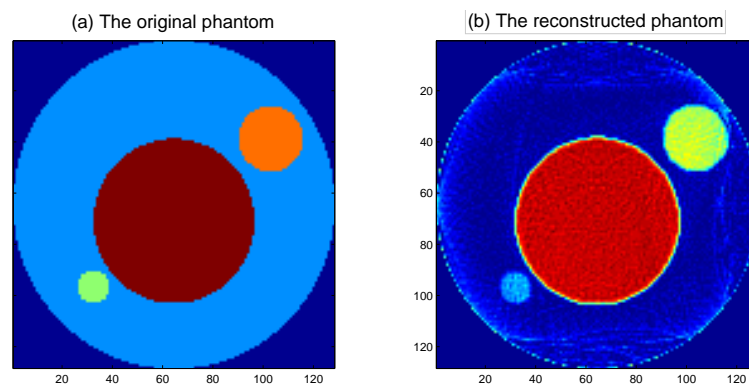
Figure 6.10. Numerical results for a phantom with 3 circles.

(a) The original phantom

(b) The reconstructed phantom
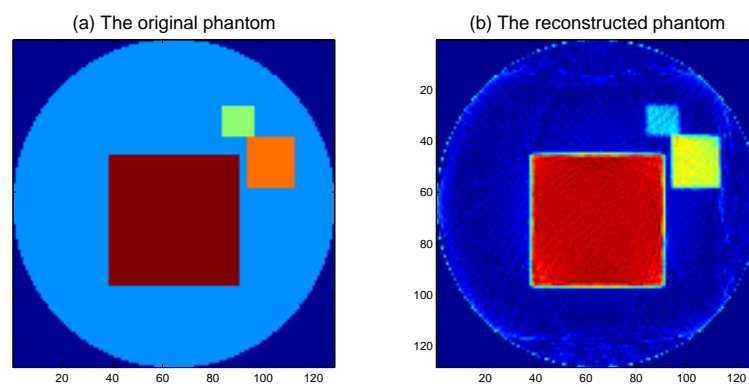
Figure 6.11. Numerical results for a phantom with 3 squares.

CHAPTER 7

DIRECTIONS FOR FURTHER WORK

The new mathematical results presented in this dissertation have the potential to be generalized to higher dimensions using spherical harmonics and Gegenbauer polynomials [1], similarly to the generalization of Cormack's original inversion formula (e.g. see [22, 41]). In addition, possible future work can be done to extend our approach to other transforms of Radon type e.g. the elliptical Radon transform.

Another perspective for future work is to derive an accurate and efficient numerical implementation of our new inversion formulas for both interior and exterior problems when the Radon transform is known for only a part of all possible radii.

The algorithm described in chapter 6 used an approximate inversion formula to reconstruct the image function from its integrals along ellipses rotating around the origin. A direction for future work is to derive an exact inversion formula for the elliptical Radon transform in 2D and 3D cases, and then implement it numerically. Also the uniqueness problem for the elliptical Radon transform still remains unresolved in the case of circular and spherical aperture. These open problems may be relevant to several imaging modalities and practical applications working in the near field zone or with bistatic measurements.

CHAPTER 8

CONCLUSION

In the last decade, there has been a substantial spike of interest towards the problem of reconstructing a function from its circular Radon transform mainly due to its connection with some mathematical models of advanced imaging modalities. In circular acquisition geometry there are various inversion formulas when the circular Radon transform Rf is known for circles of all possible radii. However, to the best of our knowledge no exact formula is known for the case when Rf is available for only a part of all possible radii, or when the support of the function f is outside the circle.

In this dissertation, we presented our new results about the existence and uniqueness of the representation of a function by its circular Radon transform with radially partial data. A new inversion formula is described in the case of the circular acquisition geometry for both interior and exterior problems when the Radon transform is known for only a part of all possible radii. We also investigated a reconstruction algorithm applicable in the case of elliptical Radon transform based on an approximate backprojection formula.

The results are not only interesting as original mathematical discoveries, but can also open new frontiers in the field of imaging.

REFERENCES

[1] M. Abramowitz and I. A. Stegun, *Handbook of Mathematical Functions with Formulas, Graphs, and Mathematical Tables*, Dover Publications, New York, 1972.

[2] M. L. Agranovsky, C. A. Berenstein and P. Kuchment, "Approximation by spherical waves in L^p-spaces," *J. Geom. Anal.*, **6** (1996), 365–383.

[3] M. L. Agranovsky, P. Kuchment and L. Kunyansky, "On reconstruction formulas and algorithms for the thermoacoustic and photoacoustic tomography," in *Photoacoustic imaging and spectroscopy, ed. L.-H. Wang*, CRC Press, 2009.

[4] M. L. Agranovsky, P. Kuchment and E. T. Quinto, "Range descriptions for the spherical mean Radon transform," *J. Funct. Anal.*, **248** (2007), 344-386.

[5] M. L. Agranovsky and P. Kuchment, "Uniquness of reconstruction and an inversion procedure for thermoacoustic and photoacoustic tomography with variable sound speed," *Inverse Problems*, **23** (2007), 2102-2007.

[6] M. L. Agranovsky and E. T. Quinto, "Injectivity sets for the Radon transform over circles and complete systems of radial functions," *J. Funct. Anal.*, **139** (1996), 383–413.

[7] G. Ambartsoumian, R. Gouia-Zarrad and M. Lewis, "Inversion of the circular Radon transform on an annulus," *Inverse Problems*, **26** (2010), 105015.

[8] G. Ambartsoumian, V. Krishnan and E. T. Quinto, "The microlocal analysis of the ultrasound operator with circular source and receiver trajectory," *preprint.*

[9] G. Ambartsoumian and P. Kuchment, "On the injectivity of the circular Radon transform," *Inverse Problems*, **21** (2005), 473.

[10] G. Ambartsoumian and P. Kuchment, "A range description for the planar circular Radon transform," *SIAM J. Math. Anal.*, **38** (2006), 681–692.

[11] M. Anastasio, J. Zhang, E. Sidky, Y. Zou, D. Xia and X. Pan, "Feasibility of half-data image reconstruction in 3D reflectivity tomography with a spherical aperture," *IEEE Trans. Med. Imag.*, **24** (2005), 1100–12.

[12] M. Anastasio, J. Zhang, X. Pan, Y. Zou, G. Ku and L. V. Wang, "Half-time image reconstruction in thermoacoustic tomography," *IEEE Trans. Med. Imag.*, **24** (2005), 199–210.

[13] M. Anastasio, X. Pan and Y. Zou, "Data Redundancy and Reduced-Scan Reconstruction in Reflectivity Tomography," *IEEE Transactions on Image Processing*, **12** (2003), 784–95.

[14] L.-E. Andersson, "On the determination of a function from spherical averages," *SIAM J. Math. Anal.*, **19** (1988), 214–232.

[15] M. Born and E. Wolf, *Principles of optics: electromagnetic theory of propagation, interference and diffraction of light*, Oxford, New York, Pergamon Press, 1965.

[16] M. Cheney, "Tomography prolems arising in Synthetic Aperture Radar," in *Radon Transforms and Tomography,* ed. *E.T. Quinto, L. Ehrenpreis, A. Faridani, F. Gonzalez, E. Grinberg*, American Math. Soc., Providence, RI, 2001.

[17] R. Cobbold, *Foundations of Biomedical Ultrasound*, Oxford Univ. Press, 2007.

[18] J. Coker and A. Tewfik, "Multistatic SAR image reconstruction based on an elliptical-geometry Radon transform," *2007 International Waveform Diversity and Design Conference*, 204–208, IEEE Conference Proceedings, 2007.

[19] A. Cormack, "Representation of a function by its line integrals, with some radiological applications," *J. Appl. Phys.* **34** (1963), 2722–27.

[20] A. Cormack, "Representation of a function by its line integrals, with some radiological applications II," *J. Appl. Phys.* **35** (1964), 2908–12.

[21] R. Courant and D. Hilbert, *Methods of Mathematical Physics*, Vol.2, Wiley, New York, 1989.

[22] S. Deans, "Gegenbauer transforms via the Radon transform," *SIAM J. Math. Anal.*, **10** (1979), 577–85.

[23] S. Deans, *The Radon transform and some of its applications* , Dover Publications, New York, 1993.

[24] L. Ehrenpreis, *The Universality of the Radon Transform*, Oxford Univ. Press, New York, 2003.

[25] C. Epstein, *Introduction to the mathematics of medical imaging*, SIAM, Philadelphia, 2003.

[26] J. A. Fawcett, "Inversion of n-dimensional spherical averages," *SIAM J. Appl. Math.*, **45** (1985), 336–341.

[27] D. Finch, M. Haltmeier and Rakesh, "Inversion of spherical means and the wave equation in even dimension," *SIAM J. Appl. Math*, **68** (2007), 392–412.

[28] D. Finch and Rakesh, "The spherical mean value operator with centers on a sphere," *Inverse Problems*, **23** (2007), s37–s49.

[29] D. Finch and Rakesh, "The range of the spherical mean value operator for functions supported in a ball," *Inverse Problems*, **22** (2006), 923–938.

[30] D. Finch, Rakesh and S. K. Patch, "Determining a function from its mean values over a family of spheres," *SIAM J. Math. Anal.*, **35** (2004), 1213–1240.

[31] I. Gelfand and G. Shilov, *Generalized Functions*, Vol. 1, Academic, New York, 1964.

[32] S. Helgason, *The Radon Transform*, Birkhäuser, Basel, 1980.

[33] A. C. Kak and M. Slaney, *Principles of Computerized Tomographic Imaging*, IEEE Press, New York, 1988.

[34] P. Kuchment and L. Kunyansky, "A Survey in Mathematics for Industry: Mathematics of thermoacoustic tomography," *European J. Appl. Math.*, **19** (2008), 191–224.

[35] L. Kunyansky, "Explicit inversion formulas for the spherical mean Radon transform," *Inverse Problems*, **23** (2007), 373–383.

[36] H. Levinson, "Reconstruction Algorithms for Bistatic Radar and Ultrasound Imaging," *BS thesis*, (2011).

[37] V. Ya. Lin and A. Pinkus, "Fundamentality of ridge functions," *J. Approx. Theory*, **75** (1993), 295–311.

[38] A. K. Louis and E. T. Quinto, "Local tomographic methods in Sonar," in *Surveys on Solution Methods for Inverse Problems*, 147–154, Springer, Vienna, 2000.

[39] S. Mensah and E. Franceschini, "Near-field ultrasound tomography," *J. Acoust. Soc. Am*, **121** (2007), 1423–1433.

[40] S. Mensah, E. Franceschini and M.-C. Pauzin, "Ultrasound mammography," *Nuclear Instruments and Methods in Physics Research*, Section A, **571** (2007), 52–55.

[41] D. Ludwig, "The Radon transform on Euclidean space," *Comm. Pure App. Math.*, **19** (1966), 41–81.

[42] F. Natterer, *The Mathematics of Computerized Tomography*, Wiley, New York, 1986.

[43] F. Natterer and F. Wübbeling, *Mathematical Methods in Image Reconstruction*, Monographs on Mathematical Modeling and Computation v. 5, SIAM, Philadelphia, PA, 2001.

[44] M. Nessibi, L. Rachdi and K. Trimeche, "Ranges and inversion formulas for the spherical mean operator and its dual," *J. Mat. Anal. Appl.*, **196** (1995), 861–884.

[45] S. J. Norton, "Reconstruction of a reflectivity field fro line integrals over circular paths," *J. Acoust. Soc. Am.*, **67** (1980), 853–863.

[46] S. J. Norton, "Reconstruction of a two-dimensional reflecting medium over a circular domain: Exact Solution," *J. Acoust. Soc. Am.*, **67** (1980), 1266–1273.

[47] S. J. Norton and M. Linzer, "Ultrasonic reflectivity imaging in three dimensions: exact inverse scattering solutions for plane, cylindrical, and spherical apertures," *IEEE Trans. Biomed. Eng.*, **28** (1981), 202–220.

[48] U. Patel and D. Rickards, *Handbook of Transrectal Ultrasound and Biopsy of the Prostate*, Taylor & Francis, 2002.

[49] A. Polyanin and A. Manzhirov, *Handbook of Integral Equations*, Boca Raton: CRC Press, 1998.

[50] T. Rivlin, *Chebyshev Polynomials : From Approximation Theory to Algebra and Number Theory*, John Wiley & Sons, 1990.

[51] F. Tricomi, *Integral Equations*, Dover Publications, New York, 1983.

[52] R. Vaidyanathan, M. Lewis, G. Ambartsoumian and T. Aktosun, "Reconstruction algorithms for interior and exterior spherical Radon transform-based ultrasound imaging," *Proceedings of SPIE*, **7265** (2009), 72651I, 1–8.

[53] V. Volterra, *Theory of Functionals and of Integral and Integro-Differential Equations*, Dover Publications, New York, 2005.

[54] M. Xu and L. Wang, "Universal Back-projection algorithm for photoacoustic computed tomography," *The American Physical Society* , **71** (2005), 016706.

[55] M. Xu and L. Wang, "Photoacoustic imaging in biomedecine," *Review of scientific instruments*, **77** (2006), 041101.

[56] Y. Xu, L. Wang, G. Ambartsoumian and P. Kuchment, "Reconstructions in limited view thermoacoustic tomography," *Medical Physics*, **31** (2004), 724–733.

BIOGRAPHICAL STATEMENT

Rim Gouia was born in Tunisia in 1979. After an excellent A-Level/ baccalaureate degree, she moved to Paris to pursue the prestigious Classes Preparatoires and earn a M.S. in Engineering in 2004 from Ecole Centrale Paris, France. Then she worked for two major corporate houses: Bougues-Construction in France and XTO Energy (currently Exxon Mobile) in USA, before deciding to return to academia and pursue a Ph.D. in Applied Mathematics. Shortly after joining the University of Texas at Arlington (UTA) in 2007, she became a research assistant to Dr. Gaik Ambartsoumian and joined a multidisciplinary research team supported by the US Department of Defense aiming at improving Ultrasound Imaging for cancer screening. She specializes in integral geometry and in particular the mathematical problems of Radon transform applied to advanced imaging. In 2010, she published a paper in the journal *Inverse Problems* titled "Inversion of the circular Radon transform on an annulus". Since then she became a reviewer in the same journal and was invited to several international conferences and workshops.

She has also taught different mathematics classes at various colleges in the US. With her academic background and her multidisciplinary career as engineer and mathematician, she strives to shed some light on the elegance and beauty of mathematics by connecting its conceptual world to solving real-life problems.

Based on her academic achievement and her dedication, the UTA Department of Mathematics selected her as the outstanding student of the year 2010-2011 awarding her the *Stephen R. Bernfeld Memorial Scholarship.*

Inversion of the circular Radon transform on an annulus

Gaik Ambartsoumian[1]**, Rim Gouia-Zarrad**[1] **and Matthew A Lewis**[2]

[1] Department of Mathematics, University of Texas at Arlington, Arlington, TX 76017-0408, USA
[2] Department of Radiology, UT Southwestern Medical School, Dallas, TX 75390-9058, USA

E-mail: gambarts@uta.edu, rim.gouia@mavs.uta.edu and matthew.lewis@utsouthwestern.edu

Abstract

The representation of a function by its circular Radon transform (CRT) and various related problems arise in many areas of mathematics, physics and imaging science. There has been a substantial spike of interest toward these problems in the last decade mainly due to the connection between the CRT and mathematical models of several emerging medical imaging modalities. This paper contains some new results about the existence and uniqueness of the representation of a function by its CRT with partial data. A new inversion formula is presented in the case of the circular acquisition geometry for both interior and exterior problems when the Radon transform is known for only a part of all possible radii. The results are not only interesting as original mathematical discoveries, but can also be useful for applications, e.g., in medical imaging.

1. Introduction

The circular Radon transform (CRT) $g = Rf$ puts into correspondence to a given function f its integrals along circles

$$g(x_0, y_0, r) = Rf\ (x_0, y_0, r) = \int_{C(x_0, y_0, r)} f(x, y)\, \mathrm{d}s, \tag{1}$$

where $C(x_0, y_0, r)$ denotes the circle of radius r centered at the point (x_0, y_0).

If $Rf(x_0, y_0, r)$ is known for all possible values of its three arguments, then the reconstruction of a function $f(x, y)$ of two variables from Rf is an overdetermined problem. It is reasonable to expect that one can still uniquely recover f from Rf after reducing the degrees of freedom of Rf by 1. There are many different ways to reduce the dimensions of the data Rf, e.g., by considering only the data coming from circles of a certain fixed radius, circles passing through a fixed point, circles tangent to a line, circles with centers located on a curve, etc. All of these approaches lead to interesting mathematical problems, and various
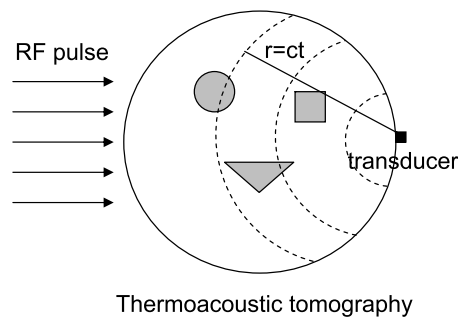
Figure 1. A sketch of TAT/PAT.

research groups have done extensive amount of work on this subject. One can find good surveys and abundant lists of references to papers dedicated to these topics in [3, 4, 17, 18, 20].

In this paper we concentrate on the problem of recovering f from Rf data limited to circles, which are centered on a circle $C(R) \equiv C(0, 0, R)$. Our consideration is partially motivated by several medical imaging applications briefly described below.

Thermoacoustic tomography (TAT) and photoacoustic tomography (PAT) are two emerging medical imaging modalities, which are based on the same principles (see [21] for a great survey on mathematical problems in TAT and PAT). The part of the human body being imaged is exposed to a short pulse of electromagnetic (EM) radiation (radio-frequency (RF) waves in TAT and lasers in PAT). A portion of this radiation is absorbed in the body, heating up the tissue, and causing thermal expansion, which in turn generates acoustic waves traveling through the body. Multiple transducers placed outside of the body record these acoustic signals for some time. Then the collected data are processed to generate an image of the heat absorption function inside the body. The premise here is that there exists a strong contrast in the amount of absorbed EM energy between different types of tissues. For example, cancerous cells absorb several times more energy than the healthy ones; hence, recovery of the RF absorption function inside the body can help both to diagnose and to locate cancer. At the same time sound waves have very weak contrast in the tissue; therefore, one can simplify the model assuming the sound speed c to be constant in the body [36–38]. Under this assumption the signals registered by a transducer at any moment of time t would be generated by inclusions lying on a sphere of radius $r = ct$ centered at the transducer location (see figure 1). Thus, the problem of image reconstruction in TAT and PAT boils down to the recovery of the image function f from Rf data along spheres centered at available transducer locations. By using plane-focused transducers one can consider a 2D problem of inverting the CRT to reconstruct planar slices of the image function. The transducer locations here (i.e. the centers of integration circles) will be limited to a planar curve on the edge of the body. The simplest such curve (i.e. the simplest data acquisition geometry) both for the mathematical model and from the engineering point of view is a circle, and that is the geometry we consider in this paper (see [18] for a survey on spherical Radon transforms with centers on a sphere).

Another medical imaging modality that uses the CRT in its mathematical model is the ultrasound reflection tomography (e.g. see [29, 30]). Here, the transducer placed at the edge of the body works in dual modes first as an emitter of sound waves and then as a receiver, registering the reflection of ultrasound waves from the inclusions inside the body. Assuming a constant speed of sound propagation, the problem of recovering the reflectivity function inside the body corresponds to the problem of inverting the CRT with data collected along the circles

of radius $r = ct/2$. Some other applications of this transform include sonar and radar imaging (e.g. see [9, 25]).

2. Previous works and known results

The major problems studied in relation to Radon transforms include the existence and uniqueness of their inversions, inversion formulae and algorithms, the stability of these algorithms and the range descriptions of the transforms (e.g. see [14, 27, 28]). The first three problems for the circular transform will be discussed throughout this paper. For the detailed description and known results about range descriptions, we refer the reader to papers [2, 5, 19].

The existence and uniqueness problem of the inversion of the CRT has been studied by many authors for various restrictions of Rf and various classes of function f (see [1, 3, 4, 8, 13, 15, 17, 18, 29, 30] and the references therein).

In a classical work [3] Agranovsky and Quinto provided a complete solution to the problem in the case when f has compact support and Rf is known along circles of all possible radii centered on a given set.

Agranovsky *et al* in [1] used PDE techniques to study the injectivity problem of the spherical Radon transform (*n*-dimensional generalization of the circular transform) when $f \in L^p(\mathbb{R}^n)$ and Rf is known for spheres of all possible radii centered at every point of the boundary of some domain D.

Finch *et al* in [17] studied this problem for smooth f supported in a bounded connected domain $D \subset \mathbb{R}^n$. For strictly convex $\overline{D}$ they proved the uniqueness of inversion using Rf from spheres centered on any open subset of the boundary of D and all possible radii. In the case of odd *n* they also showed uniqueness of inversion from data with spheres centered at every point of the boundary and radii limited to $r < \text{diam}(D)/2$. The proof of the latter result would not extend to even dimensions, since it was based on the solution properties of certain problems related to wave equation, that hold only in odd dimensions.

Ambartsoumian and Kuchment in [4] obtained some further results on injectivity of the spherical transform, providing several sufficient conditions on the data acquisition geometry, in order for the transform to have a unique inverse. That paper also used Rf from spheres of all possible radii.

Lavrentiev *et al* in [24] proved the injectivity of a Radon-type transform integrating along a fairly general family of curves invariant with respect to rotations around the origin, when only half of the possible 'radii' of these curves are used, and the function is supported inside the circle. No inversion formulae were derived in that work.

Anastasio *et al* showed in [7] that in the 3D spherical acquisition geometry the Radon data for half of all possible radii are sufficient for unique reconstruction of the unknown function supported inside the sphere. It was mentioned that the technique can be applied to obtain a similar result in 2D. The work did not provide an exact inversion formula, and it did not address the uniqueness problem when the support of the unknown function extends outside of the sphere.

In circular acquisition geometry there are various inversion formulae when Rf is known for circles of all possible radii [16, 22, 23, 29]. However, to the best of our knowledge no exact formula is known for the case when Rf is available for only half of all possible radii, or when the support of f is outside the circle.

In this paper we derive inversion formulae of the CRT from Rf data collected along all circles centered on the circle $C(R)$ and of radii $r < R_1 \leqslant \text{diam}(D)/2$. The result holds when f is supported inside the annulus $A(\varepsilon, R) = \{(x, y) : \varepsilon < \sqrt{x^2 + y^2} < R\}$ for any $\varepsilon > 0$,
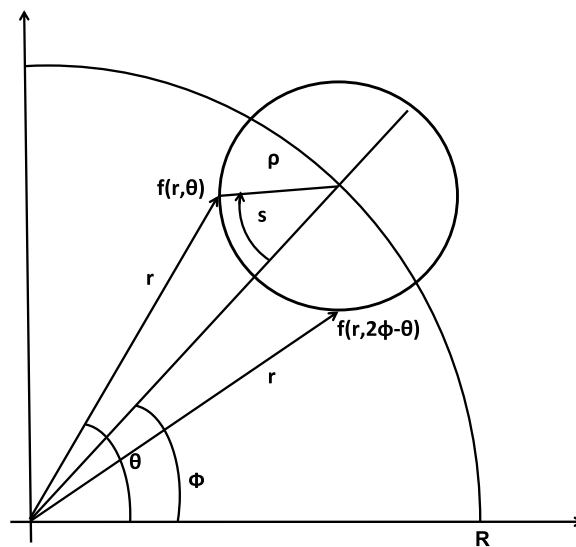
Figure 2. Geometric setup of integration along the circle $C(\rho, \phi)$.

as well as when f is supported inside the annulus $A(R, 3R)$. Some other cases, such as f defined inside $D(0, 2R)$ by the radial symmetry with respect to the circle $C(R)$, follow as simple corollaries.

3. Main results

3.1. Notations

Throughout this section, $f(r, \theta)$ denotes an unknown function supported inside the disk $D(0, 3R)$, where (r, θ) are the polar coordinates measured from the center of that disk, and $R > 0$ is a fixed number. The CRT of f along a circle of radius ρ centered at a point with the polar coordinates (R, ϕ) (see figure 2) is denoted by

$$g(\rho, \phi) = Rf(\rho, \phi) = \int_{C(\rho,\phi)} f(r, \theta) \, ds. \tag{2}$$

The Fourier series generated by $f(r, \theta)$ and $g(\rho, \phi)$ with respect to corresponding angular variables are denoted by

$$f(r, \theta) = \sum_{n=-\infty}^{\infty} f_n(r) \, e^{in\theta}, \tag{3}$$

$$g(\rho, \phi) = \sum_{n=-\infty}^{\infty} g_n(\rho) \, e^{in\phi}, \tag{4}$$

where the Fourier coefficients $f_n(r)$ and $g_n(\rho)$ are computed by

$$f_n(r) = \frac{1}{2\pi} \int_0^{2\pi} f(r, \theta) \, e^{-in\theta} \, d\theta, \tag{5}$$

4

$$g_n(\rho) = \frac{1}{2\pi} \int_0^{2\pi} g(\rho, \phi)\, e^{-in\phi}\, d\phi. \tag{6}$$

3.2. Functions supported in an annulus $A(\varepsilon, R)$

In this subsection we consider a smooth function $f(r, \theta)$ supported inside the disk of radius R. We show that the function can be uniquely recovered from Radon data with only part of all possible radii, and then provide a reconstruction formula.

Theorem 1.　*Let $f(r, \theta)$ be an unknown continuous function supported inside the annulus $A(\varepsilon, R) = \{(r, \theta) : r \in (\varepsilon, R), \theta \in [0, 2\pi]\}$, where $0 < \varepsilon < R$. If $Rf(\rho, \phi)$ is known for $\phi \in [0, 2\pi]$ and $\rho \in [0, R - \varepsilon]$, then $f(r, \theta)$ can be uniquely recovered in $A(\varepsilon, R)$.*

Proof.　We use an approach similar to Cormack's inversion of the linear Radon transform [11]. Let us rewrite formula (2) by considering the contribution dg to $g(\rho, \phi)$ from two equal elements of arc ds of the circle $C(\rho, \phi)$. If the two elements of the arc are located symmetrically with respect to the polar radius of the center of the integration circle (see figure 2), then

$$dg = \sum_{n=-\infty}^{\infty} [f_n(r)\, e^{in\theta} + f_n(r)\, e^{in(2\phi-\theta)}]\, ds, \qquad 0 \leqslant \phi \leqslant \theta \leqslant 2\pi,$$

so we can write

$$g(\rho, \phi) = \int_{C^+(\rho, \phi)} \sum_{n=-\infty}^{\infty} [f_n(r)\, e^{in\theta} + f_n(r)\, e^{in(2\phi-\theta)}]\, ds, \qquad 0 \leqslant \phi \leqslant \theta \leqslant 2\pi,$$

where $C^+(\rho, \phi)$ denotes half of the circle $C(\rho, \phi)$ corresponding to $\theta \geqslant \phi$.

Note that $e^{in\theta} + e^{in(2\phi-\theta)} = 2\, e^{in\phi} \cos[n(\theta - \phi)]$ and $s = \rho \arccos\left(\frac{\rho^2 + R^2 - r^2}{2\rho R}\right)$, hence

$$ds = \frac{r\, dr}{R\sqrt{1 - \left(\frac{\rho^2 + R^2 - r^2}{2\rho R}\right)^2}}.$$

Exchanging the order of summation and integration and using these relations we get

$$g(\rho, \phi) = \sum_{n=-\infty}^{\infty} 2\, e^{in\phi} \int_{R-\rho}^{R} \frac{f_n(r)\, r\, \cos[n(\theta - \phi)]}{R\sqrt{1 - \left(\frac{\rho^2 + R^2 - r^2}{2\rho R}\right)^2}}\, dr.$$

Applying $\theta - \phi = \arccos\left(\frac{r^2 + R^2 - \rho^2}{2rR}\right)$, we obtain

$$g(\rho, \phi) = \sum_{n=-\infty}^{\infty} 2\, e^{in\phi} \int_{R-\rho}^{R} \frac{f_n(r)\, r\, \cos\left[n \arccos\left(\frac{r^2 + R^2 - \rho^2}{2rR}\right)\right]}{R\sqrt{1 - \left(\frac{\rho^2 + R^2 - r^2}{2\rho R}\right)^2}}\, dr. \tag{7}$$

Comparing equations (4) and (7) it is easy to note that by passing to the basis of complex exponentials we diagonalized the CRT, i.e. the nth Fourier coefficient of g depends only on the nth Fourier coefficient of f. This is not surprising, due to the rotation invariance property of Rf in the circular geometry. As a result, our problem breaks down to the following set of one-dimensional integral equations:

$$g_n(\rho) = 2 \int_{R-\rho}^{R} \frac{f_n(r)\, r\, T_{|n|}\left(\frac{r^2 + R^2 - \rho^2}{2rR}\right)}{R\sqrt{1 - \left(\frac{\rho^2 + R^2 - r^2}{2\rho R}\right)^2}}\, dr, \tag{8}$$

where $T_k(x)$ is the kth-order Chebyshev polynomial of the first kind.

Let us make a change of variables in integral (8) by setting $u = R - r$. Then equation (8) becomes

$$g_n(\rho) = \int_0^\rho \frac{f_n(R-u)\, 4\rho\,(R-u)\, T_{|n|}\!\left[\frac{(R-u)^2+R^2-\rho^2}{2R\,(R-u)}\right]}{\sqrt{\rho-u}\sqrt{(u+\rho)(2R+\rho-u)(2R-\rho-u)}}\, du, \tag{9}$$

which can be rewritten as

$$g_n(\rho) = \int_0^\rho \frac{F_n(u)\, K_n(\rho, u)}{\sqrt{\rho-u}}\, du, \tag{10}$$

where

$$F_n(u) = f_n(R-u), \tag{11}$$

$$K_n(\rho, u) = \frac{4\rho\,(R-u)\, T_{|n|}\!\left[\frac{(R-u)^2+R^2-\rho^2}{2R(R-u)}\right]}{\sqrt{(u+\rho)(2R+\rho-u)(2R-\rho-u)}}. \tag{12}$$

Equation (10) is a Volterra integral equation of the first kind with a weakly singular kernel (e.g. see [32, 33]). Indeed, due to the assumptions on the support of f we know that $F_n(u) \equiv 0$ for u close to R or 0. Therefore, from formula (12) and the properties of Chebyshev polynomials, it follows that the kernel $K_n(\rho, u)$ is continuous in its arguments (and hence bounded) along with the first-order partial derivatives on the support of F_n.

To get rid of the singularity in the kernel of equation (10), we apply the standard method of kernel transformation [34]. Multiplying both sides of equation (10) by $\frac{1}{\sqrt{t-\rho}}\, d\rho$ and integrating from 0 to t, we get

$$\int_0^t \frac{g_n(\rho)}{\sqrt{t-\rho}}\, d\rho = \int_0^t \int_0^\rho \frac{F_n(u) K_n(\rho, u)}{\sqrt{\rho-u}\sqrt{t-\rho}}\, du\, d\rho, \qquad t > 0.$$

Changing the order of integration, we obtain

$$\int_0^t \frac{g_n(\rho)}{\sqrt{t-\rho}}\, d\rho = \int_0^t F_n(u)\, Q_n(t, u)\, du, \tag{13}$$

where

$$Q_n(t, u) = \int_u^t \frac{K_n(\rho, u)}{\sqrt{\rho-u}\sqrt{t-\rho}}\, d\rho.$$

The advantage of equation (13) in comparison to equation (10) is that the modified kernel $Q_n(t, u)$ is finite. Indeed, making a change of variables $\rho = u + (t-u)\, l,\ 0 \leqslant l \leqslant 1$ in the last integral, we get

$$Q_n(t, u) = \int_0^1 \frac{K_n(u + (t-u)\, l, u)}{\sqrt{l}\,\sqrt{1-l}}\, dl. \tag{14}$$

Since K_n is bounded (say $|K_n| < M$), we obtain

$$|Q_n(t, u)| < M \int_0^1 \frac{dl}{\sqrt{l}\,\sqrt{1-l}} = M\pi.$$

In addition $Q_n(t, t) = \pi K_n(t, t) = \pi \sqrt{\frac{2t\,(R-t)}{R}} \neq 0$ on the support of F_n.

Now we can easily modify equation (13) to a Volterra equation of second kind. Differentiating equation (13) with respect to t, we get

$$\frac{d}{dt} \int_0^t \frac{g_n(\rho)}{\sqrt{t-\rho}}\, d\rho = \pi F_n(t)\, K_n(t, t) + \int_0^t F_n(u) \left[\frac{\partial}{\partial t} \int_u^t \frac{K_n(\rho, u)}{\sqrt{\rho-u}\sqrt{t-\rho}}\, d\rho \right] du.$$

Dividing both sides of the last equation by $\pi K_n(t, t)$ and denoting

$$G_n(t) = \frac{1}{\pi K_n(t, t)} \frac{\mathrm{d}}{\mathrm{d}t} \int_0^t \frac{g_n(\rho)}{\sqrt{t - \rho}} \, \mathrm{d}\rho \tag{15}$$

and

$$L_n(t, u) = \frac{1}{\pi K_n(t, t)} \frac{\partial}{\partial t} \int_u^t \frac{K_n(\rho, u)}{\sqrt{\rho - u}\sqrt{t - \rho}} \, \mathrm{d}\rho, \tag{16}$$

we finally obtain a Volterra equation of second kind:

$$G_n(t) = F_n(t) + \int_0^t F_n(u) L_n(t, u) \, \mathrm{d}u, \tag{17}$$

where the kernel $L_n(t, u)$ is continuous on the support of F_n. To see the continuity of L_n, one can make a change of variables in equation (16):

$$\rho = t \cos^2 \beta + u \sin^2 \beta, \qquad \beta \in [0, \pi/2],$$

and express L_n as

$$L_n(t, u) = \frac{2}{\pi K_n(t, t)} \frac{\partial}{\partial t} \int_0^{\pi/2} K_n(t \cos^2 \beta + u \sin^2 \beta, u) \, \mathrm{d}\beta.$$

The Volterra equation of the second kind (17) has a unique solution, which finishes the proof of the theorem. $\qquad\qquad\square$

Using Picard's process of successive approximations (e.g. see [33]) for the solution of the Volterra equations of the second kind, one can immediately obtain the following.

Corollary 2. *An exact solution of equation (17) is given by the formula*

$$F_n(t) = G_n(t) + \int_0^t H_n(t, u) G_n(u) \, \mathrm{d}u, \tag{18}$$

where the resolvent kernel $H_n(t, u)$ is given by the series of iterated kernels

$$H_n(t, u) = \sum_{i=1}^{\infty} (-1)^i L_{n,i}(t, u), \tag{19}$$

defined by

$$L_{n,1}(t, u) = L_n(t, u) \tag{20}$$

and

$$L_{n,i}(t, u) = \int_u^t L_{n,1}(t, x) L_{n,i-1}(x, u) \, \mathrm{d}x, \qquad \forall i \geqslant 2. \tag{21}$$

This corollary (with notations defined in formulas (11), (12), (15) and (16)) provides a new exact formula for the inversion of the CRT in circular acquisition geometry. Its advantage compared to all the other known exact inversion formulae is the fact that only part of the Rf data are used. Namely, it is easy to note the following.

Remark 3. In order to reconstruct the function $f(r, \theta)$ in any subset Ω of the disk of its support $D(0, R)$, the inversion formula in corollary 2 requires the knowledge of $Rf(\rho, \phi)$, only for $\rho < R - R_0$, where $R_0 = \inf\{|x|, \ x \in \Omega\}$.

In medical imaging, reducing the radial data redundancy can be essential for increasing the depth and reducing the time of imaging.

Remark 4. The resolvent kernel $H_n(t, u)$ is the same for any functions f and g. Hence, in practice, one needs to compute it with the desired accuracy only once, and then it can be used with any data set.

Remark 5. In theorem 1 we require f to be continuous, which guarantees the convergence of the Fourier series (3) and (4) almost everywhere. If one needs to ensure convergence everywhere, then some additional conditions on f (e.g. bounded variation) should be added in theorem 1 and the other two theorems in this paper.

3.3. Functions supported inside an annulus $A(R, 3R)$

Let us now consider an exterior problem in the circular acquisition geometry, i.e. the Radon data are still collected along circles centered on a circle of radius R; however, the unknown function f is supported outside of the disk $D(0, R)$.

Theorem 6. *Let $f(r, \theta)$ be an unknown continuous function supported inside the annulus $A(R, 3R) = \{(r, \theta) : r \in (R, 3R), \ \theta \in [0, 2\pi]\}$. If $Rf(\rho, \phi)$ is known for $\phi \in [0, 2\pi]$ and $\rho \in [0, R_1]$, where $0 < R_1 < 2R$, then $f(r, \theta)$ can be uniquely recovered in $A(R, \ R_1)$.*

Proof. The argument of the proof of the previous theorem repeats here with very small changes. The condition $0 < R_1 < 2R$ guarantees that all integration circles $C(\rho, \phi)$ intersect the boundary of the disk $D(0, R)$. Hence equation (7) in this case becomes

$$g(\rho, \phi) = \sum_{n=-\infty}^{\infty} 2 \, e^{in\phi} \int_R^{R+\rho} \frac{f_n(r) \, r \cos\left[n \arccos\left(\frac{r^2+R^2-\rho^2}{2rR}\right)\right]}{R \sqrt{1 - \left(\frac{\rho^2+R^2-r^2}{2\rho R}\right)^2}} \, dr. \tag{22}$$

Then in a similar way, we have

$$g_n(\rho) = 2 \int_R^{R+\rho} \frac{f_n(r) r T_{|n|}\left(\frac{r^2+R^2-\rho^2}{2rR}\right)}{R \sqrt{1 - \left(\frac{\rho^2+R^2-r^2}{2\rho R}\right)^2}} \, dr. \tag{23}$$

Now making a change of variables $u = r - R$ in the last expression, we get

$$g_n(\rho) = \int_0^\rho \frac{f_n(R + u) \, 4\rho \, (R + u) T_{|n|}\left[\frac{(R+u)^2+R^2-\rho^2}{2R(R+u)}\right]}{\sqrt{\rho - u}\sqrt{(u + \rho)(2R + u + \rho)(2R + u - \rho)}} \, du, \tag{24}$$

which can be rewritten as

$$g_n(\rho) = \int_0^\rho \frac{F_n(u) \, K_n(\rho, u)}{\sqrt{\rho - u}} \, du, \tag{25}$$

where

$$F_n(u) = f_n(R + u), \tag{26}$$

$$K_n(\rho, u) = \frac{4\rho \, (R + u) T_{|n|}\left[\frac{(R+u)^2+R^2-\rho^2}{2R(R+u)}\right]}{\sqrt{(u + \rho)(2R + u + \rho)(2R + u - \rho)}}. \tag{27}$$

Note that if one would allow $\rho > 2R$, then $K_n(\rho, u)$ would become unbounded due to the last multiplier in the denominator. This shows that $3R$ is an accurate upper limit for the outer radius of the annulus in the hypothesis of the theorem.

In analogy with the proof of the previous theorem we get

$$K_n(t, t) = \sqrt{\frac{2t(R + t)}{R}} \neq 0.$$

All the other steps literally repeat the proof of theorem 1. $\qquad\square$

3.4. Functions supported inside the disk $D(0, 2R)$

It is easy to note that in some special cases one can combine the results of the previous two theorems to reconstruct a function whose support is located both inside and outside of the circular path $C(R)$ of data acquisition. For example,

Theorem 7. *Let f be an unknown continuous function supported inside the disk $D(0, 2R)$. Assume also that $f \equiv 0$ in some neighborhood of the circle $C(R)$, and all its Fourier coefficients are even (or odd) with respect to $C(R)$, i.e. $f_n(R + u) = f_n(R - u)$ (or $f_n(R + u) = -f_n(R - u)$) for $\forall u \in [0, R]$. If $Rf(\rho, \phi)$ is known for $\phi \in [0, 2\pi]$ and $\rho \in [0, R_1]$, where $0 < R_1 < R$, then $f(r, \theta)$ can be uniquely recovered in $A(R - R_1, R + R_1)$.*

Proof. Combining the two previous results, we obtain a Volterra integral equation of the first kind

$$g_n(\rho) = \int_0^\rho \frac{F_n(u) K_n(\rho, u)}{\sqrt{\rho - u}} \, \mathrm{d}u, \tag{28}$$

where

$$F_n(u) = f_n(R + u) \tag{29}$$

and

$$K_n(\rho, u) = \frac{4\rho}{\sqrt{u + \rho}} \left\{ \frac{(R + u) T_{|n|}\left[\frac{(R+u)^2 + R^2 - \rho^2}{2R(R+u)}\right]}{\sqrt{(2R + u + \rho)(2R + u - \rho)}} \pm \frac{(R - u) T_{|n|}\left[\frac{(R-u)^2 + R^2 - \rho^2}{2R(R-u)}\right]}{\sqrt{(2R + \rho - u)(2R - \rho - u)}} \right\}. \tag{30}$$

The rest of the proof is carried out along the same lines as before. $\qquad\square$

It is interesting to note that the CRT in the linear acquisition geometry can be uniquely inverted on the class of continuous functions that are even with respect to the linear path of the data acquisition. At the same time all odd functions are mapped to zero by that transform. In our case (of circular acquisition geometry), the CRT can be uniquely inverted on classes of functions with Fourier coefficients that are even with respect to the circular path of data acquisition, as well as with the ones that are odd.

4. Additional remarks

(i) While it is well established that acoustic breast tomography in its various forms is a classic example of spherical Radon-based imaging *inside* a spherical/circular (3D/2D) aperture, the case of imaging *outside* a spherical aperture is a less well-described biomedical concept. Two biomedical imaging methods can currently be modeled in the time domain through spherical transforms of a function exterior to the aperture: transrectal ultrasound (TRUS) [31] and intravascular ultrasound (IVUS) (see section 8.10 in [10] and the references therein). In both TRUS and IVUS, an ultrasound array arranged on the surface of a cylinder is introduced into the body with the goal of producing a transverse or axial image. In TRUS, the typical application is imaging of the male prostate, while IVUS is a higher resolution ultrasound technique typically used to evaluate plaques in blood vessels.

A setup where the support of the unknown function is located on both sides of the data acquisition path may not be relevant to medical imaging; however, it can be applicable in radar and sonar imaging [9, 25].

(ii) The reconstruction of f from partial Rf data is an extremely ill-conditioned problem and, despite all uniqueness results, in practical implementation one can expect to recover stably only certain parts of the image, the rest of it being blurred out (e.g. [6, 38]). This is due to the fact that some parts of the wavefront set $WF(f)$ of the image will be lost [25, 39]. More specifically, a point $(x, \xi) \in WF(f)$ can be stably detected from the Radon data, if and only if Rf includes data obtained from a circle passing through x and co-normal to ξ. In other words, one can see only those parts of image singularities that can be tangentially touched by available circles of integration.

It is easy to notice that in the case of the interior problem with the available radii $\rho < R$ all singularities can be stably resolved. In the exterior problem only singularities in the directions close to normals of polar radius can be recovered with little or no blurring. However, this may be enough for example in IVUS, where the imaging is done along the vein walls, which are normal to the polar radii directions.

(iii) The main results of the paper have potential to be generalized to higher dimensions using spherical harmonics and Gegenbauer polynomials akin to the generalization of Cormack's original inversion [11] to higher dimensions (e.g. see [26] and [12]). The authors plan to address this issue in future work.

(iv) An accurate and efficient numerical implementation of the inversion formulae derived in the paper is an interesting problem in its own right. This includes, among other things, a careful study of conditions ensuring that the resolvent kernels (19) are bounded. The authors plan to address this problem in future work.

Acknowledgments

References

[1] Agranovsky M L, Berenstein C A and Kuchment P 1996 Approximation by spherical waves in L^p-spaces *J. Geom. Anal.* **6** 365–83
[2] Agranovsky M L, Kuchment P and Quinto E T 2007 Range descriptions for the spherical mean Radon transform *J. Funct. Anal.* **248** 344–86
[3] Agranovsky M L and Quinto E T 1996 Injectivity sets for the Radon transform over circles and complete systems of radial functions *J. Funct. Anal.* **139** 383–413
[4] Ambartsoumian G and Kuchment P 2005 On the injectivity of the circular Radon transform *Inverse Problems* **21** 473–85
[5] Ambartsoumian G and Kuchment P 2006 A range description for the planar circular Radon transform *SIAM J. Math. Anal.* **38** 681–92
[6] Ambartsoumian G and Patch S K 2007 Thermoacoustic tomography: numerical results *Proc. SPIE* **6437** 64371B1–10
[7] Anastasio M, Zhang J, Sidky E, Zou Y, Xia D and Pan X 2005 Feasibility of half-data image reconstruction in 3D reflectivity tomography with a spherical aperture *IEEE Trans. Med. Imaging* **24** 1100–12
[8] Andersson L-E 1988 On the determination of a function from spherical averages *SIAM J. Math. Anal.* **19** 214–32
[9] Cheney M 2001 Tomography problems arising in synthetic aperture radar *Radon Transforms and Tomography* ed E T Quinto *et al* (Providence, RI: American Mathematical Society)
[10] Cobbold R 2007 *Foundations of Biomedical Ultrasound* (Oxford: Oxford University Press)

[11] Cormack A 1963 Representation of a function by its line integrals, with some radiological applications *J. Appl. Phys.* **34** 2722–7

[12] Deans S R 1979 Gegenbauer transforms via the Radon transform *SIAM J. Math. Anal.* **10** 577–85

[13] Denisjuk A 1999 Integral geometry on the family of semi-spheres *Fract. Calc. Appl. Anal.* **2** 31–46

[14] Ehrenpreis L 2003 *The Universality of the Radon Transform* (Oxford: Oxford University Press)

[15] Fawcett J A 1985 Inversion of *n*-dimensional spherical averages *SIAM J. Appl. Math.* **45** 336–41

[16] Finch D, Haltmeier M and Rakesh 2007 Inversion of spherical means and the wave equation in even dimension *SIAM J. Appl. Math.* **68** 392–412

[17] Finch D, Patch S K and Rakesh 2004 Determining a function from its mean values over a family of spheres *SIAM J. Math. Anal.* **35** 1213–40

[18] Finch D and Rakesh 2007 The spherical mean value operator with centers on a sphere *Inverse Problems* **23** s37–49

[19] Finch D and Rakesh 2006 The range of the spherical mean value operator for functions supported in a ball *Inverse Problems* **22** 923–38

[20] John F 1955 *Plane Waves and Spherical Means Applied to Partial Differential Equations* (New York: Interscience)

[21] Kuchment P and Kunyansky L 2008 A survey in mathematics for industry: mathematics of thermoacoustic tomography *Eur. J. Appl. Math.* **19** 191–224

[22] Kunyansky L 2007 Explicit inversion formulas for the spherical mean Radon transform *Inverse Problems* **23** 373–83

[23] Kunyansky L 2007 A series solution and a fast algorithm for the inversion of the spherical mean Radon transform *Inverse Problems* **23** s11–20

[24] Lavrentiev M, Romanov M and Vasiliev M 1970 *Multidimensional Inverse Problems for Differential Equations (Lecture Notes in Mathematics* vol 167*)* (Berlin: Springer)

[25] Louis A K and Quinto E T 2000 Local tomographic methods in Sonar *Surveys on Solution Methods for Inverse Problems* (Vienna: Springer) pp 147–54

[26] Ludwig D 1966 The Radon transform on Euclidean space *Commun. Pure Appl. Math.* **19** 41–81

[27] Natterer F 1986 *The Mathematics of Computerized Tomography* (New York: Wiley)

[28] Natterer F and Wübbeling F 2001 *Mathematical Methods in Image Reconstruction (Monographs on Mathematical Modeling and Computation* vol 5*)* (Philadelphia, PA: SIAM)

[29] Norton S J 1980 Reconstruction of a two-dimensional reflecting medium over a circular domain: exact solution *J. Acoust. Soc. Am.* **67** 1266–73

[30] Norton S J and Linzer M 1981 Ultrasonic reflectivity imaging in three dimensions: exact inverse scattering solutions for plane, cylindrical and spherical apertures *IEEE Trans. Biomed. Eng.* **28** 202–20

[31] Patel U and Rickards D 2002 *Handbook of Transrectal Ultrasound and Biopsy of the Prostate* (London: Taylor and Francis)

[32] Polyanin A and Manzhirov A 1998 *Handbook of Integral Equations* (Boca Raton, FL: CRC Press)

[33] Tricomi F 1983 *Integral Equations* (New York: Dover)

[34] Volterra V 2005 *Theory of Functionals and of Integral and Integro-Differential Equations* (New York: Dover)

[35] Xu M and Wang L-H 2002 Time-domain reconstruction for thermoacoustic tomography in a spherical geometry *IEEE Trans. Med. Imaging* **21** 814–22

[36] Xu Y, Feng D and Wang L-H 2002 Exact frequency-domain reconstruction for thermoacoustic tomography: I. Planar geometry *IEEE Trans. Med. Imaging* **21** 823–28

[37] Xu Y, Xu M and Wang L-H 2002 Exact frequency-domain reconstruction for thermoacoustic tomography: II. Cylindrical geometry *IEEE Trans. Med. Imaging* **21** 829–33

[38] Xu Y, Wang L-H, Ambartsoumian G and Kuchment P 2004 Reconstructions in limited view thermoacoustic tomography *Med. Phys.* **31** 724–33

[39] Xu Y, Wang L-H, Ambartsoumian G and Kuchment P 2009 Limited view thermoacoustic tomography *Photoacoustic Imaging and Spectroscopy* ed L-H Wang (Boca Raton, FL: CRC Press)